Monthly Notices of the ROYAL ASTRONOMICAL SOCIETY

MNRAS **452,** 2606–2640 (2015) doi:10.1093/mnras/stv1415

s-process enrichment in the planetary nebula NGC 3918. Results from deep echelle spectrophotometry

J. García-Rojas,[1,2]★ S. Madonna,[1,2] V. Luridiana,[1,2] N. C. Sterling,[3] C. Morisset,[4] G. Delgado-Inglada[4] and L. Toribio San Cipriano[1,2]

[1]*Instituto de Astrofísica de Canarias, E-38205 La Laguna, Tenerife, Spain*
[2]*Universidad de La Laguna, Dpto. Astrofísica, E-38206 La Laguna, Tenerife, Spain*
[3]*Department of Physics, University of West Georgia, 1601 Maple Street, Carrollton, GA 30118, USA*
[4]*Instituto de Astronomía, Universidad Nacional Autónoma de México, Apdo. Postal 70264, México D. F. 04510, Mexico*

Accepted 2015 June 23. Received 2015 June 22; in original form 2015 March 19

ABSTRACT

The chemical content of the planetary nebula NGC 3918 is investigated through deep, high-resolution ($R \sim 40\,000$) UVES (Ultraviolet-Visual Echelle Spectrograph) at VLT (Very Large Telescope) spectrophotometric data. We identify and measure more than 750 emission lines, making ours one of the deepest spectra ever taken for a planetary nebula. Among these lines we detect very faint lines of several neutron-capture elements (Se, Kr, Rb, and Xe), which enable us to compute their chemical abundances with unprecedented accuracy, thus constraining the efficiency of the s-process and convective dredge-up in NGC 3918 progenitor star. We find that Kr is strongly enriched in NGC 3918 and that Se is less enriched than Kr, in agreement with the results of previous papers and with predicted s-process nucleosynthesis. We also find that Xe is not as enriched by the s-process in NGC 3918 as is Kr and, therefore, that neutron exposure is typical of modestly subsolar metallicity asymptotic giant branch (AGB) stars. A clear correlation is found when representing [Kr/O] versus log(C/O) for NGC 3918 and other objects with detection of multiple ions of Kr in optical data, confirming that carbon is brought to the surface of AGB stars along with s-processed material during third dredge-up episodes, as predicted by nucleosynthesis models. We also detect numerous refractory element lines (Ca, K, Cr, Mn, Fe, Co, Ni, and Cu) and a large number of metal recombination lines of C, N, O, and Ne. We compute physical conditions from a large number of diagnostics, which are highly consistent among themselves assuming a three-zone ionization scheme. Thanks to the high ionization of NGC 3918 we detect a large number of recombination lines of multiple ionization stages of C, N, O and Ne. The abundances obtained for these elements by using recently determined state-of-the-art ionization correction factor (ICF) schemes or simply adding ionic abundances are in very good agreement, demonstrating the quality of the recent ICF scheme for high-ionization planetary nebulae.

Key words: stars: AGB and post-AGB – ISM: abundances – planetary nebulae: individual: NGC 3918.

1 INTRODUCTION

About half of the heavy elements ($Z > 30$) in the Universe are formed by slow neutron(n)-capture nucleosynthesis (the 's-process') in the asymptotic giant branch (AGB) phase, when neutrons are released in the intershell region between the H- and He-burning shells through the $^{13}C(\alpha, n)^{16}O$ reaction or, in more massive AGB stars ($M > 4$ M$_\odot$), the $^{22}Ne(\alpha, n)^{25}Mg$ reaction. Fe-peak nuclei in this layer, exposed to the neutron flux, experience n-captures interlaced with β-decays that transform them into heavier elements, in the process known as the 's-process'. The s-process- and He-burning-enriched material is later conveyed to the stellar envelope by convective dredge-up and released into the interstellar medium by

*E-mail: jogarcia@iac.es

stellar winds and planetary nebula (PN) ejection (Busso, Gallino & Wasserburg 1999; Herwig 2005; Käppeler et al. 2009; Karakas & Lattanzio 2014), where it can eventually be incorporated into a new generation of stars.

The exact details of this scenario are still poorly understood due to the lack of observational constraints to models of AGB nucleosynthesis (Karakas et al. 2009). Two major problems are strong obscuration by dust, which hinders observations in the optical, and the still-evolving surface composition, which complicates the interpretation of data. Fortunately, n-capture elements can also be studied through nebular spectroscopy of PNe. PNe are excellent laboratories for such investigations: they are easily observed in the optical region, which is home to a multitude of s-process element transitions, including lines from multiple ions of Br, Kr, Rb, and Xe; in addition, nucleosynthesis and dredge-up is complete in these objects, whereas the composition of AGB stars is evolving. On the downside, the emission lines of s-elements are intrinsically very weak even in the brightest PNe, so that deep, high-resolution spectroscopy is required to detect them. Because of these stringent technical requirements, only a few detailed abundance analysis have been published so far (see, e.g., Péquignot & Baluteau 1994; Sharpee et al. 2007; Sterling & Dinerstein 2008). The determination of total abundances is often limited by the fact that only one ion of each element is detected, leading to large and uncertain corrections for unobserved ions.

To improve the accuracy of s-element abundance determinations in PNe, we embarked on an ambitious observational program aimed at detecting multiple ions of several n-capture species in a small sample of about eight PNe. The data gathered will enable us to compute accurate total abundances for the object of the sample, as well as verify the consistency of current ionization correction factors (ICFs) based on photoionization modelling for future, less in-depth studies. In addition, the comparison of different lines of the same ionization species will enable us to assess the quality of the (as yet poorly-tested) atomic data for heavy elements. Both aspects are crucial to hone nebular spectroscopy into an effective tool for studying s-process nucleosynthesis.

Two further scientific goals depend crucially on the availability of a sample of several PNe. On one side, we intend to study the correlation, predicted by current AGB models, between the C/O ratio and the s-process enrichment factors. Additionally, we want to explore the correlation between the pattern of s-element abundances and the mass of the progenitor star, which, according to theory, is modulated by the nuclear reaction activated in each mass range (Karakas, García-Hernández & Lugaro 2012; van Raai et al. 2012).

Given the deep, high-resolution spectroscopy required to detect optical n-capture element emission lines, such studies naturally reveal numerous weak features of other species. We have detected more than 750 emission lines in NGC 3918, making ours one of the deepest spectra of a PN ever obtained at such a high spectral resolution. These include forbidden lines of several iron-group and other refractory elements, a multitude of permitted features, and a host of diagnostic lines. We determine abundances for all species for which atomic data are available in addition to n-capture elements. For comparison, available very deep PNe spectra at a comparable high-resolution in the literature are those of e.g. Sharpee et al. (2003) who detected ∼800 lines in the PN IC 418, and Sharpee et al. (2007) who detected between ∼600 and ∼900 lines in four Galactic PNe.

In this paper, we describe the results for the first PN of our sample, NGC 3918. The paper is organized as follows: in Section 2 we describe the observations and the data reduction; in Section 3 we present the table of identified lines as well as the reddening correction; in Sections 4 and 5 we compute the physical conditions and the ionic and total chemical abundances. Finally, in Section 6 we discuss our results and draw some conclusions. The work is summarized in Section 7.

Table 1. Journal of observations.

Telescope	Date	Δλ (Å)	Exp. time (s)	Seeing (arcsec)
8.2 m VLT	2013-03-08	B1: 3100–3885	60, 6×850	1.0 –1.4
”	”	B2: 3750–4995	60, 6×850	1.0–1.2
”	”	R1: 4785–6805	60, 6×850	1.0–1.4
”	”	R2: 6700–10 420	60, 6×850	1.0–1.2

2 OBSERVATIONS AND DATA REDUCTION

The spectra of NGC 3918 were taken with the Ultraviolet-Visual Echelle Spectrograph (UVES; D'Odorico et al. 2000), attached to the 8.2-m Kueyen (UT2) Very Large Telescope (VLT) at Cerro Paranal Observatory (Chile) in service mode on 2013 March 8. The observations were taken under clear/dark conditions and the seeing remains below 1.5 arcsec during the whole run (see Table 1).

We used two standard settings, DIC1 (346+580) and DIC2 (437+860), in both the red and blue arms of the telescope, covering nearly the full optical range between 3100–10420 Å. In the setting DIC1 (346+580) the dichroic splits the light beam in two wavelengths ranges: 3100–3885 Å in the blue arm and 4785–6805 Å in the red arm; in the setting DIC2 (437+860) the dichroic configuration change to split the light beam in the wavelength ranges: 3750–4995 Åin the blue arm and 6700–10420 Å in the red arm. The wavelength regions 5773–5833 Å and 8540–8650 Å were not observed because of the gap between the two CCDs used in the red arm. Additionally, there are small gaps at the reddest wavelengths which were not observed because the redmost orders do not fit completely within the CCD. The journal of observations is shown in Table 1. The atmospheric dispersion corrector was used to compensate for atmospheric dispersion at the large airmasses the object was observed (between 1.5 and 1.7). The spectra are divided in four spectral ranges (B1, B2, R1, and R2; see Table 1) because the central wavelengths of the two arms were set to two different values to cover the whole optical–near-infrared (NIR) range. We obtained six exposures of 850 s each in each configuration that were taken consecutively following the sequence DIC1 (346+580) → DIC2 (437+860), giving a total exposure time of 1.42 h in each configuration. We have to emphasize that at the end of the observing period, only 42.8 per cent of the total observing time requested was completed. Fortunately, the spectrum was deep enough to reach part of our scientific goals (detection of faint n-capture element lines). Additional single short exposures of 60 s each were taken to obtain non-saturated flux measurements for the brightest emission lines. The slit length was fixed to 10 arcsec in the two bluest spectral ranges (B1 and B2) and 12 arcsec in the two reddest ones (R1 and R2), obtaining an adequate interorder separation. The slit width was set to 1 arcsec, which gives an effective spectral resolution of $\Delta\lambda/\lambda \sim 40\,000$ (6.5 km s^{-1}), which is needed to deblend some important n-capture emission lines from other spectral features (Sharpee et al. 2007). The final one-dimensional spectra analysed in this paper cover an area of 9.35 arcsec^2 common to all spectral ranges. In Fig. 1 we show a high spatial resolution Hα

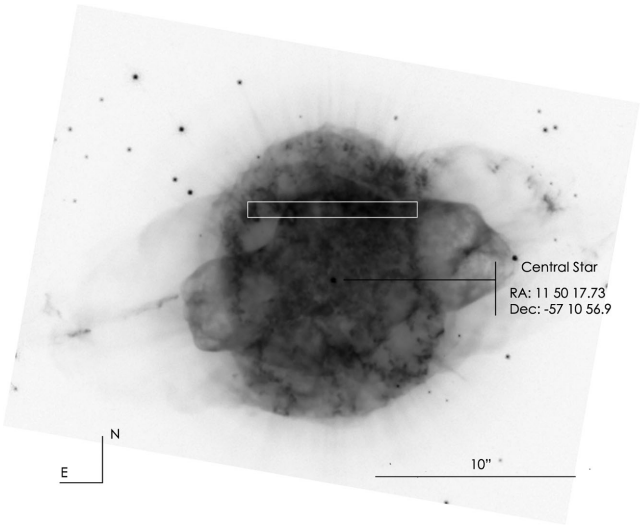

Figure 1. Deep *HST* H α image of NGC 3918. The position of the central star and its coordinates are shown. The slit position is indicated as a white rectangular box. The slit size is 10 arcsec × 1 arcsec.

image from the *HST* archive of NGC 3918. The slit centre was set 3.8 arcsec north to the central star of NGC 3918 oriented E–W (PA = 90°), covering the brightest area of NGC 3918.

The raw frames were reduced using the public ESO UVES pipeline (Ballester et al. 2000) under the GASGANO graphic user interface, following the standard procedure of bias subtraction, aperture extraction, background subtraction, flat-fielding, and wavelength calibration. The final products of the pipeline were 2D wavelength-calibrated spectra; our own IDL scripts were used thereafter to collapse the spectra in the spatial direction and obtain our final 1D spectra. The standard star LTT 3218 (Hamuy et al. 1992, 1994) was observed to perform the flux calibration and was also fully reduced with the pipeline. The flux calibration and radial velocity correction were performed using the standard procedures with IRAF[1] (Tody 1993).

3 LINE FLUXES, IDENTIFICATIONS, AND EXTINCTION CORRECTION

We used the *splot* routine of the IRAF package to measure the line intensities. The expansion velocity field of the PN is mapped in the line profile pattern, which evolves from the double-peaked line profile of the lowest ionization species to the simpler profile of the highest ionization species. Hence, the total flux of each line was measured by integrating the profile between two given limits, over a local continuum estimated by eye. Owing to the small area covered by our slit, we could not extract a sky spectrum. However, taking into account the peculiar profile of the emission lines in each range of ionization, it was easy to distinguish telluric emission features from nebular emission lines. The cases in which nebular emission lines are severely blended with sky emission features are labelled in the table of line identifications (Table 2). Finally, several lines are strongly affected by atmospheric features in absorption or by internal reflections by charge transfer in the CCD, rendering their intensities unreliable. In some cases, where we consider we could deblend the line from the non-nebular feature, we decided to report the line flux anyway, and included a label in the line identification table as a note of caution. In Fig. 2, we present an example of the line profiles for different ionic species of several elements to show the effect of the expansion velocity field on the line profiles.

The four different spectral ranges covered in the spectra have overlapping regions at the edges. To produce a homogeneous data set of line flux ratios, all the lines fluxes of a given spectrum were normalized to a particular non-saturated bright emission line located in such overlapping region. The selected lines were H9 λ3835 for the B1 and B2 spectra, [S II] 6731 Å for R1 and R2, and H β for B2 and R1. All line fluxes were eventually referred to H β. Some lines that were saturated in the long exposures were measured in the short ones and rescaled to the H β flux in a similar way.

The final intensity of a given line in the overlapping regions is the average of the values obtained in both spectra. The differences in the fluxes measured for each line in overlapping spectra do not show any systematic trend and, for the brightest lines, are always lower than 10 per cent. The differences found for the faintest lines in the overlapping regions can be slightly larger (∼20–25 per cent), and the final adopted errors for each line take into account these uncertainties. Therefore, the final adopted uncertainties are always larger than the differences found between both ranges. These differences are probably caused by the fact that these lines are in the red and blue extremes of the CCDs, where the flat-field correction might be less reliable. We do not expect our final results to be substantially affected by these effects because only line ratios are used in our analysis.

Thanks to the high ionization of NGC 3918, we detect multiple lines of different excitation stages. More than 750 emission lines were measured; most of the lines are permitted lines of H I, He I, and He II, but there is also a large number of permitted lines of heavier ions, such as O II, O III, O IV, N II, N III, N IV, C II, C III, C IV, Ne II, Ne III, Si II, Si III, Mg I, and Mg II (and, possibly, N V, O V, and S II; see Table 2). We also detect several forbidden and semi-forbidden lines from ions such as [N I], [N II], [O I], [O II], [O III], [F IV], [Ne III], [Ne IV], [Ne V], [Na IV], Mg I], [P II], [S II], [S III], [Cl II], [Cl III], [Cl IV], [Ar III], [Ar IV], [Ar V], [K IV], [K V], [K VI], [Ca V], [Cr II], [Cr III], [Mn IV], [Mn V], [Mn VI],[Fe III], [Fe IV], [Fe V], [Fe VI], [Fe VII], [Co IV], [Ni V], [Cu V], [Cu VI], [Kr III], [Kr IV], [Kr V], [Rb IV], [Rb V], [Xe III], and [Xe IV] (and, tentatively, [Co VI], [Se III], and [Xe VI]). The depth of our spectra allows us to detect lines as faint as $10^{-5} \times I(\mathrm{H}\,\beta)$. The identification and adopted laboratory wavelengths of the lines are based on several previous identifications in the literature (see Clegg et al. 1987; Péquignot & Baluteau 1994; Baluteau et al. 1995; Zhang et al. 2005; Sharpee et al. 2007; García-Rojas, Peña & Peimbert 2009; Fang & Liu 2011; García-Rojas et al. 2012, and references therein). We also made use of Peter van Hoof's Atomic Line List v2.05B18.[2] Details on the identification of n-capture element emission lines are given in Section 3.2.

For the reddening correction, we assumed the standard extinction law for the Milky Way parametrized by Seaton (1979), with $R_v = 3.1$. We selected this parametrization of the extinction law to be consistent with the analysis of Clegg et al. (1987) which is

[1] IRAF is distributed by National Optical Astronomy Observatory, which is operated by Association of Universities for Research in Astronomy, under cooperative agreement with the National Science Foundation.

[2] http://www.pa.uky.edu/∼peter/newpage/

Table 2. Observed and reddening corrected line ratios [$F(\mathrm{H}\,\beta) = 100$] and line identifications in NGC 3918.

λ_0 (Å)	Ion	Mult.	λ_{obs}	V_{rad} (km s^{-1})	$F(\lambda)/F(\mathrm{H}\,\beta)^a$	$I(\lambda)/I(\mathrm{H}\,\beta)^b$	Err(per cent)	Notes
3109.18	[Ar III]	3P–1S	3108.89	−27.97	0.485	0.648	9	
3115.67	O III	3S–3P$_0$	3115.42	−24.06	0.165	0.219	11	
3118.61	[Cl IV]	3P–1S	3118.42	−18.28	0.104	0.138	14	
3121.63	O III	3S–3P$_0$	3121.41	−21.13	2.444	3.249	8	
3132.79	O III	3S–3P$_0$	3132.58	−20.09	53.51	70.93	8	
3187.84	He I	3	3187.50	−31.99	2.492	3.255	8	
3203.10	He II	3.5	3202.89	−19.68	13.62	17.72	8	
3218.19	Ne II	4D$_0$–4F	3217.95	−22.36	0.0845	0.1096	16	
3230.54	N II	3D–3P	3229.87	−62.18	0.0581	0.0751	21	
3241.63	[Na IV]	3P–1D	3241.40	−21.27	0.737	0.950	8	
3260.86	O III	8	3260.64	−20.25	0.223	0.286	9	
3265.33	O III	8	3265.12	−19.28	0.242	0.310	9	
3280.13	N III	2F$_0$–2D	3279.78	−31.98	0.0312	0.0399	35	
3284.45	O III	8	3284.26	−17.34	0.0189	0.0241	:	
3287.65	O III	3P–3P$_0$	3287.31	−30.99	0.0236	0.0301	:	?
3299.39	O III	3	3299.16	−20.90	2.983	3.793	7	
3312.33	O III	3	3312.10	−20.82	7.753	9.828	7	
3323.74	Ne II	7	3323.59	−13.52	0.0242	0.0306	:	
3328.72	N II	3D–3P$_0$	3328.60	−10.80	0.0253	0.0319	:	?
3328.93	N II	3D–3P$_0$	*	*	*	*	*	?
3334.87	Ne II	2	3334.61	−23.38	0.0953	0.1203	14	
3340.77	O III	3	3340.53	−21.54	10.75	13.54	7	
3342.50	[Ne III]	1D–1S	3342.31	−17.04	0.458	0.577	8	
3342.85	[Cl III]	4S$_0$–2P$_0$	*	*	*	*	*	
3345.83	[Ne V]	3P–1D	3345.56	−24.20	21.92	27.58	7	
3349.11	O IV	2P$_0$–2D	3348.84	−24.17	0.0306	0.0384	35	?
3350.92	O III	5P–5P$_0$	3350.58	−30.41	0.0288	0.0362	:	
3353.21	[Cl III]	4S–2P	3352.87	−30.39	0.0456	0.0573	25	
3354.55	He I	8	3354.65	8.92	0.108	0.136	13	
3355.02	Ne II	2	*	*	*	*	*	
3357.70	N III	2S–2P$_0$	3357.20	−35.73	0.0142	0.0178	:	?
3362.24	[Na IV]	3P–1D	3361.99	−22.29	0.220	0.275	9	
3381.21	O IV	4P$_0$–4D	3380.95	−23.06	0.359	0.448	8	
3381.30	O IV	4P$_0$–4D	*	*	*	*	*	
3385.52	O IV	4P$_0$–4D	3385.24	−24.80	0.291	0.363	8	
3390.19	O IV	4P$_0$–4D	3389.98	−18.57	0.0197	0.0246	:	
3396.80	O IV	4P$_0$–4D	3396.53	−23.83	0.0729	0.0908	17	
3403.55	O IV	2P$_0$–2D	3403.26	−25.55	0.282	0.350	8	
3405.72	O III	15	3405.46	−22.89	0.270	0.336	8	
3408.13	O III	15	3407.86	−23.73	0.0775	0.0963	16	
3409.70	O IV	4P$_0$–4D	3409.41	−25.50	0.115	0.142	12	
3411.69	O IV	2P$_0$–2D	3411.44	−21.97	0.484	0.601	7	
3413.63	O IV	2P$_0$–2D	3413.39	−21.08	0.0566	0.0702	21	
3415.26	O III	15	3415.01	−21.95	0.353	0.438	8	
3425.87	[Ne V]	3P–1D	3425.62	−21.88	51.15	63.29	7	
3428.65	O III	15	3428.39	−22.74	3.518	4.352	7	
3430.57	O III	15	3430.32	−21.85	0.426	0.527	8	
3444.07	O III	15	3443.82	−21.76	22.12	27.28	7	
3447.59	He I	7	3447.41	−15.67	0.0948	0.117	14	
3453.30	He I	3P$_0$–3D	3453.05	−21.70	0.0190	0.0234	:	
3454.99	O III	5D$_0$–5F	3454.76	−20.55	0.0351	0.0432	31	?
3456.85	He I	3P$_0$–3D	3456.60	−21.68	0.0222	0.0273	:	
3461.00	He I	3P$_0$–3D	3460.66	−29.46	0.0154	0.0189	:	
3465.94	He I	P$_0$–3D	3465.81	−11.23	0.0540	0.0663	22	
3471.80	He I	44	3471.56	−20.72	0.0398	0.0488	28	
3478.72	N IV	3S–3P$_0$	3478.57	−12.92	0.0817	0.100	16	
3478.97	He I	43	*	*	*	*	*	
3480.35	[Co VI]	5D–3P$_2$	3480.23	−10.35	0.0096	0.0117	:	?
3483.00	N IV	3S–3P$_0$	3482.72	−24.10	0.0268	0.0328	39	
3484.93	N IV	3S–3P$_0$	3484.83	−8.59	0.0142	0.0174	:	*c*
3487.73	He I	42	3487.43	−25.79	0.0499	0.0611	23	
3498.64	He I	40	3498.38	−22.28	0.0654	0.0797	18	
3512.51	He I	38	3512.23	−23.90	0.0869	0.106	15	
3530.50	He I	36	3530.21	−24.63	0.122	0.148	12	

Table 2 – *continued*

λ_0 (Å)	Ion	Mult.	λ_{obs}	V_{rad} (km s^{-1})	$F(\lambda)/F(H\,\beta)^a$	$I(\lambda)/I(H\,\beta)^b$	Err(per cent)	Notes
3554.42	He I	34	3554.13	−24.46	0.147	0.177	10	
3555.60	[Fe VI]	4F–2D	3555.68	6.73	0.0091	0.0109	:	?
3568.50	Ne II	5	3568.33	−14.28	0.129	0.155	11	*c*
–	?	–	3571.09	–	0.0441	0.0531	25	
3574.61	Ne II	5	3574.40	−17.63	0.0300	0.0360	36	
3586.32	[Fe VII]	3P–1G	3586.98	55.15	0.213	0.256	9	
3587.28	He I	31	*	*	*	*	*	
3590.86	C II	23	3590.47	−32.58	0.0211	0.0253	:	
3599.32	He I	30	3599.01	−25.83	0.0173	0.0207	:	
3613.64	He I	6	3613.35	−24.04	0.163	0.195	10	
3634.25	He I	28	3633.95	−24.75	0.309	0.368	8	
3660.28	H I	H32	3659.98	−24.58	0.0877	0.104	15	
3661.22	H I	H31	3660.94	−22.93	0.130	0.154	11	
3662.26	H I	H30	3661.98	−22.92	0.170	0.201	9	
3663.40	H I	H29	3663.13	−22.10	0.205	0.243	9	
3664.68	H I	H28	3664.39	−23.73	0.242	0.286	8	
3664.07	Ne II	1	*	*	*	*	*	
3666.10	H I	H27	3665.82	−22.90	0.280	0.331	8	
3667.68	H I	H26	3667.41	−22.07	0.324	0.384	7	
3669.47	H I	H25	3669.18	−23.70	0.380	0.450	7	
3671.48	H I	H24	3671.19	−23.68	0.420	0.497	7	
3673.76	H I	H23	3673.47	−23.67	0.460	0.544	7	
3674.84	He II	4.44	3674.60	−19.58	0.0117	0.0138	:	
3676.29	He II	4.43	3676.09	−16.31	0.5252	0.6211	7	
3676.37	H I	H22	*	*	*	*	*	
3677.83	He II	4.42	3677.59	−19.56	0.0178	0.0210	:	
3679.36	H I	H21	3679.07	−23.63	0.569	0.672	7	
3679.50	He II	4.41	*	*	*	*	*	
3681.29	He II	4.40	3681.02	−21.99	0.0202	0.0238	:	
3682.81	H I	H20	3682.54	−21.98	0.651	0.769	7	
3683.22	He II	4.39	*	*	*	*	*	
3685.31	He II	4.38	3685.03	−22.78	0.0194	0.0229	:	
3686.57	He II	4.37	3686.55	−1.63	0.742	0.876	6	
3686.83	H I	H19	*	*	*	*	*	
3690.02	He II	4.36	3689.51	−41.44	0.0570	0.0672	20	
3691.56	H I	H18	3691.27	−23.56	0.808	0.953	6	
3692.71	He II	4.35	3692.49	−17.86	0.0198	0.0233	:	
3694.22	Ne II	1	3693.95	−21.91	0.0508	0.0600	22	
3695.62	He II	4.34	3695.31	−25.15	0.0718	0.0847	17	
3697.15	H I	H17	3696.86	−23.50	0.974	1.148	6	
3698.82	He II	4.33	3698.50	−25.94	0.0878	0.104	14	
3702.32	He II	4.32	3702.33	0.81	0.104	0.122	13	
3703.86	H I	H16	3703.56	−24.29	1.169	1.376	6	
3705.04	He I	25	3704.69	−28.33	0.501	0.590	7	
3706.18	He II	4.31	3705.81	−29.92	0.0335	0.0394	32	
3707.25	O III	14	3706.98	−21.84	0.0995	0.117	13	
3709.62	Ne II	1	3709.31	−25.06	0.0288	0.0338	37	
3710.44	He II	4.30	3710.18	−21.01	0.0390	0.0459	28	
3711.97	H I	H15	3711.69	−22.62	1.413	1.660	6	
3713.08	Ne II	5	3712.76	−25.84	0.0496	0.0583	23	
3714.03	O III	14	3713.75	−22.61	0.0404	0.0475	27	
3715.08	O III	14	3714.83	−20.18	0.163	0.192	10	
3715.16	He II	4.29	*	*	*	*	*	
3720.40	He II	4.28	3720.19	−16.92	0.0706	0.0829	17	
3721.83	[S III]	2F	3721.53	−24.17	3.185	3.736	6	
3721.93	H I	H14	*	*	*	*	*	
3726.03	[O II]	1F	3725.71	−25.75	45.52	53.36	6	
3726.26	He II	4.27	*	*	*	*	*	
3728.82	[O II]	1F	3728.48	−27.35	23.12	27.09	6	
3732.83	He II	4.26	3732.55	−22.49	0.0895	0.1048	14	
3734.37	H I	H13	3734.08	−23.29	2.087	2.444	6	
3736.85	O IV	6	3736.56	−23.27	0.219	0.256	8	
3740.22	He II	4.25	3739.95	−21.64	0.0629	0.0736	19	

Table 2 – *continued*

λ_0 (Å)	Ion	Mult.	λ_{obs}	V_{rad} (km s^{-1})	$F(\lambda)/F(\mathrm{H}\,\beta)^a$	$I(\lambda)/I(\mathrm{H}\,\beta)^b$	Err(per cent)	Notes
3744.89	O IV	6	3744.58	−24.80	0.0381	0.0445	29	
3748.60	He II	4.24	3748.36	−19.19	0.0815	0.0952	15	
3750.15	H I	H12	3749.86	−23.17	2.686	3.138	6	
3754.69	O III	2	3754.43	−20.76	0.847	0.989	6	
3756.10	He I	66	3755.85	−19.96	0.0277	0.0323	38	
3757.24	O III	2	3756.98	−20.75	0.266	0.310	8	
3758.14	He II	4.23	3757.97	−13.56	0.101	0.118	13	
3759.87	O III	2	3759.61	−20.73	4.198	4.897	6	
3762.47	O II	$4S_0$–4P	3762.20	−21.52	0.0132	0.0154	32	
3766.26	Ne II	1	3766.03	−18.31	0.0144	0.0168	30	
3768.78	He I	65	3768.78	0.00	0.110	0.129	10	
3769.14	He II	4.22	*	*	*	*	*	
3770.63	H I	H11	3770.33	−23.84	3.494	4.069	6	
3774.02	O III	2	3773.76	−20.66	0.197	0.230	7	
3777.14	Ne II	1	3776.81	−26.18	0.0132	0.0154	:	
3781.72	He II	4.21	3781.42	−23.79	0.110	0.128	10	
3783.22	[Fe V]	5D–3F	3783.39	13.46	0.0090	0.0104	:	
3784.89	He I	64	3784.56	−26.13	0.0214	0.0249	:	
3791.27	O III	2	3791.01	−20.56	0.261	0.303	7	
3794.94	[Fe V]	5D–3F	3795.01	5.54	0.0206	0.0239	:	
3796.33	He II	4.20	3796.05	−22.12	0.122	0.142	9	
3797.63	[S III]	2F	3797.60	−23.67	4.625	5.366	6	
3797.90	H I	H10	*	*	*	*	*	
3805.74	He I	63	3805.43	−24.43	0.0310	0.0359	35	
3806.54	Si III	5	3806.27	−21.27	0.0132	0.0153	:	
3810.99	O III	2	3810.77	−17.31	0.0145	0.0168	:	
3813.50	He II	4.19	3813.26	−18.87	0.159	0.184	8	
3819.61	He I	22	3819.31	−23.55	0.769	0.880	6	
3829.77	Ne II	39	3829.60	−13.30	0.0114	0.0132	22	
3833.57	He I	62	3833.51	−4.70	0.190	0.220	7	
3833.80	He II	4.18	*	*	*	*	*	
3835.39	H I	H9	3835.09	−23.44	6.343	7.320	6	
3839.27	[Fe V]	5D–3F	3839.48	16.39	0.0274	0.0316	39	
3856.02	Si II	1	3855.72	−23.33	0.0334	0.0384	32	
3858.07	He II	4.17	3857.81	−20.21	0.196	0.226	7	
3862.59	Si II	1	3862.31	−21.74	0.0706	0.0811	17	
3868.75	[Ne III]	1F	3868.45	−23.25	99.45	114.4	6	
3882.19	O II	12	3881.97	−16.99	0.0181	0.0208	16	
3887.44	He II	4.16	3887.19	−19.28	0.282	0.324	6	
3888.65	He I	2	3888.60	−3.84	15.85	18.17	6	
3889.05	H I	H8	*	*	*	*	*	
3891.28	[Fe V]	5D–3F	3891.44	12.32	0.0403	0.0462	10	
3895.22	[Fe V]	5D–3P	3895.45	17.70	0.0259	0.0296	13	
3911.33	[Fe V]	5D–3F	3911.68	26.81	0.0208	0.0238	14	*d*
3920.68	C II	4	3920.43	−19.12	0.0203	0.0231	15	
3923.48	He II	4.15	3923.22	−19.87	0.301	0.343	6	
3926.53	He I	58	3926.21	−24.44	0.0776	0.0885	7	
3928.90	[Fe VI]	2F–2D	3928.95	3.82	0.0098	0.0112	25	*e*
3945.04	O II	6	3944.71	−25.09	0.0266	0.0303	12	
3945.31	O IV	10	*	*	*	*	*	*d*, ?
3948.01	O III	$3D–3P_0$	3947.66	−26.59	0.0134	0.0153	20	?
3954.36	O II	6	3954.18	−13.66	0.0155	0.0177	18	
3956.74	O IV	10	3956.51	−17.43	0.0171	0.0194	17	?
3964.73	He I	5	3964.41	−24.20	0.407	0.462	6	
3967.46	[Ne III]	1F	3967.15	−23.43	33.00	37.43	6	
3968.43	He II	4.14	*	*	*	*	*	
3970.07	H I	H7	3969.77	−22.66	13.35	15.14	6	
3973.24	O II	6	3972.97	−20.38	0.0163	0.0184	17	
3994.98	N II	12	3994.72	−19.51	0.0075	0.0084	31	
3997.21	P IV	$3S–3P_0$	3996.93	−21.00	0.0097	0.0110	25	?
3998.63	N III	$2D–2F_0$	3998.37	−19.48	0.0093	0.0105	26	
4003.33	N III	$2D–2F_0$	4003.58	−18.72	0.0230	0.0260	13	
4009.26	He I	55	4008.93	−24.68	0.111	0.125	7	
4023.98	He I	54	4023.47	−38.00	0.0255	0.0287	13	

Table 2 *– continued*

λ_0 (Å)	Ion	Mult.	λ_{obs}	V_{rad} (km s^{-1})	$F(\lambda)/F(\mathrm{H}\,\beta)^a$	$I(\lambda)/I(\mathrm{H}\,\beta)^b$	Err(per cent)	Notes
4025.60	He II	4.13	4025.76	11.91	1.801	2.026	6	
4026.21	He I	18	*	*	*	*	*	
4041.31	N II	39	4041.07	−17.80	0.0183	0.0205	16	
4043.53	N II	39	4043.32	−15.57	0.0097	0.0109	25	
4060.22	[F IV]	3P–1D	4059.89	−24.37	0.0329	0.0369	11	
4060.60	O II	97	*	*	*	*	*	?
4062.94	O II	50	4062.73	−15.49	0.0064	0.0072	35	
4067.94	C III	16	4068.26	23.59	1.796	2.008	6	
4068.60	[S II]	1F	*	*	*	*	*	
4068.91	C III	16	*	*	*	*	*	
4069.62	O II	10	4069.84	16.20	0.294	0.328	6	
4069.89	O II	10	*	*	*	*	*	
4070.26	C III	16	*	*	*	*	*	
4071.24	[Fe V]	5D–3P	4071.83	43.45	0.122	0.137	6	?
4072.15	O II	10	*	*	*	*	*	
4073.98	O III	3P–3D$_0$	4073.74	−17.66	0.0325	0.0363	11	
4075.86	O II	10	4075.92	4.40	0.660	0.737	6	
4076.35	[S II]	1F	*	*	*	*	*	
4078.84	O II	10	4078.56	−20.58	0.0187	0.0209	15	
4081.02	O III	3P–3D$_0$	4080.67	−25.72	0.0187	0.0209	15	
4087.15	O II	48	4086.86	−21.26	0.0137	0.0153	19	
4088.86	Si IV	1	4088.45	−30.06	0.0273	0.0305	12	*d*
4089.29	O II	48	4088.84	−32.99	0.0598	0.0666	8	*d*
4092.93	O II	10	4092.71	−16.11	0.0166	0.0184	17	
4095.64	O II	48	4095.39	−18.30	0.0062	0.0069	36	
4097.22	O II	20	4097.02	−22.69	1.797	2.001	6	
4097.26	O II	48	*	*	*	*	*	
4097.33	N III	1	*	*	*	*	*	
4100.04	He II	4.12	4099.77	−19.74	0.565	0.629	6	
4101.74	H I	H6	4101.42	−23.41	20.95	23.31	6	
4103.43	N III	1	4103.07	−26.33	0.861	0.958	6	
4104.99	O II	20	*	*	*	*	*	
4110.79	O II	20	4110.39	−29.17	0.0064	0.0071	35	
4112.02	O II	47	4111.84	−13.14	0.0087	0.0097	27	
4116.10	Si IV	1	4115.79	−22.57	0.0047	0.0052	:	
4119.22	O II	20	4118.97	−18.20	0.0481	0.0534	9	
4120.82	He I	16	4120.41	−29.81	0.226	0.251	6	*d*
4122.62	[K V]	4S$_0$–2D$_0$	4122.25	−26.92	0.0725	0.0804	7	
4128.55	C III	3G–3H	4128.42	−9.43	0.0337	0.0374	11	
4132.80	O II	19	4132.58	−15.94	0.0139	0.0154	19	
4141.93	O II	106	4142.11	13.01	0.0170	0.0188	17	
4142.07	O II	106	*	*	*	*	*	
4143.76	He I	53	4143.40	−26.04	0.210	0.232	6	
4145.90	O II	106	4145.77	−9.39	0.0187	0.0207	15	
4146.08	O II	106	*	*	*	*	*	
4153.30	O II	19	4153.05	−18.05	0.0233	0.0258	13	
4156.50	C III	3D–3F$_0$	4156.12	−27.40	0.0478	0.0528	9	*d*
4156.53	O II	19	*	*	*	*	*	
4163.32	[K V]	4S$_0$–2D$_0$	4162.95	−26.62	0.0925	0.102	7	
4168.97	He I	52	4168.68	−20.86	0.0407	0.0449	9	
4169.22	O II	19	*	*	*	*	*	
4180.60	[Fe V]	5D–3P	4180.93	23.67	0.0154	0.0170	18	
4185.45	O II	36	4185.10	−25.08	0.0367	0.0404	10	
4186.90	C III	18	4186.59	−22.20	0.154	0.169	6	
4189.79	O II	36	4189.50	−20.75	0.0364	0.0401	10	
4199.83	He II	4.11	4199.56	−19.28	0.890	0.978	5	*d*
4201.40	[Mn V]	4F–2D	4201.42	1.43	0.0081	0.0089	29	
4219.76	Ne II	52	4219.48	−19.88	0.0095	0.0104	26	
4227.20	[Fe V]	2F	4227.34	9.90	0.137	0.150	6	
4229.02	C IV	2G–2F	4228.84	−12.77	0.0146	0.0160	18	
4236.91	N II	48	4237.24	23.35	0.0539	0.0590	8	
4237.05	N II	48	*	*	*	*	*	
4241.78	N II	48	4241.65	−9.18	0.0187	0.0204	15	
4253.90	O II	109	4253.60	−21.13	0.0186	0.0203	15	*d*

Table 2 – *continued*

λ_0 (Å)	Ion	Mult.	λ_{obs}	V_{rad} (km s^{-1})	$F(\lambda)/F(\mathrm{H}\,\beta)^a$	$I(\lambda)/I(\mathrm{H}\,\beta)^b$	Err(per cent)	Notes
4253.91	O II	109	*	*	*	*	*	
4261.47	[Cu VI]	3H–1D	4261.18	−20.41	0.0187	0.0205	15	?
4267.15	C II	6	4266.89	−18.25	0.433	0.473	5	
4275.55	O II	67	4275.42	−9.11	0.0332	0.0362	11	*f*
4281.32	O II	53	4281.14	−12.58	0.0090	0.0098	27	
4281.45	O II	53	*	*	*	*	*	
4282.96	O II	67	4282.97	0.72	0.0220	0.0239	14	
4283.25	O II	67	*	*	*	*	*	
4283.72	O II	67	*	*	*	*	*	
4284.01	O II	67	*	*	*	*	*	
4285.69	O II	78	4285.39	−20.97	0.0097	0.0106	25	
4288.82	O II	53	4288.57	−17.48	0.0043	0.0047	:	
4291.25	O II	55	4291.00	−17.47	0.0088	0.0096	27	
4292.21	O II	78	4292.06	−10.47	0.0098	0.0107	25	
4294.78	S II	49	4294.55	−16.05	0.0263	0.0286	12	
4294.92	O II	54	*	*	*	*	*	
4303.61	O II	65	4303.51	−6.97	0.0287	0.0313	12	
4303.82	O II	53	*	*	*	*	*	
4317.14	O II	2	4316.94	−13.90	0.0176	0.0192	16	
4319.63	O II	2	4319.33	−20.81	0.0145	0.0157	19	
4325.56	C III	$1P_0$–1D	4325.43	−22.84	0.0216	0.0234	14	
4325.76	O II	2	*	*	*	*	*	
4332.71	O II	65	4332.48	−15.91	0.0106	0.0115	23	
4336.83	O II	2	4336.64	−13.13	0.0098	0.0107	25	
4338.67	He II	4.10	4338.39	−19.33	1.154	1.251	5	
4340.47	H I	H5	4340.13	−23.51	41.01	44.44	5	
4344.28	O IV	–	4343.66	−42.79	0.0388	0.0420	10	?
4345.56	O II	2	4345.28	−18.63	0.0204	0.0221	14	
4347.41	O II	2D–$2D_0$	4347.17	−16.57	0.0078	0.0084	30	
4349.43	O II	2	4349.13	−20.70	0.0485	0.0525	9	
4363.21	[O III]	2F	4362.86	−24.06	19.63	21.21	5	
4366.89	O II	2	4366.65	−16.49	0.0532	0.0574	8	
4366.99	O III	F[5/2]–G[7/2]	*	*	*	*	*	
4368.77	[Co IV]	5D–$3P_2$	4368.38	−26.77	0.0155	0.0167	18	
4369.56	O III	F[5/2]–G[7/2]	4369.33	−15.78	0.0226	0.0244	13	
4375.01	C II	$4P_0$–4D	4374.67	−23.29	0.0123	0.0132	:	?
4376.53	O III	F[7/2]–G[9/2]	4376.24	−19.84	0.0314	0.0338	11	
4379.11	N III	18	4378.91	−13.67	0.149	0.160	6	
4379.60	O III	F[7/2]–G[9/2]	*	*	*	*	*	
4387.93	He I	51	4387.57	−24.62	0.366	0.394	5	
4391.94	Ne II	55e	4392.38	30.03	0.0982	0.106	6	*d*
4408.27	O III	46a	4408.00	−18.36	0.0126	0.0135	21	
4409.30	Ne II	55e	4409.04	−17.66	0.0156	0.0167	18	
4414.85	O III	46a	4414.57	−19.03	0.0477	0.0511	9	
4414.90	O II	5	*	*	*	*	*	
4416.97	O II	5	4416.60	−25.12	0.0270	0.0290	12	
4428.54	Ne II	57	4428.18	−24.36	0.0102	0.0109	24	
4431.42	[Mn V]	4F–2P	4430.85	−38.55	0.0076	0.0082	30	?
4432.74	N II	55a	4432.55	−12.88	0.0045	0.0048	:	
4434.61	O III	G[9/2]–$H[11/2]_0$	4434.27	−22.98	0.108	0.115	6	*d*
4437.55	He I	50	4437.19	−24.31	0.0489	0.0523	8	
4448.15	O III	G[9/2]–$H[11/2]_0$	4447.76	−26.30	0.0208	0.0221	14	
4452.38	O II	5	4452.54	10.78	0.0503	0.0535	8	
4452.82	O III	G[9/2]–$H[9/2]_0$	*	*	*	*	*	
4454.03	O III	D[5/2]–F[7/2]	4453.76	−18.18	0.0155	0.0165	18	
4458.55	O III	D[5/2]–F[7/2]	4458.41	−9.39	0.0468	0.0498	9	
4465.41	O II	94	4465.10	−20.82	0.0194	0.0206	15	
4467.92	O II	94	4467.56	−24.15	0.0096	0.0102	25	
4469.37	O II	4D–4P	4469.06	−20.80	0.0077	0.0081	30	
4471.47	He I	14	4471.14	−22.13	3.117	3.310	5	
4475.20	O III	45b	4474.89	−20.77	0.0131	0.0139	20	
4481.21	Mg II	4	4481.33	8.04	0.0416	0.0441	9	*d*
4491.22	C II	$2F_0$–2G	4490.96	−18.03	0.0165	0.0174	17	
4491.23	O II	86a	*	*	*	*	*	

Table 2 *– continued*

λ_0 (Å)	Ion	Mult.	λ_{obs}	V_{rad} (km s^{-1})	$F(\lambda)/F(H\,\beta)^a$	$I(\lambda)/I(H\,\beta)^b$	Err(per cent)	Notes
4510.92	[K IV]	1D–1S	4510.57	−23.27	0.0833	0.0879	7	
4510.92	N III	3	*	*	*	*	*	
4514.85	N III	3	4514.53	−21.27	0.0282	0.0297	12	
4516.79	C III	3P–3S	4516.48	−20.58	0.0079	0.0083	29	
4518.14	N III	3	4517.84	−19.93	0.0187	0.0197	15	
4523.56	N III	3	4523.23	−21.88	0.0216	0.0227	14	
4530.41	N II	58b	4530.41	0.00	0.0193	0.0203	15	
4530.86	N III	3	*	*	*	*	*	
4534.58	N III	3	4534.19	−25.80	0.0317	0.0333	11	
4539.70	N III	12	4539.27	−28.41	0.0179	0.0188	16	
4541.59	He II	4.9	4541.29	−19.79	1.585	1.662	5	
4544.84	N III	12	4544.47	−24.38	0.0311	0.0326	11	
4546.33	N III	4S–4P$_0$	4545.96	−24.41	0.0033	0.0035	:	
4549.04	[Mn IV]	a5D–a3F	4548.82	−14.51	0.0059	0.0061	37	
4552.52	N II	58a	4552.32	−13.18	0.0066	0.0069	34	
–	?	–	4554.64	–	0.0036	0.0038	:	
4562.60	Mg I]	1	4562.19	−26.95	0.096	0.101	6	
4571.10	Mg I]	1	4570.69	−26.90	0.423	0.442	5	*d*
4587.72	O III	3P–3P$_0$	4587.23	−32.04	0.0046	0.0048	:	
4590.97	O II	15	4590.66	−20.25	0.0368	0.0383	10	
4595.95	O II	15	4595.85	−6.53	0.0305	0.0317	11	
4596.18	O II	15	*	*	*	*	*	
4602.13	O II	92b	4601.74	−25.38	0.0080	0.0083	29	
4603.74	N V	2S–2P$_0$	4603.43	−20.19	0.0056	0.0058	38	?
4606.33	N IV	3G–3H$_0$	4606.12	−13.67	0.0734	0.0762	7	
4613.68	O II	92b	4613.15	−34.46	0.0032	0.0034	:	
4621.39	N II	5	4620.18	−78.51	0.0152	0.0158	18	*f*
4624.22	C III	3H$_0$–3I	4624.02	−12.98	0.0041	0.0042	:	?
4624.93	[Ar V]	1D–1S	4625.04	7.12	0.0472	0.0489	9	
4630.54	N II	5	4630.19	−22.67	0.0246	0.0255	13	
4631.89	O IV	2G–2H$_0$	4631.73	−10.37	0.148	0.153	6	
4634.14	N III	2	4633.80	−22.02	1.772	1.833	5	
4638.86	O II	1	4638.70	−10.32	0.110	0.114	6	
4640.64	N III	2	4640.29	−22.62	3.543	3.663	5	
4641.81	O II	1	4641.54	−17.44	0.500	0.517	5	
4641.85	N III	2	*	*	*	*	*	
4643.30	[Mn IV]	b3G–d3F	4643.04	−16.77	0.0274	0.0283	12	
4647.42	C III	1	4647.04	−24.51	0.228	0.235	5	*c*
4649.13	O II	1	4648.82	−19.99	0.212	0.219	5	
4649.97	O III	3P–3P$_0$	4650.21	15.46	0.224	0.231	5	
4650.25	C III	1	*	*	*	*	*	
4650.84	O II	1	*	*	*	*	*	
4651.47	C III	1	*	*	*	*	*	
4657.55	C IV	2F–2G	4657.29	−16.72	0.0872	0.0899	6	
4658.05	[Fe III]	3F	4658.14	−3.87	0.232	0.240	5	
4658.20	C IV	2G–2H	*	*	*	*	*	
4661.63	O II	1	4661.19	−28.30	0.111	0.114	6	*d*
4665.86	C III	–	4665.31	−35.33	0.0205	0.0211	14	
4668.87	O III	3P–3P$_0$	4668.43	−28.25	0.0156	0.0161	17	*c*
4673.48	O III	3P–3P$_0$	4673.39	−5.76	0.0193	0.0198	15	
4676.24	O II	1	4675.87	−23.73	0.0492	0.0506	8	
4679.83	N III	2P$_0$–2P	4679.61	−14.11	0.0248	0.0255	13	
4685.68	He II	3.4	4685.41	−17.28	46.73	47.98	5	
4688.83	N IV	3D–3P$_0$	4688.49	−21.74	0.0156	0.0160	17	?
4688.99	N IV	3P$_0$–3D	*	*	*	*	*	?
4701.62	[Fe III]	3F	4701.16	−29.33	0.0111	0.0114	22	
4707.22	[Mn IV]	b3G–d3F	4706.86	−22.95	0.0143	0.0147	19	
4711.37	[Ar IV]	1F	4711.02	−22.28	6.702	6.856	5	
4713.14	He I	12	4712.79	−22.27	0.521	0.533	5	
4714.36	[Ne IV]	2D–2P	4713.91	−28.60	0.608	0.622	5	
4715.80	[Ne IV]	2D–2P	4715.35	−28.59	0.160	0.164	6	
4724.15	[Ne IV]	1F	4723.81	−21.57	0.664	0.678	5	
4725.62	[Ne IV]	1F	4725.25	−23.48	0.557	0.568	5	
4740.17	[Ar IV]	1F	4739.86	−19.61	8.369	8.525	5	

Table 2 *– continued*

λ_0 (Å)	Ion	Mult.	λ_{obs}	V_{rad} (km s^{-1})	$F(\lambda)/F(\mathrm{H}\,\beta)^a$	$I(\lambda)/I(\mathrm{H}\,\beta)^b$	Err(per cent)	Notes
4754.69	[Fe III]	3F	4754.10	−37.20	0.0049	0.0050	:	
4769.43	[Fe III]	3F	4769.11	−20.14	0.0062	0.0063	35	
4802.70	C II	17.08	4802.22	−29.96	0.0168	0.0169	17	
4859.32	He II	4.8	4859.00	−19.73	2.323	2.324	5	
4861.33	H I	H4	4860.95	−23.43	100.0	100.0	5	
4881.00	[Fe III]	2F	4880.60	−24.56	0.0166	0.0165	17	
4921.93	He I	48	4921.53	−24.39	0.876	0.869	5	
4924.50	[Fe III]	2F	4924.23	−16.44	0.0169	0.0168	16	
4924.53	O II	28	*	*	*	*	*	
4930.50	[Fe III]	2F	4930.85	−28.56	0.180	0.178	5	
4931.32	[O III]	1F	*	*	*	*	*	
4958.91	[O III]	1F	4958.55	−21.79	526.0	518.5	5	
4985.90	[Fe III]	2F	4984.59	−78.79	0.0064	0.0063	:	?
4987.20	[Fe III]	2F	4986.71	−29.47	0.0116	0.0114	:	
5006.84	[O III]	1F	5006.47	−22.13	1596	1563	5	
5015.68	He I	4	5015.29	−23.32	1.281	1.253	5	*d*
5040.72	N II	19	5040.46	−15.48	0.0840	0.0818	6	*d*
5055.98	Si II	5	5055.86	−7.12	0.0340	0.0330	9	*d*
5058.85	N III	27	5058.20	−38.52	0.0097	0.0094	22	
5121.82	C II	12	5121.53	−16.98	0.0140	0.0135	16	
5131.17	[Ni V]	3F–1D	5130.65	−30.39	0.0784	0.0755	6	
5145.75	[Fe VI]	4F–2G	5145.63	−7.00	0.0798	0.0768	6	*f*
5147.87	N III	2G–2H$_0$	5147.61	−15.16	0.0274	0.0264	10	
5148.90	O III	G[7/2]–1F$_0$	5148.24	−38.43	0.0096	0.0092	22	?
–	?	–	5150.60	–	0.0170	0.0163	14	
5158.41	[Fe VII]	3F–3P	5158.48	4.06	0.0304	0.0292	10	*g*
5159.94	O II	2P$_0$–2P	5159.45	−28.46	0.0113	0.0108	19	*g*, ?
5176.04	[Fe VI]	4F–2G	5176.17	7.52	0.0599	0.0574	7	
5179.72	N II	70	5179.45	−15.63	0.0129	0.0124	17	
5191.82	[Ar III]	3F	5191.31	−29.44	0.214	0.204	5	
5197.90	[N I]	1F	5197.43	−27.09	0.391	0.373	5	
5200.26	[N I]	1F	5199.80	−26.52	0.266	0.254	5	
5249.11	C III	23	5248.71	−22.84	0.0043	0.0041	:	
5270.40	[Fe III]	1F	5270.07	−18.78	0.0135	0.0128	17	
5275.79	[Fe VII]	3F–3P	5276.27	27.27	0.0073	0.0069	27	
5277.80	[Fe VI]	4F–4P	5277.66	−7.93	0.0172	0.0163	14	
5304.55	C III	46	5303.89	−37.29	0.0124	0.0117	18	
5304.93	C III	46	5304.65	−15.84	0.0159	0.0150	15	
5309.11	[Ca V]	3P–1D	5308.89	−12.41	0.0991	0.0933	6	
5322.99	[Cl IV]	1D–1S	5322.66	−18.59	0.0596	0.0560	7	
5335.18	[Fe VI]	4F–4P	5335.13	−2.83	0.0538	0.0505	7	
5342.38	C II	17.06	5342.03	−19.65	0.0268	0.0251	11	
5346.02	[Kr IV]	1F	5345.60	−23.55	0.112	0.105	6	
5363.37	[Rb V]	–	5363.39	1.12	0.0048	0.0045	38	
5370.29	[Fe VI]	4F–2G	5370.25	−2.24	0.0054	0.0051	34	
5411.52	He II	4.7	5411.17	−19.40	3.969	3.691	5	
5412.00	[Fe III]	1F	*	*	*	*	*	
5424.22	[Fe VI]	4F–4P	5424.10	−6.64	0.0363	0.0337	9	
5426.64	[Fe VI]	4F–4P	5426.36	−15.48	0.0175	0.0163	14	
–	?	–	5450.62	–	0.0027	0.0025	:	
5460.99	[Cu V]	4F–4P	5460.50	−26.91	0.0027	0.0025	:	?
–	?	–	5464.91	–	0.0065	0.0060	30	
–	?	–	5467.17	–	0.0034	0.0032	:	
–	?	–	5468.35	–	0.0050	0.0046	37	
5470.68	C IV	2G–2F	5470.27	−22.48	0.0232	0.0214	12	
5484.84	[Fe VI]	4F–4P	5484.83	−0.53	0.0316	0.0291	10	
–	?	–	5487.87	–	0.0052	0.0048	36	
5517.71	[Cl III]	1F	5517.24	−25.52	0.656	0.602	5	
5537.88	[Cl III]	1F	5537.39	−26.51	0.979	0.896	5	
5577.34	[O I]	3F	5576.50	−45.15	0.0516	0.0470	8	
5592.37	O III	5	5591.92	−24.14	0.119	0.108	6	
5602.44	[K VI]	3P–1D	5601.76	−36.40	0.0052	0.0048	35	
5604.99	N IV	3P$_0$–3D	5604.56	−23.01	0.0011	0.0010	:	
5622.30	N IV	3P$_0$–3D	5621.82	−25.60	0.0082	0.0074	25	

Table 2 – *continued*

λ_0 (Å)	Ion	Mult.	λ_{obs}	V_{rad} (km s^{-1})	$F(\lambda)/F(H\,\beta)^a$	$I(\lambda)/I(H\,\beta)^b$	Err(per cent)	Notes
5631.10	[Fe VI]	4F–4P	5630.81	−15.44	0.0427	0.0386	8	
–	?	–	5659.80	–	0.0114	0.0103	19	
5666.64	N II	3	5666.28	−19.07	0.0208	0.0187	13	
5676.02	N II	3	5675.61	−21.66	0.0086	0.0078	24	
5677.00	[Fe VI]	4F–4P	5676.79	−11.09	0.0381	0.0342	9	
5679.56	N II	3	5679.21	−18.48	0.0459	0.0411	8	
5685.35	[Fe IV]	4P–4F	5684.90	−23.74	0.0113	0.0102	19	
5686.21	N II	3	*	*	*	*	*	
5691.98	[Mn V]	4F–2G	5691.67	−16.33	0.0113	0.0101	20	
5701.82	[Mn V]	4F–2G	5701.61	−11.04	0.0196	0.0175	13	
5709.21	[Xe IV]	–	5708.56	−34.13	0.0073	0.0065	27	
5710.76	N II	3	5710.37	−20.46	0.0079	0.0071	26	
5720.71	[Fe VII]	3F–1D	5720.89	9.44	0.0635	0.0566	7	
5726.45	He II	5.67	5725.94	−26.72	0.0013	0.0011	:	
5727.43	He II	5.66	5727.09	−17.82	0.0016	0.0015	:	
5728.45	He II	5.65	5728.04	−21.47	0.0029	0.0025	:	
5729.53	He II	5.64	5729.12	−21.44	0.0029	0.0026	:	
5730.65	He II	5.63	5730.28	−19.36	0.0037	0.0033	:	
5731.83	He II	5.62	5731.47	−18.82	0.0033	0.0029	:	
5733.07	He II	5.61	5732.65	−21.96	0.0036	0.0032	:	
5734.38	He II	5.60	5734.01	−19.35	0.0044	0.0039	:	
5735.48	[Fe IV]	4P–4F	5735.34	−7.33	0.0047	0.0042	39	?
5735.75	He II	5.59	*	*	*	*	*	
5737.19	He II	5.58	5736.77	−21.94	0.0059	0.0053	32	
5738.71	He II	5.57	5738.26	−23.52	0.0046	0.0041	39	
5739.73	Si III	4	5739.85	6.27	0.0057	0.0051	33	
5740.32	He II	5.56	*	*	*	*	*	
5742.01	He II	5.55	5741.60	−21.39	0.0062	0.0055	31	
5743.80	He II	5.54	5743.38	−21.92	0.0070	0.0062	28	
5745.69	He II	5.53	5745.30	−20.36	0.0057	0.0050	33	
5747.70	He II	5.52	5747.30	−20.89	0.0088	0.0078	24	
5749.82	He II	5.51	5749.48	−17.72	0.0079	0.0070	26	
5752.08	He II	5.50	5751.73	−18.25	0.0076	0.0067	26	
5754.47	He II	5.49	5754.08	−20.33	1.886	1.675	6	
5754.64	[N II]	3F	*	*	*	*	*	
5757.02	He II	5.48	5756.66	−18.74	0.0074	0.0066	27	
5758.11	C III	$1F_0$–1D	5757.85	−13.53	0.0021	0.0019	:	?
5759.55	[Rb IV]	–	5759.21	−17.69	0.0145	0.0129	16	
5759.74	He II	5.47	*	*	*	*	*	
5762.64	He II	5.46	5762.32	−16.66	0.0109	0.0097	20	
5837.06	He II	5.32	5836.65	−21.07	0.0291	0.0255	10	
5846.66	He II	5.31	5846.27	−20.01	0.0305	0.0268	10	
5846.77	[Xe III]	–	*	*	*	*	*	?
5857.26	He II	5.30	5856.87	−19.94	0.0349	0.0306	9	
5861.00	[Mn V]	4F–2G	5860.94	−3.07	0.0249	0.0218	11	
5865.40	C IV	$2K_0$–2I	5864.94	−23.51	0.0061	0.0054	31	
5867.74	[Kr IV]	4S–2D	5867.29	−23.00	0.149	0.131	6	
5869.02	He II	5.29	5868.62	−20.43	0.0310	0.0271	10	
5875.64	He I	11	5875.19	−22.97	11.10	9.706	6	
5882.13	He II	5.28	5881.73	−20.38	0.0363	0.0317	9	
5885.40	[Mn V]	4F–2G	5885.34	−3.06	0.0229	0.0200	12	
5896.78	He II	5.27	5896.28	−25.42	0.0486	0.0424	8	*h*
5913.24	He II	5.26	5912.84	−20.30	0.0474	0.0412	8	
5931.83	He II	5.25	5931.43	−20.21	0.0547	0.0475	8	
5952.93	He II	5.24	5952.53	−20.17	0.0631	0.0547	7	
5977.03	He II	5.23	5976.63	−20.06	0.0704	0.0609	7	
5990.10	[Mn V]	4F–4P	5989.24	−43.04	0.0044	0.0038	:	?
6004.73	He II	5.22	6004.31	−20.97	0.0794	0.0684	7	
6024.40	[Mn V]	4F–4P	6024.44	1.99	0.0058	0.0050	33	
6036.70	He II	5.21	6036.38	−15.91	0.0909	0.0781	7	
6074.10	He II	5.20	6073.79	−15.30	0.105	0.0901	7	
6083.30	[Mn V]	4F–4P	6083.28	−0.99	0.0148	0.0126	16	
6086.29	[Fe VII]	3F–1D	6086.51	10.82	0.121	0.103	7	
6086.40	[Ca V]	3F–1D	*	*	*	*	*	

Table 2 – *continued*

λ_0 (Å)	Ion	Mult.	λ_{obs}	V_{rad} (km s^{-1})	$F(\lambda)/F(\mathrm{H}\,\beta)^a$	$I(\lambda)/I(\mathrm{H}\,\beta)^b$	Err(per cent)	Notes
6101.83	[K IV]	1F	6101.28	−27.04	0.502	0.428	6	
6107.60	N III	$2P_0$–2D	6107.19	−29.94	0.0094	0.0081	22	
6107.80	[Kr IV]	2D–2P	*	*	*	*	*	
–	?	–	6114.12	–	0.0047	0.0040	:	
6118.20	He II	5.19	6117.85	−17.16	0.121	0.103	7	
6130.30	C III	$3H_0$–3G	6129.89	−20.04	0.0114	0.0097	20	
6134.33	Ne III	5P–$5D_0$	6134.15	−8.81	0.0097	0.0082	22	
6134.61	Ne III	5P–$5D_0$	*	*	*	*	*	
6141.48	Ne III	5P–$5D_0$	6141.17	−15.14	0.0090	0.0077	23	
6151.43	C II	16.04	6150.94	−23.89	0.0249	0.0211	12	
6157.60	[Mn V]	4F–4P	6156.97	−30.67	0.0154	0.0131	16	
6166.00	[Mn V]	4F–4P	6165.33	−32.58	0.0109	0.0092	20	
6167.75	N II	36	6167.38	−17.99	0.0046	0.0039	39	
6170.16	N II	36	6170.29	6.31	0.148	0.126	7	
6170.60	He II	5.18	*	*	*	*	*	
6228.60	[K VI]	3P–1D	6227.83	−37.07	0.0126	0.0106	18	
6233.80	He II	5.17	6233.42	−18.27	0.174	0.147	7	
6256.10	[Kr V]	–	6256.04	−2.88	0.0093	0.0078	23	
–	?	–	6272.78	–	0.0185	0.0155	14	
6300.30	[O I]	1F	6299.77	−25.21	6.433	5.389	6	
6310.85	He II	5.16	6311.58	34.67	3.199	2.677	6	
6312.10	[S III]	3F	*	*	*	*	*	
6343.60	[Mn V]	4F–4P	6343.20	−18.90	0.0169	0.0141	15	
6347.11	Si II	2	6346.58	−25.03	0.0364	0.0303	10	
6363.78	[O I]	1F	6363.21	−26.85	2.238	1.864	6	
6371.36	Si II	2	6370.86	−23.53	0.0759	0.0631	8	
6393.60	[Mn V]	4F–4P	6393.31	−13.60	0.0255	0.0212	12	
6406.30	He II	5.15	6405.96	−15.90	0.258	0.214	7	
6408.10	C IV	9/17	6407.72	−17.78	0.0027	0.0023	:	
6408.80	[Xe VI]	–	6408.39	−19.18	0.0048	0.0039	:	?
6435.10	[Ar V]	3P–1D	6434.56	−25.16	1.121	0.927	7	
6461.95	C II	17.04	6461.44	−23.67	0.0598	0.0493	8	
6515.70	C II	2G–$2F_0$	6515.58	−5.53	0.0330	0.0271	10	
6527.11	He II	5.14	6526.67	−20.21	0.323	0.265	7	
6548.03	[N II]	1F	6547.51	−23.81	30.83	25.25	7	
6560.00	He II	4.6	6559.68	−14.62	7.701	6.301	7	
6562.82	H I	H3	6562.31	−23.29	322.3	263.6	7	
6578.05	C II	2	6577.64	−18.67	0.218	0.178	7	
6583.41	[N II]	1F	6582.87	−24.59	95.06	77.63	7	
6601.00	O IV	2D–$2D_0$	6600.40	−27.25	0.0074	0.0060	27	?
6641.03	O II	4	6640.57	−20.77	0.0040	0.0032	:	
6678.15	He I	46	6677.63	−23.35	3.255	2.638	7	
6683.20	He II	5.13	6682.76	−19.76	0.410	0.332	7	
6716.47	[S II]	2F	6715.89	−25.89	3.640	2.941	7	
6721.39	O II	4	6720.96	−19.19	0.0064	0.0052	31	
6727.48	C III	3	6727.03	−20.06	0.0034	0.0027	:	
6730.85	[S II]	2F	6730.27	−25.84	6.617	5.340	7	
6734.00	C II	21	6733.52	−21.37	0.0036	0.0029	:	
6739.80	[Fe IV]	4G–2I	6739.50	−13.34	0.0035	0.0028	:	*i*, ?
6742.15	C III	3	6741.69	−20.45	0.0028	0.0022	:	
6744.39	C III	3	6743.93	−20.45	0.0162	0.0130	16	
6746.80	C IV	9/16	6746.45	−15.55	0.0055	0.0044	34	
6762.17	C III	3	6761.74	−19.05	0.0033	0.0026	:	
6779.93	C II	14	6779.59	−15.05	0.0318	0.0256	11	
6780.59	C II	14	*	*	*	*	*	
6783.91	C II	14	6783.42	−21.67	0.0029	0.0023	:	
6787.22	C II	14	6786.73	−21.66	0.0072	0.0058	27	
6791.47	C II	14	6790.98	−21.64	0.0114	0.0092	21	
6795.00	[K IV]	1F	6794.47	−23.38	0.119	0.0955	8	
6800.69	C II	14	6800.21	−21.16	0.0065	0.0052	30	
6826.70	[Kr III]	–	6826.66	−1.76	0.0354	0.0284	12	
6827.88	He I	1/16	*	*	*	*	*	
6849.92	[Mn VI]	1F	6849.61	−13.56	0.0163	0.0130	17	?
6890.88	He II	5.12	6890.49	−16.95	0.4829	0.3852	7	

Table 2 – *continued*

λ_0 (Å)	Ion	Mult.	λ_{obs}	V_{rad} (km s^{-1})	$F(\lambda)/F(H\,\beta)^a$	$I(\lambda)/I(H\,\beta)^b$	Err(per cent)	Notes
6895.10	O II	4F–4D	6894.72	−16.52	0.0185	0.0147	16	
6906.44	O II	4F–4D	6906.08	−15.62	0.0064	0.0051	29	
6933.89	He I	1/13	6933.13	−32.87	0.0057	0.0045	31	
–	?	–	6958.81	–	0.0085	0.0068	25	*i*
6975.60	C III	3H$_0$–3I	6975.19	−17.63	0.0025	0.0020	:	
6989.47	He I	1/12	6989.01	−19.75	0.0082	0.0065	25	
7004.10	O IV	2P$_0$–2P	7003.93	−7.27	0.0031	0.0025	:	
7005.67	[Ar V]	3P–1D	7005.21	−19.68	2.682	2.123	7	
–	?	–	7030.44	–	0.0052	0.0041	33	
7032.30	O IV	12.01	7031.85	−19.17	0.0037	0.0029	:	
–	?	–	7046.36	–	0.0055	0.0044	32	
7053.60	O IV	12.01	7053.40	−8.51	0.0197	0.0155	16	
–	?	–	7058.79	–	0.0146	0.0115	18	
7062.26	He I	1/11	7061.82	−18.68	0.0565	0.0445	10	
7065.28	He I	10	7064.68	−25.44	5.760	4.539	7	
–	?	–	7102.30	–	0.0077	0.0061	26	
7112.48	C II	20	7112.41	−2.94	0.0090	0.0071	24	
7113.04	C II	20	*	*	*	*	*	
7115.63	C II	20	7115.04	−24.85	0.0086	0.0068	25	
7135.78	[Ar III]	1F	7135.25	−22.26	26.79	21.01	7	
7160.61	He I	1/10	7160.12	−20.51	0.0173	0.0136	17	
7170.62	[Ar IV]	2F	7170.08	−22.58	0.462	0.362	8	
7177.50	He II	5.11	7176.95	−22.97	0.566	0.443	8	
7206.40	C IV	9/15	7205.91	−20.38	0.0020	0.0016	:	*e*
7231.34	C II	3	7230.93	−16.98	0.0836	0.0651	9	
7236.42	C II	3	7236.98	23.20	0.550	0.429	8	
7237.17	C II	3	*	*	*	*	*	
7237.40	[Ar IV]	2F	*	*	*	*	*	
7262.76	[Ar IV]	2F	7262.43	−13.61	0.411	0.320	8	
7281.35	He I	45	7280.78	−23.48	0.679	0.528	8	
7298.05	He I	1/9	7297.43	−25.46	0.0221	0.0172	15	
7306.85	O III	24.03	7306.58	−11.08	0.0085	0.0066	25	
7307.12	O III	24.03	*	*	*	*	*	
7318.92	[O II]	2F	7319.33	16.80	6.260	4.852	8	
7319.99	[O II]	2F	*	*	*	*	*	
7329.66	[O II]	2F	7329.57	−3.69	5.483	4.247	8	
7330.73	[O II]	2F	*	*	*	*	*	
7414.04	O III	24.03	7413.52	−21.03	0.0043	0.0033	37	
7455.36	O III	24.03	7454.75	−24.53	0.0101	0.0078	23	
7486.59	C III	41	7486.29	−12.01	0.0085	0.0065	25	
7499.85	He I	1/8	7499.25	−23.99	0.0396	0.0303	12	
7504.96	O II	2G–G[5]$_0$	7504.52	−17.57	0.0042	0.0033	37	
7507.20	C III	3H$_0$–3I	7506.87	−13.18	0.0049	0.0037	34	
–	?	–	7509.38	–	0.0037	0.0028	:	
7514.40	C III	3I–3K$_0$	7513.85	−21.94	0.0028	0.0022	:	
7515.99	O III	24.03	7515.48	−20.35	0.0061	0.0047	30	
7519.49	C II	16.08	7519.26	−9.19	0.0039	0.0030	39	
7519.86	C II	16.08	*	*	*	*	*	
7530.54	[Cl IV]	1F	7529.84	−27.88	0.708	0.542	8	
7535.40	[Xe IV]	4S–2D	7534.38	−40.59	0.0100	0.0076	23	
7578.15	C III	35	7577.44	−28.09	0.0063	0.0048	30	
7581.50	N IV	1G–1Ho	7580.69	−32.04	0.0040	0.0031	39	
7582.30	N IV	22	7581.83	−18.57	0.0068	0.0052	28	
7592.00	O V	29	7590.59	−55.69	0.0047	0.0036	35	*g*, ?
7592.28	C III	35	7592.24	−1.56	1.070	0.816	8	
7592.74	He II	5.10	*	*	*	*	*	
7677.40	O IV	20	7675.79	−62.88	0.0321	0.0244	13	
7702.96	N IV	23	7702.80	−6.23	0.0330	0.0250	13	
7726.20	C IV	8.01	7725.65	−21.35	0.201	0.152	9	*i*
7735.84	C IV	2G–2F	7735.33	−19.76	0.0235	0.0178	15	
7751.10	[Ar III]	2F	7750.53	−22.06	6.890	5.208	8	
7816.13	He I	1/7	7815.52	−23.39	0.0577	0.0435	11	
7839.38	O III	3S–3P$_0$	7838.85	−20.26	0.0030	0.0023	:	

Table 2 – *continued*

λ_0 (Å)	Ion	Mult.	λ_{obs}	V_{rad} (km s^{-1})	$F(\lambda)/F(\mathrm{H}\,\beta)^a$	$I(\lambda)/I(\mathrm{H}\,\beta)^b$	Err(per cent)	Notes
7860.40	C IV	9/14	7860.19	−8.01	0.0104	0.0080	22	*i*
7876.03	[P II]	1D–1S	7875.18	−32.34	0.0470	0.0354	11	*f*
8018.90	N III	$2F_0$–2G	8018.33	−21.30	0.0169	0.0126	17	
8019.50	N III	$2F_0$–2G	*	*	*	*	*	
8045.63	[Cl IV]	1F	8045.05	−21.62	1.694	1.263	8	
8160.10	[Cr II]	4G–2D	8159.62	−17.63	0.0379	0.0281	12	
8196.48	C III	43	8196.04	−16.11	0.310	0.230	9	
8236.77	He II	5.9	8236.24	−19.27	1.633	1.204	8	
8267.94	H I	P34	8267.57	−13.42	0.109	0.0804	10	*i*
8271.93	H I	P33	8271.23	−25.34	0.0902	0.0664	10	*e*
8281.12	H I	P31	8280.61	−18.46	0.102	0.0751	10	*e*,*i*
8286.43	H I	P30	8285.96	−17.00	0.150	0.110	9	*i*
8292.31	H I	P29	8291.69	−22.39	0.135	0.0992	9	
8298.83	H I	P28	8298.57	−9.38	0.221	0.163	9	*i*
8306.11	H I	P27	8305.77	−12.30	0.131	0.0960	9	*e*
8314.26	H I	P26	8313.60	−23.81	0.183	0.134	9	*i*
8323.42	H I	P25	8322.81	−21.99	0.192	0.141	9	
8333.78	H I	P24	8333.08	−25.19	0.221	0.162	9	*e*
8345.55	H I	P23	8344.79	−27.30	0.394	0.289	9	*i*
8345.65	He I	7/22	*	*	*	*	*	
8359.00	H I	P22	8358.40	−21.51	0.253	0.185	9	
8361.08	He I	7/21	8361.05	−1.09	0.0885	0.0647	10	
8374.48	H I	P21	8373.86	−22.20	0.275	0.201	9	
8386.38	N III	5.01	8385.93	−16.09	0.0413	0.0301	12	
8388.96	He II	6.40	8388.41	−19.65	0.0120	0.0088	21	
8392.40	H I	P20	8391.78	−22.15	0.351	0.256	9	
8413.32	H I	P19	8412.70	−22.10	0.401	0.292	9	
8421.67	He II	6.37	8421.13	−19.23	0.0232	0.0169	15	
8433.85	[Cl III]	3F	8433.31	−19.20	0.0538	0.0391	11	
8437.96	H I	P18	8437.34	−22.03	0.464	0.337	9	
8446.25	O I	4	8445.67	−20.59	0.126	0.0915	10	
8446.36	O I	4	*	*	*	*	*	
8446.76	O I	4	*	*	*	*	*	
8448.39	He II	6.35	*	*	*	*	*	*i*
8463.70	He II	6.34	8463.18	−18.44	0.0186	0.0135	17	
8467.25	H I	P17	8466.44	−28.67	0.648	0.469	9	*i*
8480.67	He II	6.33	8480.07	−21.20	0.0547	0.0395	12	
8480.90	[Cl III]	3F	*	*	*	*	*	
8486.27	He I	6/16	8485.62	−22.94	0.0158	0.0114	18	
8499.00	He II	6.32	8499.01	0.34	0.0567	0.0409	11	
8499.70	[Cl III]	3F	*	*	*	*	*	
8502.48	H I	P16	8501.86	−21.87	0.655	0.473	9	
8519.40	He II	6.31	8518.74	−23.23	0.0241	0.0174	15	
8528.99	He I	6/15	8528.38	−21.46	0.0187	0.0135	17	
8661.40	He II	6.26	8660.88	−18.02	0.0560	0.0398	12	*i*
8662.90	C III	45	8664.37	50.85	1.287	0.913	9	
8663.90	C III	45	*	*	*	*	*	
8665.02	H I	P13	*	*	*	*	*	
8665.40	C III	45	*	*	*	*	*	*i*
8668.25	Ne II	$2G–2F_0$	8667.84	−14.19	0.0150	0.0107	19	
8680.37	Ne II	$2G–2F_0$	8679.95	−14.50	0.0119	0.0084	21	*i*
8701.30	He II	6.25	8700.79	−17.56	0.0487	0.0344	12	*i*
–	?	–	8703.81	–	0.0136	0.0096	20	
8706.60	C III	$2G–2H_0$	8706.19	−14.09	0.0062	0.0044	30	
8727.13	[C I]	3F	8726.47	−22.68	0.0563	0.0397	12	
8733.43	He I	6/12	8732.75	−23.33	0.0379	0.0267	13	
8736.04	He I	7/12	8735.39	−22.32	0.0124	0.0088	21	
8747.00	He II	6.24	8746.30	−24.00	0.0615	0.0433	12	
8750.47	H I	P12	8749.83	−21.92	1.543	1.086	9	
8776.60	He I	4/9	8776.23	−12.61	0.0901	0.0632	11	
8794.97	[Cr III]	18F	8794.38	−20.11	0.0156	0.0109	19	
8798.90	He II	6.23	8798.41	−16.70	0.0632	0.0443	12	
8806.76	Mg I	7	8806.03	−24.83	0.0079	0.0055	27	
8816.50	He I	10/12	8816.05	−15.31	0.0085	0.0059	25	

Table 2 – *continued*

λ_0 (Å)	Ion	Mult.	λ_{obs}	V_{rad} (km s^{-1})	$F(\lambda)/F(\mathrm{H}\,\beta)^a$	$I(\lambda)/I(\mathrm{H}\,\beta)^b$	Err(per cent)	Notes
8829.40	[S III]	3F	8829.05	−11.90	0.0131	0.0092	20	
8845.38	He I	6/11	8844.74	−21.68	0.0546	0.0381	12	
8848.05	He I	7/11	8847.45	−20.32	0.0203	0.0142	17	
8854.00	[Se III]	–	8853.48	−17.61	0.0111	0.0077	22	
8854.11	He I	5/11	*	*	*	*	*	
8857.40	C IV	9/13	8856.66	−25.06	0.0114	0.0080	22	
8859.10	He II	6.22	8858.53	−19.27	0.0633	0.0441	12	
8862.79	H I	P11	8862.13	−22.33	1.964	1.368	10	
8929.21	He II	6.21	8928.43	−26.20	0.0748	0.0518	11	
8996.99	He I	6/10	8996.26	−24.34	0.0668	0.0461	12	
8999.40	He I	7/10	8998.85	−18.35	0.0139	0.0095	20	
9014.91	H I	P10	9014.26	−21.63	2.630	1.810	10	*e*
9063.29	He I	4/8	9062.69	−19.83	0.0574	0.0394	12	*e*
9068.60	[S III]	1F	9068.17	−14.21	33.51	22.98	10	
9108.50	He II	6.19	9107.94	−18.42	0.0500	0.0342	13	*e*
9123.60	[Cl II]	1F	9122.83	−25.29	0.0724	0.0495	12	
9210.28	He I	6/9	9209.66	−20.19	0.0886	0.0604	11	
9213.20	He I	7/9	9212.44	−24.72	0.0274	0.0187	15	*e*
9225.23	He II	6.18	9224.51	−23.42	0.120	0.0817	11	*e*
9229.01	H I	P9	9228.31	−22.75	3.682	2.506	10	
9344.94	He II	5.8	9344.85	−2.91	0.162	0.110	11	*e*
9367.03	He II	6.17	9365.92	−35.54	0.0474	0.0322	13	*e*
9516.57	He I	4/7	9515.52	−33.11	0.0623	0.0422	12	*e*
9526.16	He I	6/8	9525.74	−13.22	0.114	0.0774	11	*e*
9530.60	[S III]	1F	9530.41	−5.96	78.52	53.09	10	
9542.06	He II	6.16	9541.67	−12.24	0.0844	0.0571	11	*e*
9545.97	H I	P8	9545.40	−17.88	2.652	1.793	10	*e*
9702.50	He I	3/7	9702.66	4.95	0.0061	0.0041	31	*e*
9708.20	C III	$3H_0$–3I	9707.69	−15.74	0.0097	0.0065	24	
9719.62	C III	3I–$3K_0$	9718.98	−19.73	0.0174	0.0117	18	*i*
9824.13	[C I]	–	9823.37	−23.19	0.132	0.0890	11	*i*
9850.26	[C I]	–	9849.26	−30.44	0.490	0.331	10	*i*
9902.30	[Kr III]	–	9902.88	17.56	0.218	0.147	11	
9903.46	C II	17.02	*	*	*	*	*	
9982.45	O II	$G[5]_0$–2[6]	9981.94	−15.31	0.0161	0.0109	19	
9988.54	O II	$G[5]_0$–2[6]	9989.58	31.21	0.0620	0.0419	12	
9990.08	O II	$D[3]_0$–0[4]	*	*	*	*	*	
9991.48	O II	$D[3]_0$–0[4]	*	*	*	*	*	
10 008.90	O II	$G[4]_0$–1[5]	10 008.18	−21.59	0.0122	0.0082	21	
10 027.70	He I	6/7	10 026.94	−22.72	0.237	0.160	10	*i*
10 031.20	He I	7/7	10 030.40	−23.90	0.0754	0.0510	12	
10 045.20	He II	6.14	10 044.47	−21.80	0.410	0.277	10	*i*
10 049.40	H I	P7	10 048.63	−22.99	9.655	6.525	10	
10 110.40	O II	$F[4]_0$–2[5]	10 109.92	−14.25	0.0115	0.0078	22	
10 123.60	He II	4.5	10 122.97	−18.65	25.33	17.12	10	*i*
10 138.40	He I	10/7	10 137.55	−25.15	0.0418	0.0282	13	
10 310.70	He I	4/6	10 310.09	−17.75	0.254	0.172	10	*i*
10 320.50	[S II]	3F	10 319.60	−26.16	0.911	0.616	10	
10 336.40	[S II]	3F	10 335.51	−25.83	0.688	0.465	10	
10 370.50	[S II]	3F	10 369.64	−24.87	0.328	0.222	10	
10 397.50	[N I]	3F	10 396.68	−23.65	0.526	0.356	10	*i*
10 407.40	[N I]	3F	10 406.33	−30.83	0.141	0.0954	11	
10 419.80	He II	6.13	10 418.64	−33.38	1.256	0.849	10	*i*

Notes. [a]Where F is the unreddened flux in units of $100.00 = 5.543 \times 10^{-12}$ erg cm^{-2} s^{-1}.
[b]Where I is the reddened corrected flux, with $c(\mathrm{H}\,\beta) = 0.27$, in units of $100.00 = 1.032 \times 10^{-11}$ erg cm^{-2} s^{-1}.
[c]Blended with an unknown line.
[d]Affected by charge transfer.
[e]Affected by atmospheric absorption bands.
[f]Affected by ghost.
[g]Partially blended with other emission line.
[h]Affected by interstellar Na I absorption.
[i]Affected by telluric emission.

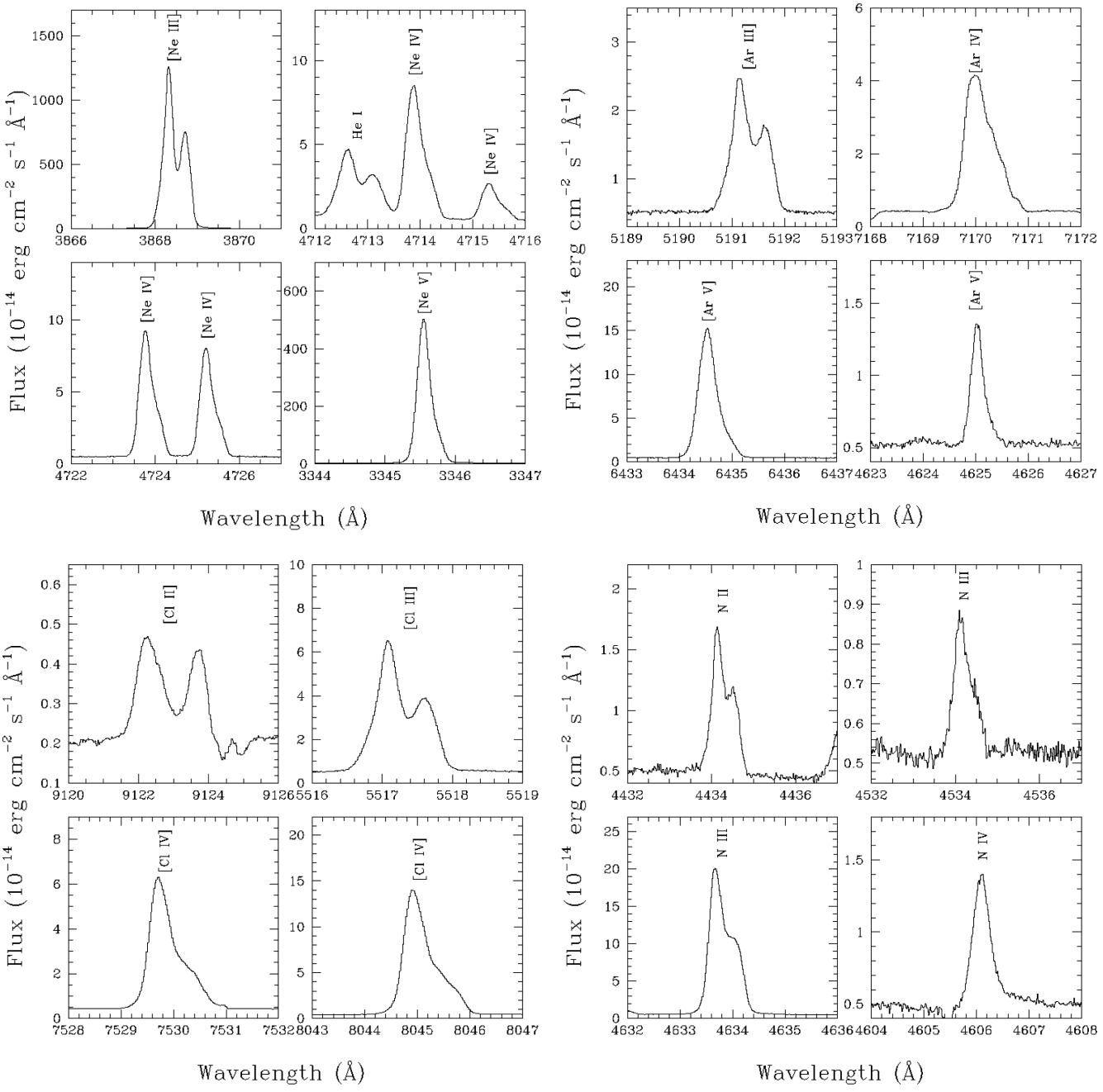

Figure 2. Portions of the echelle spectrum of NGC 3918 showing selected collisionally excited lines of different ionic species of Ne, Ar, and Cl, and recombination lines of N. The effect of the expansion velocity field is clearly shown. As expected, the effect is larger in the lowest ionization species whose lines are formed in the external parts of the PN, than in the highest ionization species, which form in the inner parts of the PN.

the deepest study of this object in the optical range. The use of other parametrizations of the standard extinction law would have no significant effects on the results of this paper, as the obtained $c(\mathrm{H}\,\beta)$ is fairly low (see below). The logarithmic redddening coefficient, $c(\mathrm{H}\,\beta)$, was derived by fitting the observed Balmer lines, $F(\mathrm{H\,I}\ \mathrm{Balmer})/F(\mathrm{H}\,\beta)$ (from H25 to H3), and the observed $F(\mathrm{H\,I}$ Paschen$)/F(\mathrm{H}\,\beta)$ lines (from P25 to P9) to the theoretical values computed by Storey & Hummer (1995) for $T_\mathrm{e} = 11\,000$ K and $n_\mathrm{e} = 5000$ cm^{-3}, as derived for NGC 3918 by Clegg et al. (1987). We only used those lines neither contaminated by telluric emission/absorptions nor by other nebular emissions. We obtained an averaged value of $c(\mathrm{H}\,\beta) = 0.26\pm0.06$. This value is lower than those obtained by Tsamis et al. (2003b), Clegg et al. (1987), and Peña & Torres-Peimbert (1985), which amount to 0.44, 0.43, and 0.40, respectively. However, our value is consistent with the value obtained by Clegg et al. (1987) from the Balmer decrement, which amounts to 0.33±0.14, and with the value obtained by Torres-Peimbert & Peimbert (1977) [$c(\mathrm{H}\,\beta) = 0.30$].

To determine the line flux uncertainties, we considered individually each spectral range (B1, B2, R1, and R2). Several lines were chosen in each of these ranges so as to cover the whole intensity ranges, and the statistical errors associated with the uncertainties in the continuum measurement were computed using the IRAF *splot* task. Error propagation and a logarithmic interpolation

Table 3. Unidentified lines and profile type.

λ_{obs}	Expected λ_0	Profile type[a]
3571.09	∼3571.3	Low
4554.64	∼4555.0	High
5150.60	∼5151.0	High
5450.62	∼5451.0	High
5464.91	∼5465.3	High
5467.17	∼5467.6	Low?
5468.35	∼5468.8	High
5487.87	∼5488.3	High
5659.80	∼5660.3	High
6114.12	∼6114.6	Low–high?
6272.78	∼6273.3	High
6958.81	∼6959.3	High
7030.44	∼7031.0	High
7046.36	∼7046.9	High
7058.79	∼7059.3	High
7102.30	∼7102.8	Low
7509.38	∼7509.9	Low
8703.81	∼8704.3	Low

Note. [a]'Low' means a double-peak line profile; 'high' means single-peaked or slightly double-peak line profile (see text).

of $F(\lambda)/F(\mathrm{H}\ \beta)$ *versus* $\sigma(F(\lambda)/F(\mathrm{H}\ \beta))$ were used to determine $\sigma(F(\lambda)/F(\mathrm{H}\ \beta))$ for each line. Finally, the final percentile errors (1σ) of the $I(\lambda)/I(\mathrm{H}\,\beta)$ ratios were computed taking into account the uncertainties in the determination of $c(\mathrm{H}\ \beta)$. The result is presented in column 8 of Table 2. Colons indicate errors higher than 40 per cent.

3.1 Unidentified lines.

There are 18 lines that could not be identified with the available sources, amounting to ∼2.5 per cent of the measured lines. There are also about 30 dubious identifications, labelled in Table 2 with a quotation mark. We checked that these lines are not telluric lines, nor ghosts or charge transfer features. Given the strong dependence of the line profiles (velocity field) with the excitation of the ion, we can at least tentatively classify these lines as low- or high-ionization ions, with low-ionization species having a clear double-peaked line profile and high-ionization lines a single-peaked or slightly double-peaked profile. In Table 3 we show the list of unidentified lines with a rough estimation of the laboratory wavelength and the profile type.

3.2 Identification of n-capture lines

The detection of n-capture element emission lines in the optical spectra of photoionized nebulae is a hard task, since these lines are intrinsically very faint. However, since the first identification of n-capture elements lines 20 yr ago by Péquignot & Baluteau (1994) in the optical spectrum of the PN NGC 7027, the reported detections of these lines in the optical spectra of Galactic PNe and H II regions have grown significantly (e.g. Baldwin et al. 2000; Liu et al. 2004a; Peimbert et al. 2004; Zhang et al. 2005; Sharpee et al. 2007; García-Rojas et al. 2009, 2012; Sterling et al. 2009; Otsuka et al. 2010, 2011; Fang & Liu 2011; Otsuka & Tajitsu 2013). Other studies have reported the detection of n-capture element lines in the NIR spectra of Galactic PNe and H II regions (e.g. Dinerstein 2001; Blum & McGregor 2008; Sterling & Dinerstein 2008) and in other galaxies (e.g. Vanzi et al. 2008).

Table 4. Corrected line ratios [$I(\mathrm{H}\ \beta) = 100$] for n-capture element lines in NGC 3918.

λ_0 (Å)	Ion	$I(\lambda)/I(\mathrm{H}\,\beta)$	Error(per cent)
5346.02	[Kr IV]	0.105	6
5363.37	[Rb V]	0.0045	38
5709.21	[Xe IV]	0.0065	27
5759.55	[Rb IV]	0.0047	:
5846.77	[Xe III]	0.0021	:
5867.74	[Kr IV]	0.131	15
6256.10	[Kr V]	0.0078	23
6408.80	[Xe VI]	0.0039	:
6826.70	[Kr III]	0.0284	12
7535.40	[Xe IV]	0.0076	23
8845.00	[Se III]	0.0058	:

We report the detection of several n-capture element lines in NGC 3918. In our analysis, we use all the certain and probable line identifications by Péquignot & Baluteau (1994) and Sharpee et al. (2007) as a reference. The complex velocity structure of NGC 3918 is a double-edged sword. On the one hand, it does not allow us to easily use automatic identification algorithms such as EMILI (Sharpee et al. 2003); on the other hand, it helps us to detect the presence of line blends with ions with different ionization potentials. Additionally, the large number of ghosts and charge-transfer features, as well as the 'wiggling' of the continuum which is typical of deep echelle spectra, do not allow us to properly use the PYSSN spectrum synthesis code, except in some cases (see below). The PYSSN code is a PYTHON version of the X-SSN code (Péquignot, Morisset & Casassus 2012) and is still in development. PYSSN uses a data base of emission lines containing identifications, wavelengths and relative intensities for lines of the same multiplets (or emitted by the same process as atmospheric emission and absorption lines). It generates a synthetic spectrum by summing the contributions of all the individual lines, taking into account different profiles for different ions and/or emission processes, and the continuous nebular emission. Reddening and instrumental response are also taken into account. Therefore, in most of the cases, we identify the lines by eye, following several criteria: (i) the line profiles agree with what is expected for the ionization potential of the ion; in some cases, this criterion allows us to discard possible blends with other faint lines; (ii) the radial velocities of different lines of the same ion agree; (iii) the relative intensities of lines arising from the same ion agree with what is expected from the collision strengths and spontaneous emission coefficient calculations for these transitions (this applies to the [Kr IV] and [Xe IV] lines); (iv) finally, in some cases of very tight blends we use the PYSSN spectrum synthesis code, which makes use of all the previous conditions to perform the line fitting. When the first three criteria are fulfilled we consider the identification to be robust. In Fig. 3 we show some of the n-capture element lines detected in our spectrum.

3.2.1 *Se-line identifications*

Several authors reported that the identification of the [Se III] λ8854.00 line is quite difficult because of blending with a weak He I λ8854.11 line which is at nearly the same wavelength (Péquignot & Baluteau 1994; Sharpee et al. 2007). We used the PYSSN spectral synthesis code to fit the nearby He I lines and estimate the contribution of the He I line to the blend. In Fig. 4 we show the best fit we have found. From this fit, a contribution of ∼75 per cent of the line was considered to come from the [Se III] emission. Another

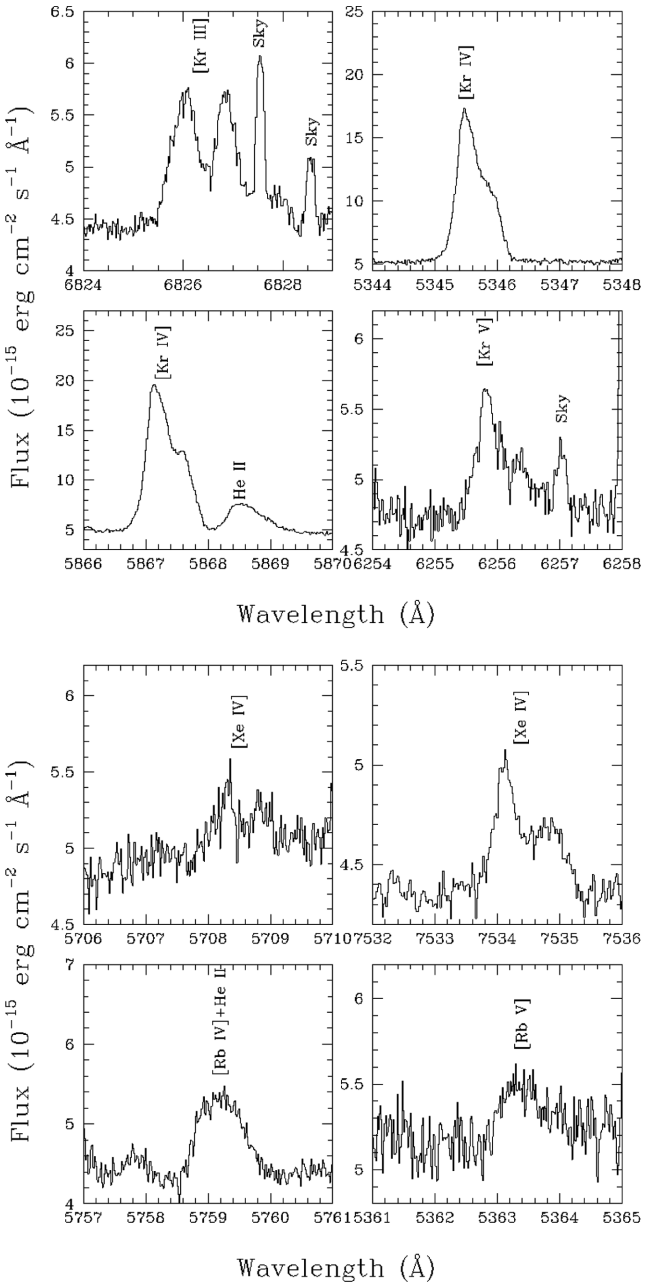

Figure 3. Portions of the echelle spectrum of NGC 3918 showing lines of different ionic species of Kr (upper panel), Xe, and Rb (lower panel).

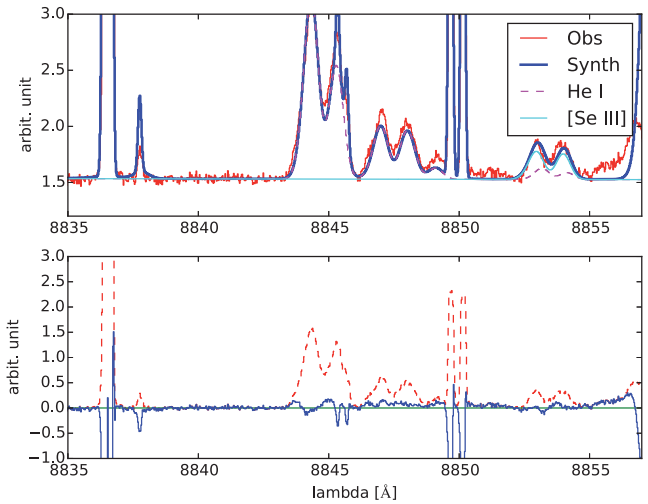

Figure 4. PYSSN fitting of the [Se III] λ8854.00 + He I λ8854.11 lines. In the upper panel we show the observed spectrum (red line) and the different fits (magenta dashed line for He I, cyan for [Se III], and blue for the total spectrum); flux is in arbitrary units. Note that a model of the telluric emission is included in the fit. In the lower panel, we show the residuals of the fit.

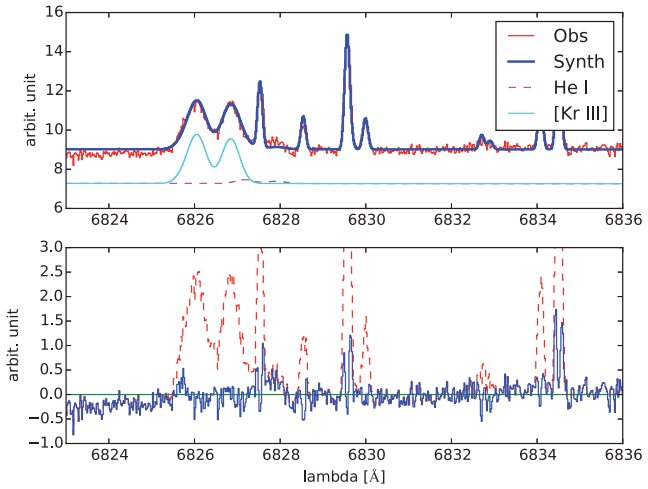

Figure 5. PYSSN fitting of the [Kr III] λ6826.70 + He I λ6827.88 lines. In the upper panel we show the observed spectrum (red line) and the different fits (magenta dashed line for He I, cyan for [Kr III], and blue for the total spectrum); flux is in arbitrary units. Note that a model of the telluric emission is included in the fit. In the lower panel, we show the residuals of the fit.

possible contaminant of this line is the [Mn III] λ8854.2 line, but we discarded this line because we do not detect any other [Mn III] line in the spectrum of NGC 3918.

3.2.2 Kr-line identifications

We identify lines of three ionization stages of Kr. Péquignot & Baluteau (1994) identify the [Kr III] λ6826.70 line as a strong feature, partially blended with the faint C I λ6828.12 and He I 3s ^{3}S–16p ^{3}P^0 λ6827.88 lines. Given the high ionization of NGC 3918, we discarded the presence of C I emission. We tentatively assume that the He I line is contributing to the measured flux of the line, given the radial velocity measured. We detect other 3s–*n*p transitions of He I in our spectrum, but several of them are strongly affected by telluric absorptions and/or emissions and their intensities are unreliable. Therefore, we used the spectrum synthesis code PYSSN to check how this line can affect the measured flux. In Fig. 5 we can see that the He I line is affecting the red end of the [Kr III] emission; PYSSN predicts that the He I line should have a flux ∼20 per cent the flux of the [Kr III] line, but, from a close inspection of Fig. 5 only a portion of the He I line (∼25 per cent) overlaps the [Kr III] line and therefore, the contribution to the measured flux is within the uncertainties reported for the [Kr III] line. Sharpee et al. (2007) report that this line could also be potentially affected by [Fe IV] λ6826.50. However, we do not detect other multiplet members that should be brighter than this line in our spectrum and therefore, this possibility was discarded. In Fig. 5 we see that the telluric nightglow OH lines only slightly affect the measured flux of the [Kr III] line and can be easily deblended. The [Kr III] λ9902.30 line, which arises

Table 5. Atomic data set used for collisionally excited lines.

Ion	Transition probabilities	Collisional strengths
N^+	Froese Fischer & Tachiev (2004)	Tayal (2011)
O^+	Froese Fischer & Tachiev (2004)	Kisielius et al. (2009)
O^{2+}	Froese Fischer & Tachiev (2004) Storey & Zeippen (2000)	Storey, Sochi & Badnell (2014)
Ne^{2+}	Galavís, Mendoza & Zeippen (1997)	McLaughlin & Bell (2000)
Ne^{3+}	Butler & Zeippen (1989) Bhatia & Kastner (1988)	Giles (1981)
Ne^{4+}	Galavís et al. (1997) Bhatia & Doschek (1993) Unknown	Dance et al. (2013)
Na^{3+}	Becker, Butler & Zeippen (1989) Bhatia & Kastner (1988)	Giles (1981)
S^+	Podobedova, Kelleher & Wiese (2009)	Tayal & Zatsarinny (2010)
S^{2+}	Podobedova et al. (2009)	Tayal & Gupta (1999)
Cl^+	Mendoza & Zeippen (1983)	Tayal (2004)
Cl^{2+}	Mendoza (1983)	Butler & Zeippen (1989)
Cl^{3+}	Kaufman & Sugar (1986) Mendoza & Zeippen (1982b) Ellis & Martinson (1984)	Galavís, Mendoza & Zeippen (1995)
Ar^{2+}	Mendoza (1983) Kaufman & Sugar (1986)	Galavís et al. (1995)
Ar^{3+}	Mendoza & Zeippen (1982a)	Ramsbottom & Bell (1997)
Ar^{4+}	Mendoza & Zeippen (1982b) Kaufman & Sugar (1986) LaJohn & Luke (1993)	Galavís et al. (1995)
K^{3+}	Kaufman & Sugar (1986) Mendoza (1983)	Galavís et al. (1995)
K^{4+}	Kaufman & Sugar (1986) Mendoza (1983)	Butler, Zeippen & Le Bourlot (1988)
Ca^{4+}	Kaufman & Sugar (1986) Mendoza (1983)	Galavís et al. (1995)
Fe^{2+}	Quinet (1996) Johansson et al. (2000)	Zhang (1996)
Fe^{3+}	Froese Fischer, Rubin & Rodríguez (2008)	Zhang & Pradhan (1997)
Fe^{4+}	Nahar et al. (2000)	Ballance, Griffin & McLaughlin (2007)
Fe^{5+}	Chen & Pradhan (2000)	Chen & Pradhan (1999)
Fe^{6+}	Witthoeft & Badnell (2008)	Witthoeft & Badnell (2008)
Se^{2+}	Biémont & Hansen (1986a)	Schoning (1997)
Kr^{2+}	Biémont & Hansen (1986a)	Schoning (1997)
Kr^{3+}	Biémont & Hansen (1986b)	Schoning (1997)
Kr^{4+}	Biémont & Hansen (1986b)	Schoning (1997)
Rb^{3+}	Biémont & Hansen (1986b)	Schoning (1997)[a]
Rb^{4+}	Biémont & Hansen (1986a)	Schoning (1997)[b]
Xe^{2+}	Biémont et al. (1995)	Schoening & Butler (1998)
Xe^{3+}	Biémont et al. (1995)	Schoening & Butler (1998)
Xe^{5+}	Biémont et al. (1995)	Schoening & Butler (1998)

Notes. [a]Scaled from Kr^{3+} effective collision strengths.
[b]Scaled from Kr^{4+} effective collision strengths.

from the same level as [Kr III] λ6826.70, is also expected in the spectrum. Indeed, a feature is found in our spectrum at the right wavelength, but the line is strongly blended with the C II multiplet 17.02 λ9903.46 line. If we estimate the flux of [Kr III] λ9902.30 by subtracting the flux of the C II λ9903.46 line, which yields a C^{2+} abundance consistent with what is obtained from the average of the other C II recombination lines (see Section 5.2.2), we still have a [Kr III] λ9902.30 line too bright compared to the [Kr III] λ6826.70 line (the theoretical line ratio [Kr III] λ9902.30/λ6826.70 computed from state-of-the-art atomic data shown in Table 5 is about 0.08). This discrepancy might be explained in terms of either the occurrence of other lines contributing to the measured flux, or errors in the assumed C II recombination coefficients. In either case, we cannot consider it as a robust identification and we then consider [Kr III] λ6826.70 as the only confirmed line of the [Kr III] spectrum.

The [Kr IV] λλ 5346.02 and 5867.74 nebular lines are usually the brightest n-capture lines in the optical spectra of PNe. As it can be seen in Fig. 3, this is the case in NGC 3918. In principle, these lines are well isolated and, at the excitation of NGC 3918, are not affected by blends. On the other hand, the [Kr IV] λ 6107.8 auroral line is extremely faint and it seems to be strongly blended with another line, which we identify as the brightest component of the N III 5p $^2P_0$–6d ^2D multiplet. The abundance computed from this line would be a factor of ∼4 larger than that derived from

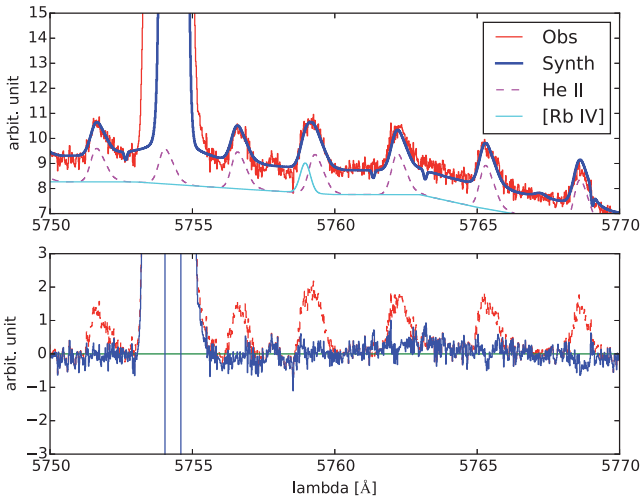

Figure 6. PYSSN fitting of the [Rb IV] λ5759.55 + He II λ5759.74 lines. In the upper panel we show the observed spectrum (red line) and the different fits (magenta dashed line for He II, cyan for [Rb IV], and blue for the total spectrum). Lower panel is similar to that shown in Fig. 5.

the nebular lines. The relative intensities of the [Kr IV] λλ 5346.02 and 5867.74 lines agree within 10 per cent with what is expected from their collision strengths. The excellent agreement between the observed and theoretical intensity ratios of the λλ 5346.02 and 5867.74 features strongly supports their identification with [Kr IV].

We identify the [Kr V] λ6256.1 line in our spectrum. Péquignot & Baluteau (1994) and Zhang et al. (2005) claim that this line can be affected by the C II λ6257.18 line and/or the dielectronic C II λ6256.52 line. Given our spectral resolution, the expected line profile and the radial velocities measured for other C II lines, we can discard the presence of the C II λ6257.18 line. Additionally, we discard the presence of the dielectronic C II λ6256.52 line because we do not detect the brightest component of the multiplet at 6250.76 Å. Unfortunately, we could not detect the [Kr V] λ8243.39 line to compare the expected theoretical intensity ratio with [Kr V] λ6256.1 line with the observed one because this line falls in a zone of the spectrum with a strong telluric absorption feature. Therefore, although the radial velocity is somewhat lower than expected, we consider the identification of the [Kr V] λ6256.1 line as quite robust.

3.2.3 *Rb-line identifications*

We identify two lines of Rb in the spectrum of NGC 3918. These identifications are complicated by blending with other features, especially the [Rb IV] λ5759.55 one. We reported the detection of this line as an excess intensity in the He II 5–47 λ5759.74 line. We have assumed He II $I(\lambda5759.55)/I(\mathrm{H}\ \beta) = 0.0082$ for $T_e = 12000$ K and $n_e = 1000$ cm^{-3} (Storey & Hummer 1995) to correct for the contribution of this line. This give us a contribution of ∼36.4 per cent of the [Rb IV] line to the total measured flux. Moreover, we used PYSSN to check this by fitting the expected profile of a He II line to this line, finding an excess of ∼35 per cent at the wavelength where we expect to find the [Rb IV] emission (see Fig. 6). Therefore, we consider that this is a quite robust identification. Unfortunately, we could not detect the [Rb IV] λ9008.74 line, which arises from the same upper level as λ5759.74 line and that could give us an additional constraint for [Rb IV] line identification, because it falls in a zone with a strong telluric absorption band.

Some authors report the identification of the [Rb V] λ5363.37 line in the spectra of PNe (Péquignot & Baluteau 1994; Sharpee et al. 2007). The most likely contaminants to this line would be the [Ni IV] λ5363.35 and O II 4f $F^2[4]^0_{7/2}$–4d′ $^2F_{7/2}$ λ5363.80 lines (Sharpee et al. 2007). We do not detect other [Ni IV] lines belonging to the same multiplet and, therefore, we discard this line as contributing to the measured flux. On the other hand, regarding the possible detection of the O II line, we inspected our spectra looking for other O II lines arising from the lower level of the O II λ5363.80 transition ($F^2[4]^0_{7/2}$) and tentatively detected a feature at ∼4609.15 Å, corresponding to the 3d $^2D_{5/2}$–4f $F^2[4]^0_{7/2}$ λ4609.4 transition, but its flux cannot be properly measured because it is strongly affected by a much brighter charge transfer feature. Other lines arising from the $F^2[4]^0_{7/2}$ level, such as O II λλ4282.02, 4312.11 or ending in this level, such as λλ5321.97, 5361.74, 5363.80, or 5375.57 were not detected in our spectrum. Additionally, the O II line profiles are different to the profile observed and, therefore, the [Rb V] λ5363.37 identification is tentatively adopted.

3.2.4 *Xe-line identifications*

Several Xe identifications are considered probable in the spectrum of NGC 3918. Péquignot & Baluteau (1994) identify [Xe III] λ5846.77 line as an excess intensity in the He II 5–31 λ5846.66 line in NGC 7027. Similarly, Sharpee et al. (2007) also detect this blend in objects in their sample. Following the same procedure of the [Rb IV] line identification and assuming the theoretical He II $I(\lambda5846.66)/I(\mathrm{H}\ \beta) = 0.0247$ ratio for $T_e = 12\,000$ K and $n_e = 1000$ cm^{-3} (Storey & Hummer 1995) to correct for the contribution of this line, we find a contribution of ∼8 per cent of the [Xe III] line to the total measured flux. As this is a rather uncertain estimation, and it lies within the uncertainties of the measured flux, we used the emission-line spectral synthesis code PYSSN to fit the expected profile of an He II line finding that, in principle, there is no substantial contribution of the [Xe III] line to the measured flux. Therefore, we cannot conclude that [Xe III] λ5846.77 is detected in our spectrum. Nevertheless, we do the exercise of computing an upper limit to the Xe^{2+} abundance adopting the flux excess measured in the He II line as the flux of the [Xe III] line.

We identify two possible [Xe IV] lines at λλ5709.10, 7535.4 Å. The [Xe IV] λ5709.21 is well separated from the widely observed N II multiplet 3 λ5710.77 line. Other potential contaminants, such as [Fe I] λ5708.91 and the intercombination Fe II] λ5709.04 line, can be discarded since no other lines of these ions are observed in the spectrum of NGC 3918 (a situation similar to what Sharpee et al. 2007 report for most of their objects). Sharpee et al. (2007) argue that all the lines most likely to affect the [Xe IV] λ7535.4 emission come from low-ionization ions (Fe II] λ7535.4, Ne II λ7534.75, [Cr II] λ7534.80, N II λ7535.10, and Ne I λ7535.77). Given the profile of the line we detect and the excitation of NGC 3918, we can safely discard all of them as possible contributors to the measured flux and, hence, we consider [Xe IV] λ7535.4 as a robust identification. The excellent agreement between the observed and theoretical intensities of the λλ 5709.10 and 7535.4 features strongly supports their identification with [Xe IV]. The intensity ratios of these lines agree within 17 per cent with what is expected from their collisional strengths and is consistent with the uncertainties of these lines.

We do not detect any [Xe V] line in our spectra. Sharpee et al. (2007) report the possible detection of the [Xe V] λ7076.8 line in the two most excited PNe of their sample. Although we do detect an emission feature at ∼7076.5 Å, the feature is strongly affected by

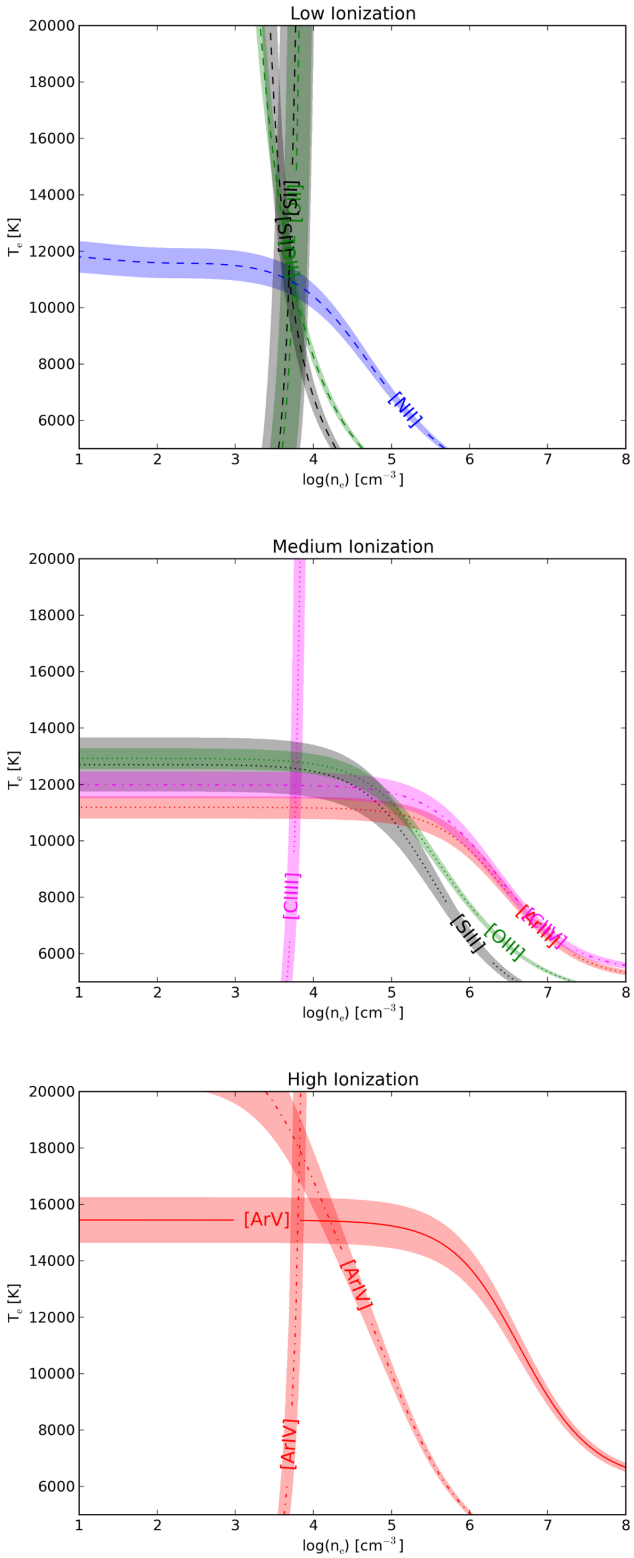

Figure 7. Diagnostic diagrams for the low- (upper panel), medium- (middle panel) and high- (lower panel) ionization zones in NGC 3918.

telluric absorptions, making its flux unreliable. On the other hand, we do not detect any line near 5228.8 Å or near 6998.7 Å, which correspond to the laboratory wavelengths of the [Xe V] $^3P_{1,2}$–$^1D_2$ transitions. In the first case, no emission was detected and in the second case, telluric absorption lines preclude the identification of any emission line.

Péquignot & Baluteau (1994) and Sharpee et al. (2007) report the detection of [Xe VI] λ6408.89 line in the spectrum of NGC 7027 on the red wing of the He II 5–15 λ6406.38 line. We also detect two extremely faint features at a similar position. We discard the identification of these lines in terms of a double-peaked line of [Fe III] λ6408.50, owing to the low number of [Fe III] identifications in our spectrum and to the different line profile of [Fe III] lines. Alternative identifications could be the C IV λλ6408.1, 6408.8 lines. Sharpee et al. (2007) discard these identifications owing to the high excitation of these lines, although they report the detection of other C IV lines in the spectrum of NGC 7027. Since we detect other brighter lines of the 9g–*n*h series, we confirm the identification of the C IV 9g ^{2}G–17h $^2H_0$ λ6408.1. However, the second line can hardly be C IV 9h $^2H_0$–17i ^{2}I λ6408.8, since there are no other lines of the 9h–*n*i series in our spectra. The identification of this line as [Xe VI] λ6408.90 is also highly questionable, given the faintness of the line; however, when we compute the Xe^{5+} abundance from this line, we find a reasonable result (see Section 5.1).

Since the intensities of several n-capture element lines are corrected by deblending other nebular or telluric lines, in Table 4 we show the detected n-capture element lines with line intensities corrected for contamination from other features. In the following, we comment on identifications of individual n-capture elements.

Table 6. Atomic data set used for recombination lines.

Ion	Recombination coefficients
H^+	Storey & Hummer (1995)
He^+	Porter et al. (2012, 2013)
He^{2+}	Storey & Hummer (1995)
C^{2+}	Davey, Storey & Kisielius (2000)
N^{2+}	Fang, Storey & Liu (2011, 2013)
	Escalante & Victor (1992)
	Kisielius & Storey (2002)
O^{2+}	Storey (1994)
	Liu et al. (1995)
CNO^{3+}	Péquignot, Petitjean & Boisson (1991)
	Nussbaumer & Storey (1984)
CO^{4+}	Péquignot et al. (1991)
N^{4+}	Péquignot et al. (1991)
	Nussbaumer & Storey (1984)
Ne^{2+}	Kisielius et al. (1998)
	Kisielius & Storey (private communication)

4 PHYSICAL CONDITIONS

The large number of emission lines identified and measured in the spectrum of NGC 3918 allows us to derive physical conditions using multiple emission-line ratios. The computations of physical conditions were carried out with PYNEB v1.0.9 (Luridiana, Morisset & Shaw 2015), a PYTHON-based package dedicated to the analysis of emission-line spectra. The methodology followed for the derivation of the electron density, n_e, and the electron temperature, T_e, has been described in previous papers of our group. We have updated the atomic data set to state-of-the-art atomic data, presented in Tables 5 and 6 for collisionally excited lines (CELs) and optical recombination lines (ORLs), respectively. Errors in the diagnostics were computed via Monte Carlo simulations. We generate 1500 random values for each line intensity using a Gaussian distribution centred in the observed line intensity with a sigma equal to the

Table 7. Physical conditions.

Diagnostic	
n_e (cm^{-3})	
[S II] λ6716/λ6731	5000^{+3000}_{-2100}
[O II] λ3726/λ3729	5600^{+2700}_{-1800}
[Cl III] λ5517/λ5537	6000^{+1100}_{-1000}
[Ar IV] λ4711/λ4741	6500^{+1300}_{-1200}
Adopted	**6200±1250**
T_e (K)	
[N II] λ5755/λ6548	10950±700
[O II] λλ3726+29/λλ7320+30	11 350±2800
[S II] λλ4068+76/λλ6716+31	10 650±1800
T_e(low) (adopted)	**11 000±1350**
[O III] λ4363/λ4959	12 800±400
[S III] λ6312/λ9069	12 550±950
[Ar III] λ5192/λ7136	11 200±400
[Cl IV] λ5323/λλ7531+8046	11 950±450
T_e(mid) (adopted)	**12 100±300**
[Ar IV] λλ7170+263/λλ4711+40	17 900±1250
[Ar V] λ4626/λλ6425+7005	15 400±800
T_e(high) (adopted)	**15 400±800**
T_e(BJ)	**11 750±1400**

associated uncertainty. For higher number of Monte Carlo simulations, the errors in the computed quantities remain constant. The electron temperatures and densities are presented in Table 7.

For the calculation of ionic abundances (see Section 5) we assumed a three-zone ionization scheme. For n_e, we obtained very similar results from the different diagnostics; therefore, we adopted the average of n_e([O II]), n_e([S II]), n_e([Cl III]) and n_e([Ar IV]) as representative of the whole nebula. We adopted the average of electron temperatures obtained from [N II], [S II] and [O II] lines as representative of the low-ionization zone (IP < 17 eV); we refer to this value as T_e(low). Similarly, the average of electron temperatures obtained from [O III], [Ar III], [S III] and [Cl IV] lines was assumed as representative of the medium-ionization zone (17 eV < IP < 39 eV) and designated T_e(mid). Finally, the electron temperature from [Ar V] (see below) was adopted as representative of the high-ionization zone (IP > 39 eV) and designated T_e(high) (see Table 7).

Following equations 1 and 2 by Liu et al. (2000), we corrected the intensity of the auroral [N II] λ5755 line and the trans-auroral [O II] λλ7320+30 lines from the recombination contribution. We assumed preliminary computations of the N^{++}/H^+ and O^{++}/H^+ ratios obtained from N II multiplets 3, 39, and 48 and from the O II multiplet 1 to compute the recombination contributions to [N II] λ5755 line and [O II] λλ7320+30 lines, respectively. These contributions led to an ∼6 per cent correction in the [N II] line and in the [O II] lines, which translate in temperatures lower by ∼300 K in both temperature diagnostics. Additionally, we also corrected the contribution of the He II 5–49 λ5754.67 line [I(He II 5.49)/I(H β)∼0.0078]. Given the high-ionization degree of NGC 3918, the recombination contribution to the auroral λ4363 line may also be non-negligible; we estimated it using equation 3 of Liu et al. (2000), where the O^{3+}/H^+ ratio was estimated assuming $O^{3+}/H^+ = (He/He^+)^{2/3} \times (O^+/H^+ + O^{++}/H^+)$. Using the values derived for He^+/H^+ and He^{++}/H^+ from ORLs (see Table 9) and O^+/H^+ and O^{++}/H^+ from CELs (see Table 7), this contribution amounts to ∼1 per cent, which has almost no effect on the determination of T_e([O III]) and therefore, was not considered.

In Fig. 7 we show the diagnostics diagrams obtained for each ionization zone in NGC 3918. It is worth noting the agreement between the different diagnostics except for the high-ionization zone, where [Ar IV] temperature diagnostic gives a very high T_e. We discarded T_e([Ar IV]) because we notice in a previous paper (see section 4.3 of García-Rojas et al. 2013) that the ratio between collisional strengths for [Ar IV] λλ7170+263 and λλ4711+40 lines might be unreliable. Therefore, only the [Ar V] diagnostic was considered for the high-ionization zone.

The electron temperature can also be derived from the ratio between the Balmer discontinuity and the H I lines belonging to the Balmer series. We use the expression given by Liu et al. (2001) to compute the electron temperature T_e(BJ) from the ratio of the Balmer discontinuity to I(H11).

The physical conditions reported in Table 7 agree within the uncertainties with the physical conditions reported by Clegg et al. (1987) and Tsamis et al. (2003b).

5 CHEMICAL ABUNDANCES

5.1 Ionic abundances from CELs

Ionic abundances from CELs were computed using PYNEB (Luridiana et al. 2015) and the atomic data in Table 5. To perform the computations required for this paper, we updated PYNEB by including several new ions; the updated version of PYNEB (v1.0.9) was uploaded to the PYNEB website.[3] For highly ionized Fe ions, we adopt the data recommended by Delgado-Inglada & Rodríguez (2014), and for n-capture elements we use the atomic data references compiled by Sharpee et al. (2007). Errors in the line fluxes and the physical conditions were propagated via Monte Carlo simulations. As pointed out in Section 4, we use a three-zone scheme of the nebula, adopting a unique n_e value in the three zones and T_e(low) for ions with IP<17 eV (i.e. N^+, O^+, S^+, and Fe^{2+}), T_e(mid) for ions with 17 eV < IP < 39 eV (i.e. O^{2+}, S^{2+}, Cl^{2+}, Cl^{3+}, Ar^{2+}, Fe^{3+}, Se^{2+}, Kr^{2+}, Kr^{3+}, Xe^{2+}, and Xe^{3+}), and T_e(high) for ions with IP > 39 eV (i.e. Ne^{2+}, Ne^{3+}, Ne^{4+}, Na^{3+}, Ar^{3+}, Ar^{4+}, K^{3+}, K^{4+}, Ca^{4+}, Fe^{4+}, Fe^{5+}, Fe^{6+}, Kr^{4+}, Rb^{3+}, Rb^{4+}, and Xe^{5+}). Ionic abundances are presented in Table 8, along with the lines used to compute them. We avoid using auroral lines in abundance computations because they do not affect significantly the computed abundances but can introduce some scatter.

Since transition probabilities and effective collision strengths for several of the detected Fe-peak species ([Cr II], [Cr III], [Mn IV], [Mn V], [Co IV], [Ni V], [Cu V], and [Cu VI]) are unknown, we are unable to determine the ionic or elemental abundances of these species. Most of these ions require large model atoms (30–50 levels), as used for Fe ions (e.g. Rodríguez & Rubin 2005; Delgado-Inglada & Rodríguez 2014) in order to accurately determine the fractional populations of the upper levels of the observed transitions. Gas-phase abundances of these species would provide valuable information regarding the chemical content of dust grains in PNe and AGB star winds. New atomic data determinations are needed to make such investigations possible.

5.2 Ionic abundances from recombination lines

In the following subsections, we present ionic abundances for He, C, N, O, and Ne derived from ORLs. We adopt the physical conditions derived from CELs to compute the abundances, as ORLs

[3] http://www.iac.es/proyecto/PyNeb/

Table 8. CELs ionic abundances.

Ion	Lines used	$12 + \log(X^{i+}/H^+)^a$
N^+	[N II] λλ6548+84	$7.12^{+0.16}_{-0.10}$
O^+	[O II] λλ3726+29	$7.58^{+0.29}_{-0.17}$
O^{2+}	[O III] λλ4959, 5007	8.47±0.04
Ne^{2+}	[Ne III] λλ3868, 3967	7.80±0.04
Ne^{3+}	[Ne IV] λλ4714+15, 4724+25	7.50±0.15
Ne^{4+}	[Ne V] λλ3345, 3425	7.20±0.08
Na^{3+}	[Na IV] λλ3242, 3362	5.53±0.08
S^+	[S II] λλ6717+31	$5.57^{+0.20}_{-0.12}$
S^{2+}	[S III] λλ8829, 9069	6.45±0.07
Cl^+	[Cl II] λ 9123	3.89±0.11
Cl^{2+}	[Cl III] λλ3353, 5517+37, 8434	4.84±0.05
Cl^{3+}	[Cl IV] λλ7531, 8045	4.87±0.04
Ar^{2+}	[Ar III] λλ3109, 7136, 7751	6.10±0.04
Ar^{3+}	[Ar IV] λλ4711+40	6.10±0.04
Ar^{4+}	[Ar V] λλ6435, 7005	5.21±0.06
K^{3+}	[K IV] λλ6102, 6796	4.14±0.06
K^{4+}	[K V] λλ4123+63	4.10±0.07
Ca^{4+}	[Ca V] λ5309	3.76±0.06
Fe^{2+}	[Fe III] λλ4701+55, 4881, 5270	$4.01^{+0.18}_{-0.14}$
Fe^{3+}	[Fe IV] λ6740	4.35:
Fe^{4+}	[Fe V] λλ3891+95, 4181, 4227	4.38±0.07
Fe^{5+}	[Fe VI] λλ5278, 5335+70, 5424+27+85, 5631+77	4.25±0.06
Fe^{6+}	[Fe VII] λλ5158, 5276, 5720. 6086	4.14±0.06
Se^{2+}	[Se III] λ8854	$2.79^{+0.15}_{-0.23}$
Kr^{2+}	[Kr III] λ6827	3.23±0.06
Kr^{3+}	[Kr IV] λλ5346, 5868	3.62±0.05
Kr^{4+}	[Kr V] λ6256	2.60±0.11
Rb^{3+}	[Rb IV] λ5760	2.41:
Rb^{4+}	[Rb V] λ5364	$1.83^{+0.17}_{-0.28}$
Xe^{2+}	[Xe III] λ5847	<1.47
Xe^{3+}	[Xe IV] λλ5709, 7535	2.41±0.08
Xe^{5+}	[Xe VI] λ6409	1.37:

Note. [a]Only lines with intensity uncertainties lower than 40 per cent have been considered, except in the case of Fe^{3+} and n-capture lines, where we used all the available lines (see text).

depend only weakly on electron temperature and are essentially independent on the electron density under the low-density conditions of NGC 3918.

5.2.1 *He^+ and He^{++} abundances*

We detect several He I emission lines in the spectrum of NGC 3918. These lines arise mainly from recombination, but some of them can be affected by collisional excitation and self-absorption effects. We use the effective recombination coefficients compiled in Table 6 for H I and He I. Both collisional contribution effects and the optical depth in the triplet lines are included in the computations. Using PYNEB, we determine the He^+/H^+ ratio from the three brightest He I emission lines: λλ4471, 5876, and 6678.

We measure multiple He II emission lines in the spectrum of NGC 3918, but, to compute the He^{2+}/H^+ ratio, we use only the 11 brightest ones among those not affected by telluric features or line blending (λλ3203, 4100, 4200, 4339, 4542, 4686, 4859, 5412, 6560, 7593, and 8237 Å). The computation adopts the recombination coefficients computed by Storey & Hummer (1995). The adopted He^+/H^+ and He^{2+}/H^+ ratios are presented in Table 9.

Table 9. He^+ and He^{2+} abundances.

Ion	$12+\log(He^{i+}/H^+)$
He^+/H^+	10.77 ± 0.02
He^{2+}/H^+	10.63 ± 0.01

5.2.2 *Ionic abundances from C, N, O, and Ne recombination lines*

A well-known problem of nebular astrophysics is the difference between the chemical composition of photoionized plasmas as derived from CELs and from recombination lines (ORLs). This discrepancy is parametrized in terms of an abundance discrepancy factor (ADF), which is defined as

$$\mathrm{ADF}(X^{i+}) = (X^{i+}/H^+)_{\mathrm{ORLs}}/(X^{i+}/H^+)_{\mathrm{CELs}}, \quad (1)$$

where X^{i+}/H^+ is the abundance of *i*-times ionized element *X* relative to H^+. ADFs may reach values of 2–3 in H II regions (García-Rojas & Esteban 2007) and up to 120 in PNe, with an average value of about 3 (McNabb et al. 2013; Corradi et al. 2015).

Thanks to the high quality of our data, we could measure a large number of permitted lines of heavy-element ions such as O I, O II, O III, O IV, C II, C III, C IV, N II, N III, N IV, Ne II, Si II, Si III, Mg I, and

Table 10. Ionic abundance ratios from permitted lines of C in NGC 3918[a].

Mult.	λ_0	$I(\lambda)/I(\mathrm{H}\,\beta)$ ($\times10^{-2}$)	C^{i+}/H^+ ($\times10^{-5}$)
		C^{2+}/H^+	
6	4267.15	0.473±0.024	**45**
16.04	6151.43	0.021±0.003	**47**
17.02	9903.46[b]	0.147±0.016	58
17.04	6461.95	0.049±0.004	**46**
17.06	5342.38	0.025±0.003	**45**
	Adopted		**45±2**
		C^{3+}/H^+	
1	4647.42[c]	0.235±0.012	**19**
16	4067.94[d]	0.113:	20
	4068.91[d]	0.148:	20
	4070.26[d]	0.193:	20
	Sum		**20**
18	4186.90	0.169±0.010	**21**
	Adopted		**20±2**
		C^{4+}/H^+	
8	4657.55	0.330±0.023	12
	4658.20	*	*
8.01	7726.20	0.152±0.014	15
	Adopted		**13±2**

Notes. [a]Only lines with intensity uncertainties lower than 40 per cent have been considered (see text).
[b]Blend with [Kr III] λ9902.3 line.
[c]Blend with unknown line.
[d]Corrected from the contribution of [S II] λ4068.6 line and O II λλ4069.62+.89 lines.

Table 11. Ionic abundance ratios from permitted lines of N in NGC 3918.[a]

Mult.	λ_0	$I(\lambda)/I(\mathrm{H}\,\beta)$ ($\times10^{-2}$)	N^{i+}/H^+ ($\times10^{-5}$)
		N^{2+}/H^{+b}	
3	5666.64	0.019±0.002	10
	5676.02	0.008±0.002	8
	5679.56	0.041±0.003	12
	5710.76	0.007±0.002	10
	Sum		**10**
12	3994.98	0.008±0.003	8
39	4041.31	0.021±0.003	16
48	4239.40	0.079±0.006[c]	30
	Adopted		**10±1**
		N^{3+}/H^+	
18	4379.11[d]	<0.160	<7
	Adopted		**<7**
		N^{4+}/H^+	
$3s^3S–3p^3P_0$	3483.00	0.033±0.013	1.6
$5g^{1,3}G–6h^3H_0$	4606.33	0.076±0.005	1.9
$6g^{1,3}G–7h^{1,3}H_0$	7581.90	0.083±0.019	1.2
$6h^{1,3}H_0–7i^{1,3}I$	7702.96	0.025±0.003	1.9
	Adopted		**1.8±0.5**

Notes. [a]Only lines with intensity uncertainties lower than 40 per cent have been considered (see text).
[b]For multiplets 3 and 39, recombination coefficients by Fang et al. (2011, 2013). For multiplet 12 recombination coefficients by Kisielius & Storey (2002). For multiplet 48, recombination coefficients by Escalante & Victor (1992).
[c]The reported flux ratio is the sum of the contribution of three individual lines at λλ4236.91, 4237.05, and 4241.78 Å.
[d]Blended with O III λ4379.6 Å.

Mg II, many of them detected for the first time in NGC 3918, and compute the ADF for several ions. Unfortunately, many of these permitted lines are affected by fluorescence or blended with telluric emission lines, making their measured intensities unreliable. A discussion on the mechanisms of formation of permitted lines can be found in Esteban et al. (1998, 2004, and references therein). We could not estimate the Mg^{2+}/H^+ ratio because the pure recombination line of Mg II λ4481 is affected by charge transfer in the CCD and its flux is unreliable.

The abundances are derived using the atomic data compiled in Table 6. For C^{3+}, N^{3+}, N^{4+}, and O^{3+} we take also into account the contribution of dielectronic recombination computed by Nussbaumer & Storey (1984). We selected the lines formed by pure recombination to compute ionic abundances from ORLs in PNe (see Liu et al. 2000; Tsamis et al. 2004). For C IV, N III, and N IV lines and some multiplets of O III and O IV, we adopt the log(*gf*)s given by the computations in the Atomic Line List v2.05b18.[4] The log(*gf*) values necessary to compute abundances from the remaining lines for which we have assumed LS-coupling have been adopted from the local thermodynamic equilibrium (LTE) computation predictions from Wiese, Fuhr & Deters (1996).

C ORLs: owing to the high ionization of NGC 3918, we detect lines of C II, C III, and C IV that are excited by pure recombination and therefore are suitable for abundance determinations (see García-Rojas et al. 2009, and references therein). In Table 10 we show the ionic abundances from recombination lines of C. The results obtained for the different multiplets of each given ion clearly show the excellent agreement between the different lines, strengthening the hypothesis of the recombination origin of these lines. Tsamis et al. (2004) computed the ADF for C^{2+} and C^{3+} by comparing the abundances obtained from C II and C III ORLs with the abundances obtained from *IUE* UV data of the C III] λλ1906+09 CELs and the C IV λ1549 resonant doublet, respectively. Our ORL C^{2+} abundances are in good agreement with those obtained by Tsamis et al. (2004) but, on the other hand, we obtain C^{3+} and C^{4+} abundances that are somewhat higher than those obtained by Tsamis et al. (2004). In our case the comparison between UV CELs and optical ORLs is meaningless because optical and *IUE* UV observations do not cover the same volume of NGC 3918.

N ORLs: several permitted lines of N II, N III, and N IV are detected in our spectrum. In Table 11 we show the ionic abundances from recombination lines of N. We compute the N^{2+}/H^+ ratios from N II permitted lines of multiplets 3, 12, 39, and 48, which are mainly excited by recombination and are not sensitive to optical depth effects (Liu et al. 2004b). We assume the recombination coefficients by Fang et al. (2011, 2013) except in the case of multiplets 12 and 48, for which Fang et al. (2011, 2013) do not compute recombination coefficients and, therefore, we adopt the recombination coefficients by Kisielius & Storey (2002) for multiplet 12 and Escalante & Victor (1992) for multiplet 48.

Lines belonging to multiplets 1 and 2 are the brightest N III lines detected in our spectrum, but they are not reliable for abundance determinations because they appear to be excited by the Bowen mechanism (Grandi 1976). However, other N III lines are detected in our spectrum but the recombination coefficients are only available for the multiplet 18 N III λ4379.11 line (see Péquignot et al. 1991).

[4] Webpage at http://www.pa.uky.edu/~peter/newpage/.

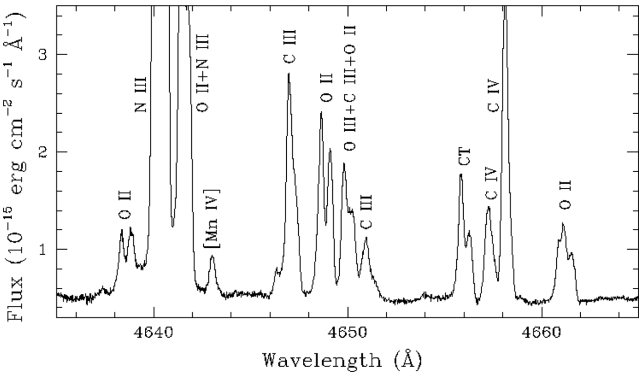

Figure 8. Portion of the echelle spectrum of NGC 3918 showing the zone where the O II multiplet 1 ORLs lie. Given the high ionization of NGC 3918, we also detected several permitted lines of C III, C IV, N III, and O III lines, although only some of them are excited by recombination (see text). At ∼4656 Å there is a feature produced by charge transfer (CT) in the CCD.

This is a 4f–5g transition that cannot be excited by mechanisms other than recombination. Unfortunately, this line is probably blended with the O III λ4379.6 Å line; as the relative strength of this O III line with other detected lines belonging to the same multiplet is not available, we can only give an upper limit to the N^{3+}/H^{+} ratio.

We detect several N IV in the spectrum of NGC 3918, but only a handful of them have available recombination coefficients (Péquignot et al. 1991). These lines give relatively similar results for the N^{4+}/H^{+} ratio and most of them are transitions between high levels and, therefore, are probably excited by pure recombination. The 3s–3p transition gives very similar results to the other lines and, therefore, recombination is its most probable excitation mechanism. Similarly to the case of C ions, although there are *IUE* UV CELs data available for N^{3+} and N^{4+} ions for NGC 3918, a comparison with our ORL abundances would not be meaningful since optical and UV observations do not cover the same volume of the nebula.

O ORLs: we detect a large number of O II permitted lines in our spectrum. Esteban et al. (2004) argue that the best lines to compute O^{2+} abundances from ORLs are those belonging to multiplets 1, 2, 10, 20, and from the 3d–4f transitions, which are mainly excited by recombination. However, we detect other multiplets that, at the excitation of NGC 3918, are not expected to be affected by any fluorescence effects. In Fig. 8 we show the region of the multiplet 1 O II ORLs, which are the brightest O II ORLs in the spectrum of NGC 3918 [of the order $10^{-3} \times I(\mathrm{H}\,\beta)$]. The upper levels of the transitions of this multiplet may be affected by departures from LTE for densities $n_e < 10^4$ cm^{-3} (Ruiz et al. 2003; Tsamis et al. 2003a). In such a case, the abundances derived from the various lines assuming LTE may differ from each other by large factors. To account for such effect, we apply the non-LTE corrections estimated by Peimbert, Peimbert & Ruiz (2005), obtaining abundances from individual lines in good agreement; we also derive the abundance using the sum of all lines of the multiplet following the recipe given by Esteban et al. (1998). This abundance, which is not affected by non-LTE effects, agrees with those derived from individual lines. In Table 12 we present the values obtained for the individual lines, as well as those derived from the sum of all the lines of a given multiplet. We only consider lines with errors lower than 40 per cent; for 3d–4f transitions, when available, we average lines with errors <40 per cent, otherwise, we average all available lines and quote the final value with an uncertainty higher than 40 per cent.

Table 12. Ionic abundance ratios from permitted lines of O in NGC 3918.[a]

Mult.	λ_0	$I(\lambda)/I(\mathrm{H}\,\beta)$ ($\times10^{-2}$)	O^{i+}/H^{+} ($\times10^{-5}$)
		O^{2+}/H^{+}	
1[b]	4638.85	0.114±0.010	66
	4641.81	0.109±0.030	42
	4649.14	0.219±0.037	65
	4650.84	0.031:	17:
	4661.64	0.114±0.027	59
	4676.24	0.051±0.024	55
	Sum		**52**
2	4317.14	0.019±0.003	27
	4319.63	0.016±0.003	22
	4336.83	0.011±0.003	36
	4345.56	0.022±0.003	28
	4349.43	0.053±0.005	26
	Sum		27
5	4416.97	0.029±0.004	**51**
10[c]	4069.62	0.135:	53:
	4069.89	*	*
	4072.15	0.133:	55:
	4075.86	0.184:	53:
	4078.84	0.021±0.003	57
	4092.93	0.018±0.003	51
	Sum		**53**
12[c]	3882.19	0.021±0.003	61
19[c]	4132.80	0.015±0.003	28
	4153.30	0.026±0.003	33
	Sum		31
20[c]	4110.79	0.007±0.002	30
	4119.22	0.053±0.005	61
	Sum		**57**
3d–4f[c]	4087.15	0.015±0.003	51
	4095.64	0.007±0.002	32
	4275.55	0.036±0.004	60
	4285.69	0.011±0.003	50
	4288.82	0.005:	87:
	4291.25	0.010±0.003	55
	4303.61	0.004±0.001	60
	4303.82	0.028±0.003	60
	4602.13	0.008±0.002	44
	4613.68	0.003:	70:
	Average		**46**
	Adopted		**52±7**
		O^{3+}/H^{+}	
8	3260.86	0.286±0.026	18
	3265.33	0.310±0.028	13
	3284.45	0.024:	12
	Sum		**15**
	Adopted		**15±2**
		O^{4+}/H^{+}	
$5g^2G$–$6h^2H_0$	4631.89	0.153±0.009	**5**
20	7677.40	0.024±0.003	**5**
	Adopted		**5±1**

Notes. [a]Only lines with intensity uncertainties lower than 40 per cent have been considered (see text).
[b]Corrected from non-LTE effects (see text).
[c]Recombination coefficients in intermediate coupling (Liu et al. 1995).

For 3s–3p transitions we use the recombination coefficients assuming LS-coupling by Storey (1994). In all the other cases (3p–3d and 3d–4f transitions) we use the intermediate-coupling scheme by Liu et al. (1995).

Table 13. Ionic abundance ratios from permitted lines of Ne in NGC 3918[a].

Mult.	λ_0	$I(\lambda)/I(\mathrm{H}\,\beta)$ ($\times10^{-2}$)	Ne^{i+}/H^+ ($\times10^{-5}$)
		Ne^{2+}/H^+	
1	3694.22	0.060±0.013	16
	3709.62	0.034±0.013	25
	3766.26	0.017±0.005	16
	3777.14	0.015:	15:
	Sum		**18**
7	3323.74	0.031:	8:
39	3829.77	0.013±0.003	**11**
55	4409.30	0.017±0.003	**25**
57	4428.54	0.011±0.003	**25**
	Adopted		**16±2**

Note. [a]Only lines with intensity uncertainties lower than 40 per cent have been considered (see text).

As seen in Table 12, the abundances computed from multiplets 1, 5, 10, 20, and 3d–4f transitions (averaged value) agree within a ∼15 per cent uncertainty. However, multiplets 2 and 19 give abundances that are a factor of ∼1.7–2 lower and multiplet 12 give an abundance that is ∼10 per cent higher than the abundances derived from the other lines. Liu et al. (2000) report a similar behaviour for multiplet 2 and claim that departure from case B to case A could resolve this discrepancy. However, considering case A we obtain abundances that are a factor of ∼1.4 higher but still too low compared to the other multiplets. Taking into account that multiplet 1 is the most widely used proxy of the O^{2+}/H^+ ratio from ORLs and that the derived abundance from this multiplet agrees with the one derived from multiplets 5, 10, 20, and 3d − 4f transitions, we finally adopt the average abundance weighted by the uncertainties of multiplets 1, 5, 10, 20, and 3d − 4f lines as representative of the O^{++} abundance from ORLs. From this value, we compute an $ADF(O^{2+}) = 1.8\pm0.3$, which is in good agreement with the value obtained by Tsamis et al. (2004) for NGC 3918 for their comparison between optical CELs and ORLs [$ADF(O^{2+}) = 1.85$].

We detect several lines of O III in the spectrum of NGC 3918. We do not consider the brightest O III lines (i.e. those belonging to multiplets 2 and 5) because they are probably excited by other mechanisms than recombination (see Grandi 1976; Clegg & Walsh 1985). We compute the O^{3+}/H^+ ratio from ORLs from multiplet 8 of O III, which has contributions from both radiative and dielectronic recombination (Liu & Danziger 1993).

Several O IV lines are detected in our spectrum. We use the $5g^2G$–$6h^2H_0$ O IV λ4631.89 and the $6g^2G$–$7h^2H_0$ O IV λ7677.40 lines to compute the O^{4+}/H^+ ratio since they are hardly excited by other mechanisms than recombination.

Ne ORLs: we detect several permitted lines of Ne II, belonging to multiplets 1, 7, 39, 55, and 57. In Table 13 we show the ionic abundances from recombination lines of Ne II. To derive Ne^{++} abundances, we adopt the effective recombination coefficients by Kisielius et al. (1998) for multiplets 1, 7, and 39 and the computations by Kisielius & Storey (private communication), assuming LS-coupling for multiplets 55 and 57. Transitions from multiplet 1 and 55 are probably the result of recombination because they correspond to quartets and their ground level has a doublet configuration (Esteban et al. 2004). Transitions from multiplets 7 and 57 correspond to doublets and give abundances similar (m57) or lower (m7) than those derived from the multiplet 1 and 55 lines; however, given the high uncertainty in the flux of multiplet 7 λ 3323.74, we do not include this line in the final average abundance. Taking into account that the multiplet 55 lines correspond to 3d–4f transitions, whose upper levels are unlikely to be populated by fluorescence, it seems that in NGC 3918 all these lines are excited mainly by recombination. The multiplet 39 Ne II λ3829.77 line corresponds to an intercombination transition ($3p^2P^0$–$3d^4D$) and the abundance derived from it agrees with that derived from other multiplets, so this multiplet is probably mainly excited by recombination. Therefore, we adopt the averaged value from all multiplets as representative of the Ne^{++} abundance. From our derived Ne^{2+}/H^+ ratio from ORLs and CELs, we compute an $ADF(Ne^{2+}) = 2.54\pm0.37$, which is somewhat higher than that derived for O^{2+}, but is within the typical range of PNe. A similar result was found by Tsamis et al. (2004).

5.3 Total abundances

To correct for the unseen ionization stages and then derive the total gaseous abundances of chemical elements in NGC 3918, it is necessary to adopt a set of ICFs. For most elements, we adopted the ICFs recently developed by Delgado-Inglada, Morisset & Stasińska (2014) from a large grid of photoionization models and applied them to the ionic abundances computed from CELs, but also provided alternative computations when possible. The ICFs derived in Delgado-Inglada et al. (2014) were designed for large aperture observations (that cover the whole nebulae) as well as for small aperture observations across the central regions of the nebulae. Our observations avoid the central star but the slit is located sufficiently close to cover different ionization zones in the nebula. Moreover, we obtain similar ionic abundances and ionic fractions [for example, of $O^{++}/(O^+ + O^{++})$ and $He^{++}/(He^+ + He^{++})$] as the ones reported in Clegg et al. (1987) and Tsamis et al. (2003b), whose observations are adequate for these ICFs, and thus, we feel justified the adoption of these ICFs. The total abundances discussed in this section are shown in Table 14 and the specific criteria adopted in each particular case are discussed in the following. Uncertainties in the total abundances were computed through Monte Carlo simulations that take into account uncertainties in line fluxes, physical conditions and ionic abundances. For C, N, O, Ne, S, Cl, and Ar, we include in the Monte Carlo simulations the uncertainties in the ICFs reported by Delgado-Inglada et al. (2014).

The total C abundance is computed only from ORLs. The ICF proposed by Delgado-Inglada et al. (2014) in their equation 39 is based on C^{2+} and O^{2+} derived from ORLs and the result obtained is shown in Table 14. Alternatively, we also compute the C abundance by adding all the ionic abundances from C II, C III, and C IV ORLs and taking into account the contribution of C^+ by rescaling the C^+/C^{2+} obtained by Tsamis et al. (2003b) from CELs. The latter value is only 7 per cent higher than the value derived from an ICF (see Table 14).

When computing the O abundance from CELs, we apply the ICF by Delgado-Inglada et al. (2014) to correct for the unseen high-ionization ions. But we can also compute the O abundance from ORLs. As commented in the previous section, ionic abundances are estimated for several O ions from ORLs. Therefore, we can estimate the total O abundance from ORLs by adding the observed ionic species, and taking into account the contribution of O^+ by scaling the O^+/O^{2+} obtained from CELs. Alternatively, we can also compute the O total abundance from O^{2+} obtained from ORLs and the scaled O^+ abundance from CELs and the ICF provided by Delgado-Inglada et al. (2014). As shown in Table 14, there is an excellent agreement between both values, indicating that the ICF seems to estimate correctly the contribution of high-ionization ions to the total O abundance.

Table 14. Total abundances.

Ion	12 + log(*X*/H)				C87[a]		T03, T04[b]	
	CELs sum	CELs ICF	ORLs sum	ORLs ICF	CELs	ORLs	CELs	ORLs
He	–	–	11.01±0.01	–	–	11.03	–	11.00
C	–	–	8.93±0.04[c]	8.90±0.09[d]	–	8.90	8.64	8.88
N	–	8.12±0.09	–	–	8.18	–	8.02	–
O	–	8.67±0.06	8.90±0.05[e]	8.90±0.11[f]	8.70	–	8.86	9.09
Ne	8.04±0.06	7.95±0.06/8.01±0.06[g]	–	8.44±0.08	8.08	–	7.97	–
Na	–	6.07:	–	–	–	–	–	–
S	–	$6.81^{+0.06}_{-0.11}$	–	–	7.20	–	6.70	–
Cl	–	5.17±0.10	–	–	–	–	5.11	–
Ar	6.43±0.03	$6.40^{+0.08}_{-0.16}$[h]	–	–	6.30	–	6.24	–
K	–	4.85:	–	–	–	–	–	–
Ca	–	4.66:	–	–	–	–	–	–
Fe	4.95±0.07	4.84±0.08/4.48±0.10[i]	–	–	5.57	–	–	–
Se	–	$3.52^{+0.15}_{-0.23}$	–	–	–	–	–	–
Kr	3.80±0.04	3.97±0.12/3.89±0.06[j]	–	–	–	–	–	–
Rb	$2.51^{+0.14}_{-0.20}$	–	–	–	–	–	–	–
Xe	2.49±0.07	2.48±0.08	–	–	–	–	–	–

Notes. [a]Clegg et al. (1987).
[b]Tsamis et al. (2003b, 2004).
[c]Sum of C ionic species from ORLs, with C^+ estimated from the CEL C^+/C^{2+} ionic ratio by Tsamis et al. (2003b, see text).
[d]From C II ORLs and the ICF by Delgado-Inglada et al. (2014).
[e]Sum of O ionic species from ORLs, with O^+ estimated from the CEL O^+/O^{2+} ionic ratio (see text).
[f]From O II ORLs, O^+/O^{2+} from CELs, and the ICF by Delgado-Inglada et al. (2014).
[g]ICF from equation 17/equation 20 of Delgado-Inglada et al. (2014).
[h]ICF from equation 36 of Delgado-Inglada et al. (2014).
[i]Sum of all ionic abundances/ICF from equation 2/equation 3 by Rodríguez & Rubin (2005).
[j]Average from the ICFs given by Sterling et al. (2007)/average from the ICFs given by equations 4–6 of Sterling et al. (2015).

Thanks to the high ionization of NGC 3918, we detect lines of [Ne III], [Ne IV], and [Ne V] with a high S/N ratio (see Fig. 2). We need to correct for the contribution of Ne^+ to the total abundance. Therefore, we compute the total abundance in two ways: (i) by adding the ionic chemical abundances, and (ii) by using a classical ICF scheme that corrects the observed ionic abundances for the unseen ionization species. We use the ICFs given by equations 17 and 20 of Delgado-Inglada et al. (2014), which give the total Ne abundance when only [Ne III] lines are observed and both [Ne III] and [Ne V] lines are observed. All the results are shown in Table 14. The abundance obtained from the sum of the ionic species agree within the uncertainties with that derived using the ICF when [Ne III] and [Ne V] lines are detected, but it is ∼0.1 dex higher than that derived using only [Ne III] lines. Because auroral [Ne IV] lines are quite sensitive to the electron temperature, these ICFs do not use them. Considering all these factors, we adopt as a representative Ne abundance the value given by equation 20 of Delgado-Inglada et al. (2014), which is 8.01±0.06.

For Cl, we detect [Cl II], [Cl III], and [Cl IV] lines and, therefore, we use the ICF recommended by Delgado-Inglada et al. (2014) when all these lines are observed (their equation 32), which takes into account the contribution of high Cl ionization states.

Similarly to Ne, we detect several ionization stages of Ar in the spectrum of NGC 3918 (see Fig. 2). We compute the total Ar abundance by adding the ionic chemical abundances and by using the ICF proposed by Delgado-Inglada et al. (2014) when only [Ar III] lines are detected (their equation 36). The uncertainties associated with the ICF reported by these authors are very high (see their table 3 and fig. 13). Note that these uncertainties are likely overestimated since they are derived from the maximum dispersion in the ICF given by the grid of photoionization models. This is the reason why we obtain high errors on the Ar/H determination based on this ICF (see Table 14). Given that the ICFs for Kr and Xe are based on Ar abundances, we have tried to find a value for Ar/H with lower uncertainties. We select from the 3MdB models (Morisset, Delgado-Inglada & Flores-Fajardo 2015) the ones corresponding to the PNe_2014 reference (used by Delgado-Inglada et al. 2014, to compute their ICFs), adding as a selection criteria the fact that the models must reproduce simultaneously the Ar^{2+}/Ar, Ar^{3+}/Ar, Ar^{3+}/Ar, and O^{2+}/O ionic fractions (within ±5 per cent). These models then reproduce well the ionization structure of the nebula. The total Ar/H abundance for these models is found to be very close to the sum $Ar^{2+}/H + Ar^{3+}/H + Ar^{3+}/H$, with an error being less than 2 per cent. Therefore, we will use from now on the sum of these three ionic abundances as representative of the total Ar abundance.

As can be seen in Table 8, we measure several lines of multiple ionization stages of Fe. In Fig. 9 we show some of the lines used to compute ionic chemical abundances. The [Fe III] lines are usually the brightest iron lines in photoionized nebulae. However, as is shown in Fig. 9, this is not the case for NGC 3918, which is an extremely high ionization PN and presents several bright [Fe V], [Fe VI] and [Fe VII] lines. Taking this into account, we use two different approaches to compute the total Fe abundance: (i) in the first one, we use the correction scheme suggested by Rodríguez & Rubin (2005), which is based on the detection of [Fe III] lines and two ICFs, one from photoionization models (their equation 2) and one from an observational fit that takes into account all the uncertainties in the atomic data involved in the calculations and that allows us to constrain real iron abundances (their equation 3); (ii) in the second approach, we take advantage of the high-ionization degree of the

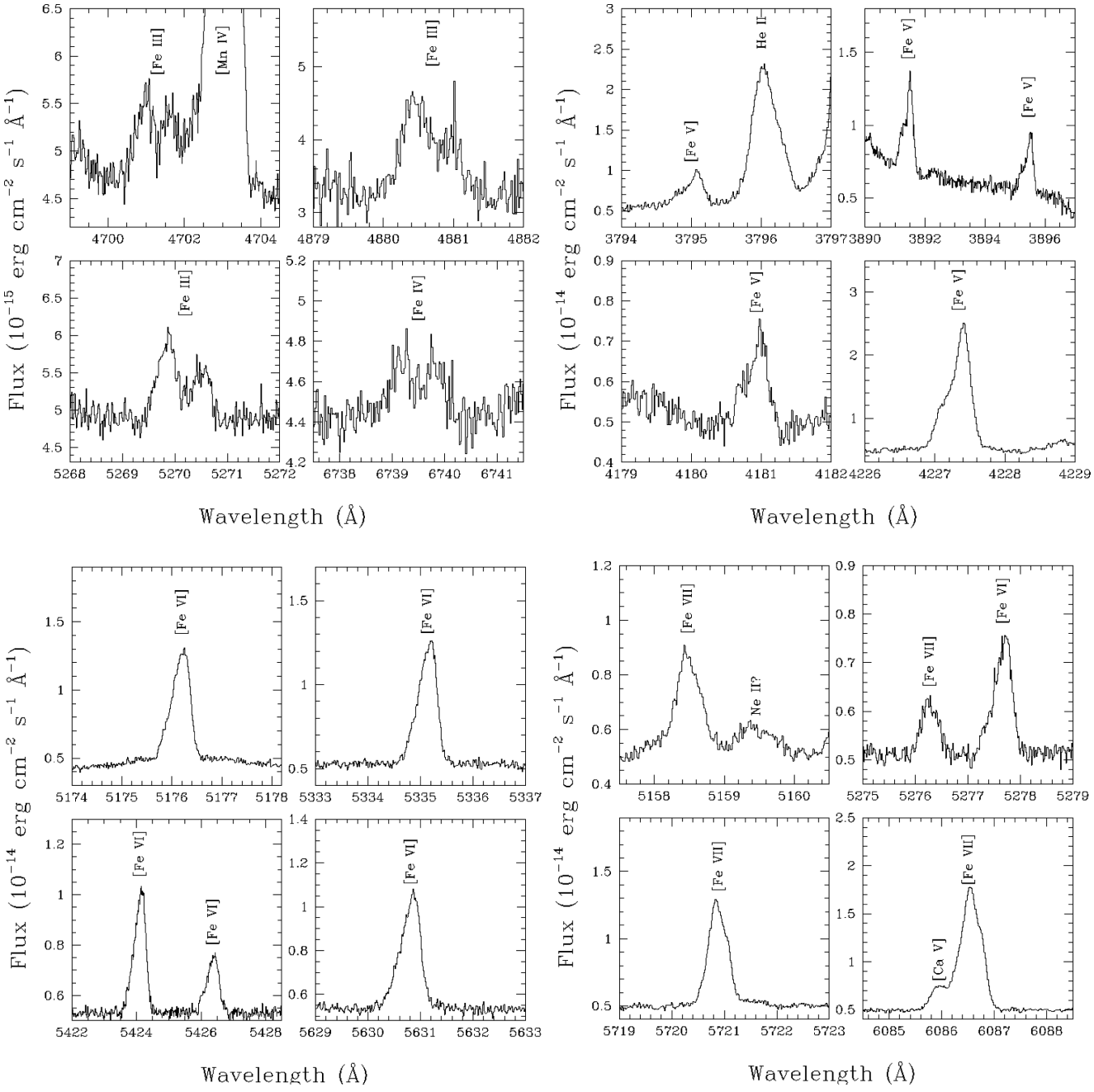

Figure 9. Portions of the echelle spectrum of NGC 3918 showing lines of different ionic species of Fe.

PN and simply compute the total abundance as the sum of all the observed ionic species. The results are shown in Table 14. As can be seen, the sum value is in very good agreement with the value derived from equation 2 of Rodríguez & Rubin (2005). Delgado-Inglada & Rodríguez (2014) also find several objects with high-ionization Fe ions. In a similar exercise to ours, they compare the sum of the ionic Fe abundances with the results obtained from the ICFs, but their results do not allow them to conclude which ICF works better. It must be taken into account that their data are more limited than our data both in spectral resolution, which is lower and, thus, prevents deblending some of the lines from other close-by features, and in the S/N ratio of the high-ionization Fe lines, which is also lower. We agree with their conclusion that the inherent limitations of ionization correction schemes are responsible for the different behaviours found and that high-resolution, high-S/N ratio data are needed to improve the ionization correction scheme or to define a new and better one, especially for high-ionization PNe.

To estimate the correction for the unseen ions of Ca, K and Na, for which no published ICFs exist, we compute a simple spherical photoionization model of the PN with CLOUDY (v. 13.03; Ferland et al. 2013), ionized by a blackbody with $T_{\rm eff} = 190$ kK. The inner and outer radius are set to $\log(r_{\rm in}) = 15.0$ and $\log(r_{\rm out}) = 17.16$ (in cm); at an assumed distance of 1 kpc, the projected radius equals the observed optical radius (19 arcsec). Using PYCLOUDY (Morisset 2013) CLOUDY's output has been corrected to account for the slit used to observe the nebula (9.35 arcsec × 1 arcsec:

see Section 2). The density, chemical composition, and total H β flux are set by design. The model thus computed reproduces the observed line ratios and the general ionization structure as given by O I through O IV and Ne III through Ne V. According to the model, Na^{3+} accounts for 35 per cent of the total sodium; K^{3+} and K^{4+} together account for the 46 per cent of the total potassium; and Ca^{4+} accounts for 17 per cent of the total calcium. This leads to an ICF of ∼2.9 for Na, ∼2.2 for K, and ∼5.8 for Ca. The validity of the model is supported by the nice agreement between the K^{3+}/K^{4+} ratios predicted by our model (1.04) and the one derived from the observations (1.10±0.25).

An alternative method to compute the abundances of these three elements is the ICF scheme by Delgado-Inglada et al. (2014), based on the public data base of photoionization models 3MdB developed by Morisset et al. (2015). We preliminarily verify the overall agreement of our model with the predictions by Delgado-Inglada et al. (2014) by comparing the ICFs of that paper with those returned by the model; the differences between both methods are 0, −0.04, −0.05, and +0.04 dex for He/H, Ne/H, Ne/O, and C/O and indicate a substantial agreement between the two methods. Based on the values of $O^{2+}/(O^{+}+O^{2+})$ and $He^{2+}/(He^{+}+He^{2+})$ of the nebula, a rough estimate gives us the following ICFs: ∼4.0 for Na, ∼3.2 for K, and ∼10.0 for Ca.

Given the overall agreement between the two methods, we adopt as a representative value of the total abundance for each atomic species the average of the values returned by both methods. The results are shown in Table 14.

The gaseous abundances of Ca, K, and Na relative to hydrogen in the interstellar medium are significantly lower than solar (Morton 1974), which is generally attributed to depletion into dust grains. The reported abundances of K and Na in PNe are about 1 dex lower than solar and the Ca abundances are between ∼0.8 and ∼2.5 dex lower than solar (Aller 1978; Aller et al. 1981; Shields et al. 1981; Aller & Czyzak 1983; Keyes, Aller & Feibelman 1990; Bohigas, Rodríguez & Dufour 2013). The abundances of Ca, K, and Na obtained here are 1.6, 0.6, and 0.3 dex lower than solar, respectively, suggesting a significant depletion of these elements (especially of Ca) into dust grains in NGC 3918.

The high depletion factors in NGC 3198 could be related to the dominant chemistry in the PN. Both the value of C/O ($\gtrsim$1, this work) and the broad feature at 30 μm found in the nebula (Delgado-Inglada & Rodríguez 2014) and often associated with MgS, reveal a carbon-rich environment. In the particular case of iron, Delgado-Inglada & Rodríguez (2014) found that the highest depletion factors are found in carbon-rich PNe.

Sterling, Dinerstein & Kallman (2007) constructed the first ionization correction scheme for Kr, using approximate atomic data. These authors propose ICFs based on detailed photoionization models and on the detection of multiple Kr ions in the optical and *K* band. Very recently, Sterling, Porter & Dinerstein (2015) incorporated new photoionization and recombination data into the modelling code CLOUDY (Ferland et al. 2013). They compute a large grid of photoionization models to determine a new set of ICFs for calculating the Kr elemental abundance. This new set provides different ICFs depending on the detection of different Kr ionic lines: [Kr III], [Kr IV], and [Kr V] and therefore, is perfectly fitted for our data. We note that the results obtained by using the different ICFs proposed by Sterling et al. (2015) display a relatively low dispersion, suggesting that the formulae proposed are quite robust. In Table 14 we show the total Kr abundances obtained by using the average of the ICFs proposed by Sterling et al. (2007) and the average of the ICFs obtained with equations 4–6 (which are the ones that use more than one ionization stage) of Sterling et al. (2015). We rely more on the second set of ICFs because they were computed from models that incorporated *ab initio* atomic data calculations (Sterling 2011; Sterling & Stancil 2011). Sharpee et al. (2007) also propose an ICF based on the similarity between the ionization potentials of the noble gases. This ICF scheme gives a result which is very similar (0.01 dex higher) to the sum of the observed ionic species, but is much lower than the other ICF schemes.

There are no reliable ICFs for Xe and Rb in the literature. Sharpee et al. (2007) propose a correction for Xe based on the similarity in the ionization potentials of noble gases. We used a similar scheme assuming that $Xe/Ar \approx (Xe^{2+}+Xe^{3+})/(Ar^{2+}+Ar^{3+})$. This scheme yields an abundance that is slightly lower than the sum of the ionic abundances. Therefore, for Xe and Rb, the total abundance is simply computed as the sum of all the observed ionic species. This gives us a lower limit to the total abundance.

5.4 Comparison with elemental abundances in the literature

The first attempt to compute chemical abundances in NGC 3918 was made by Torres-Peimbert & Peimbert (1977) from optical photoelectric spectrophotometry using a wide long-slit. Torres-Peimbert, Pena & Daltabuit (1981) obtain *IUE* low-dispersion spectra and construct ionization structure models to derive physical conditions and chemical content of the PN. Peña & Torres-Peimbert (1985) derive the physical conditions and chemical abundances from high-dispersion *IUE* spectra. The most detailed chemical analysis of NGC 3918 is the one by Clegg et al. (1987), who use a combination of high- and low-resolution *IUE* and optical long-slit spectra covering different positions in the nebula. Using UV, optical, and far-infrared (FIR) spectrophotometric data covering the whole nebula, Tsamis et al. (2003b) and Tsamis et al. (2004) study the chemical content of NGC 3918 derived from CELs and ORLs. Finally, Ercolano et al. (2003) construct a realistic photoionization model of NGC 3918 using a three-dimensional Monte Carlo photoionization code.

From Table 14 it is clear that the agreement between our total abundances with those elements in common with Clegg et al. (1987) is very good. For He, C, N, O, and Ne, their derived total abundances agree with ours within 0.05 dex. For Ar, the difference is slightly larger (between 0.1 and 0.2 dex depending on the ICF assumed). The abundances derived by these authors are computed through a tailored photoionization model to constrain UV and optical observations. In Clegg et al. (1987) computations, only the S/H and Fe/H ratios are significantly higher, by 0.4 dex and more than 0.6 dex, respectively. In Table 14 we also include the abundances obtained by Tsamis et al. (2003b) from UV, optical, and FIR CELs of C, N, O, S, Cl, Ne, and Ar and those derived by Tsamis et al. (2004) from C and O ORLs. In this case the agreement between C ORLs abundances is also very good. In general, the abundances agree within 0.1–0.15 dex, with a larger scatter for O (∼0.2 dex). In the case of CELs O abundances, the difference can be attributed mainly to the fact that they compute a high O^{3+}/H^{+} ratio from the UV O IV] λ1401 line, which is very sensitive to both temperature and extinction effects and, to a lesser extent, to the fact that they use the classical ICF scheme of Kingsburgh & Barlow (1994), which is based on a small grid of photoionization models. In the case of recombination line abundances, the differences are due to the fact that they scaled O^{3+}/O^{2+} from CELs, which is quite uncertain and is a factor of ∼4 higher than the ratio obtained from ORLs.

Table 15. Total abundance ratios.

Ratio	$[X/O]^a$
[Se/O]	$0.18^{+0.17}_{-0.22}$
$[Kr/O]^b$	0.60±0.13
$[Rb/O]^c$	$>0.17^{+0.17}_{-0.22}$
$[Xe/O]^c$	>0.21±0.11

Notes. $^a[X/O]=\log(X/O)-\log(X/O)_\odot$. Solar abundances from Asplund et al. (2005).
^{b}ICF for Kr is an average of the ICFs proposed by Sterling et al. (2015) from equations 4–6.
^{c}Lower limits. Total Rb and Xe from the sum of the ionic abundances.

6 DISCUSSION

6.1 s-process enrichments of n-capture elements

The total abundances of Se, Kr, Rb, and Xe can be used to establish if the central star has undergone a substantial s-process nucleosynthesis and convective dredge-up. As discussed in Sterling & Dinerstein (2008), the enrichment must be measured against a reference element which is neither enriched nor depleted in the object studied; for a metal-rich, non-type-I PN such as NGC 3918, a suitable element seem to be O; in the case of a type-I PNe, O can be affected by nucleosynthesis and then we use Ar as a reference (see Sterling & Dinerstein 2008). In order to establish which level of [*X*/O], where *X* is a n-capture element, counts as significant, it is necessary to take into account the primordial scatter in the abundances of the progenitor gas. Based on stellar data by Travaglio et al. (2004) and Burris et al. (2000), Sterling & Dinerstein (2008) estimate that s-process enrichment is statistically likely to have taken place if the [*X*/O] ratio is found to be in excess of 0.2–0.3 dex.

It should be noted that Delgado-Inglada et al. (2015) have recently found evidence of O enrichment in a group of Galactic PNe with carbon-rich dust, including NGC 3918. This result suggests that the real s-process element enrichment in this PN is likely higher. However, in order to compare our results with those found by Sterling et al. (2007) and Sterling et al. (2015) we still consider O as the metallicity proxy for these PNe.

The [Se/O], [Kr/O], [Xe/O], and [Rb/O][5] ratios determined for NGC 3918 from our data are shown in Table 15. If we adopted the more recent solar composition of Asplund et al. (2009), the derived abundances would change by less than 0.06 dex, with the exception of [Rb/O] which would be 0.11 dex larger. In the calculation, we assume the solar abundances by Asplund et al. (2005) for the sake of a direct comparison with the results by Sterling & Dinerstein (2008). For Kr we obtain [Kr/O] = 0.57±0.18, a value well above the threshold assumed by Sterling & Dinerstein (2008). We can therefore conclude that Kr is strongly enriched in NGC 3918. It is interesting to note that our Kr data, which include all the relevant ionization stages, make it possible to test the predictions of theoretical ICFs; the results support the ICFs proposed by Sterling et al. (2015).

For Se, owing to the difficulties detecting and measuring the line, the value we obtain, i.e. $[Se/O] = 0.18^{+0.17}_{-0.22}$ is very uncertain. Taking this result at face value, we find that Kr is more enriched than Se in NGC 3918 ($[Kr/Se] = 0.42^{+0.21}_{-0.26}$), in agreement with what is observed by Sterling & Dinerstein (2008) in a large sample of PNe with both Kr and Se emission ([Kr/Se] = 0.5±0.2) and with the predictions of theoretical models of s-process nucleosynthesis (Gallino et al. 1998; Goriely & Mowlavi 2000; Busso et al. 2001; Karakas et al. 2009).

The values obtained for Rb and Xe, in turn, are only marginally positive ($[Rb/O]>0.17^{+0.17}_{-0.22}$; [Xe/O]>0.21±0.11), so they do not allow us to draw any definite conclusion. It must be stressed, though, that these values are only lower limits to the real abundances, so we cannot exclude that these elements are actually enriched.

These two elements lie on opposite sides of the bottleneck in the s-process path corresponding to isotopes with the magic neutron number $N = 50$. This bottleneck occurs because species with closed neutron shells have very small n-capture cross-sections, leading to peaks in the element-by-element distribution of s-process enrichments (e.g. Käppeler et al. 2009). In stellar spectroscopy, n-capture elements produced by the s-process are often categorized as 'light-s' or 'heavy-s' elements if one of their isotopes has a magic number of $N = 50$ (e.g. the s-process peak near Zr) or $N = 82$ (the peak near Ba), respectively (e.g. Luck & Bond 2014). The abundance ratio [hs/ls] is a measure of the neutron exposure (the time-averaged neutron flux experienced by Fe-peak nuclei) in AGB stars. Both Kr and Xe have isotopes with a magic number of neutrons, and can be used as nebular proxies for light-s and heavy-s elements, respectively. The ratio $[Xe/Kr]\geq-0.39$ corresponds to a neutron exposure typical of modestly subsolar metallicity AGB stars, according to the models of Busso et al. (2001, see their figs 3 and 4). While this abundance ratio is a lower limit, it appears to be somewhat lower than the average $[Xe/Kr] \approx 0.0$ value found by Sharpee et al. (2007) in their sample of PNe. Theoretical studies have shown that a spread in the sizes of ^{13}C pockets and in average neutron exposures are needed, even in stars with the same mass and metallicity, in order to reproduce observations of s-process enrichments in AGB stars (e.g. Busso et al. 2001; Herwig 2005; Karakas & Lattanzio 2014). Herwig, Langer & Lugaro (2003) showed that the interplay between convective overshoot and rotationally induced mixing can naturally lead to a spread in neutron exposures in AGB stars of a given mass and metallicity. In order to draw more robust conclusions from these results, advances on two fronts are needed. First, a reliable ICF scheme is needed for Xe. This requires photoionization and recombination data such as Sterling & Witthoeft (2011) and Sterling (2011) produced for Se and Kr. Secondly, AGB nucleosynthesis model studies are needed to interpret [Xe/Kr] ratios and their relation to the [hs/ls] index used in studies of s-process nucleosynthesis in AGB stars.

Though only a lower limit, the modestly enhanced [Rb/O] value suggests that the reaction $^{13}C(\alpha, n)^{16}O$ was the neutron source in the AGB progenitor of NGC 3918, and not $^{22}Ne(\alpha, n)^{25}Mg$ which operates more efficiently in intermediate-mass AGB stars (García-Hernández et al. 2006; Karakas et al. 2012; van Raai et al. 2012). In particular, the high neutron density of the ^{22}Ne source opens branchings in the s-process path that lead to large enrichments of Rb relative to other n-capture elements, unlike the ^{13}C neutron source, which produces lower neutron densities. Therefore the modest Rb enrichment relative to Kr and Xe indicates that the progenitor mass of NGC 3918 is between 1.5 $M_\odot$ (the approximate lower limit for convective dredge-up to occur; Straniero, Gallino & Cristallo 2006) and 5–6 $M_\odot$ (Karakas et al. 2012). The upper limit to the progenitor mass is consistent with the abundances of other species in NGC 3918, in particular N/O and C/O. NGC 3918 is not a

[5] $[X/O]=\log(X/O)-\log(X/O)_\odot$. Solar abundance references are taken from Asplund, Grevesse & Sauval (2005).

Peimbert type I PN (Peimbert 1978), and thus its progenitor mass is expected to be less than 3–4 $M_{\odot}$. The analysis of n-capture element abundances confirms this expectation, and additionally places a lower limit to the progenitor mass of this PN.

A more definite statement regarding Rb and Xe would require either observing all the relevant ionization stages or correcting the observed ones with an ICF. Although corrections for unseen ions of Se and Kr exist (Sterling et al. 2007, 2015), no ICF expressions are available for Xe and Rb as yet, due to a lack of the atomic data required to derive such corrections. However, theoretical and experimental efforts to produce these atomic data are ongoing (Kerlin et al. 2015), after which photoionization modelling can be used to determine analytical ICF formulae (e.g. Sterling et al. 2015). As already noted above, photoionization models are especially productive if used in combination with data such as those presented in this paper, since the detection of several ionization stages for each element makes it possible to test the predictions of theoretical ICFs.

6.2 Correlation of s-process enrichments with the C/O ratio

Nucleosynthesis models also predict that n-capture elements correlate with the C/O ratio, as carbon is brought to the surface of AGB stars along with s-processed material during third dredge-up episodes (Gallino et al. 1998; Busso et al. 2001; Karakas & Lattanzio 2014). In the upper panel of Fig. 10 we show the correlation found by Sterling & Dinerstein (2008) for PNe of their sample with known abundances of C (from UV lines) and their Kr abundances obtained from NIR [Kr III] line detections (red squares). This correlation is marginal due to the large uncertainties in the Kr/O and C/O ratios. We have overplotted our result for NGC 3918 from optical data for both the C/O and the Kr/O ratios (big blue dot). We adopt C/O = 0.87±0.25 from C II and O II recombination lines (see Fig. 8 and the ICFs given by Kingsburgh & Barlow 1994). C/O ratios from ORLs generally agree with those derived from UV/optical CELs (Liu et al. 2004b; Delgado-Inglada & Rodríguez 2014) and, additionally, they are not affected by aperture corrections and extinction uncertainties, which can potentially affect C/O ratios derived from CELs. Additionally, we also include some data from García-Rojas et al. (2009) and García-Rojas et al. (2012) where Kr lines are detected. From García-Rojas et al. (2012) only NGC 6369 has detections of more than one ionization stage of Kr ([Kr III] and [Kr IV] lines are detected). For the other objects, only [Kr IV] lines are reported. However, a reinspection of the spectra in García-Rojas et al. (2012, 2013) has brought to light detections of the [Kr III] λ6826.70 line in the spectra of He 2-86, PC 14, Pe 1-1 and, possibly NGC 2867. These lines are not reported in García-Rojas et al. (2009) and García-Rojas et al. (2012) because they are strongly affected by charge transfer and telluric emission features. We use PYSSN to deblend this line from the charge transfer feature, the telluric emission lines, and a close He I line (see Fig. 11). The fluxes we obtain are shown in Table 16. We consider in all cases that the uncertainties in the flux measurements are larger than 40 per cent. Then, to compute the total Kr abundance for these new objects we use equation 3 of Sterling et al. (2015) when only [Kr IV] lines are detected (M 1-61 and NGC 2867) and equation 4 when both [Kr III] and [Kr IV] lines are detected (He 2-86, NGC 6369, PC 14, Pe 1-1). We computed C/O ratios by using the C^{2+} and O^{2+} abundances reported by García-Rojas et al. (2009) and García-Rojas et al. (2013) for these objects and applying the ICF recipes given by Kingsburgh & Barlow (1994, green triangles) in order to be consistent with the C/O ratios derived by Sterling et al. (2007). Additionally, we add two objects (M 1-25 and M 1-32) for which Sterling et al. (2007) report [Kr/(O,Ar)] ratios, but reanalyze the data including our log(C/O) ratios derived from C^{2+}/H^{+} and O^{2+}/H^{+} from ORLs reported by García-Rojas et al. (2013) and the ICFs by Kingsburgh & Barlow (1994, yellow squares).

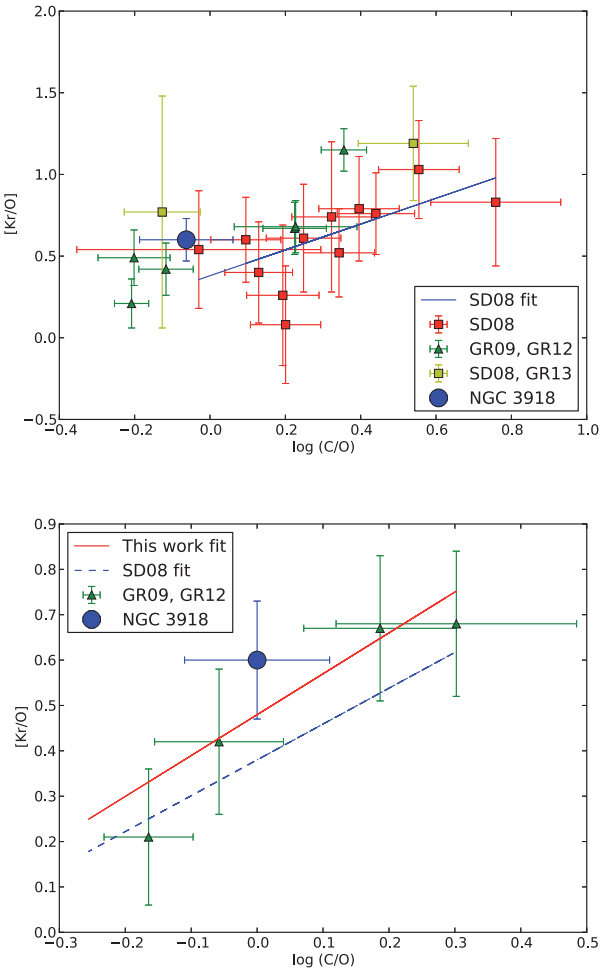

Figure 10. [Kr/O] versus log(C/O) correlation. Upper panel: red squares represent the data by Sterling & Dinerstein (2008) with C/O ratios computed from UV forbidden lines. Green triangles are data for objects of the sample by García-Rojas et al. (2009, 2012, 2013) with more than one ionization stage of Kr detected (see text); yellow squares are two objects with [Kr/O] ratios from Sterling & Dinerstein (2008) and log(C/O) determinations from ORLs (García-Rojas et al. 2013). The blue dot represent the result obtained for NGC 3918. For NGC 3918 and the objects of the sample of García-Rojas et al. (2009) and García-Rojas et al. (2012) where the C/O ratios are computed from optical recombination lines and using the ICF scheme by Kingsburgh & Barlow (1994). The least-squares fit to the Sterling & Dinerstein (2008) data is shown as a blue line. Lower panel: NGC 3918 and objects from the sample of García-Rojas et al. (2012) with measured [Kr III] and [Kr IV] lines. In this case, we apply the ICF scheme by Delgado-Inglada et al. (2014) to compute the total C and O abundances. A least-squares fit to the data is shown as a red line. For comparison we also show the fit to the Sterling & Dinerstein (2008) data.

Sterling et al. (2015) find that their equation 3 seems to produce larger Kr abundances than other equations, especially for low-ionization objects, and they do not recommend using this equation when [Kr III] emission is clearly detected. In Table 17 we show the total Kr abundances obtained from all equations of Sterling et al. (2015) for NGC 3918 and from equations 2– 4 for the objects of the García-Rojas et al. (2009) and García-Rojas et al. (2012)

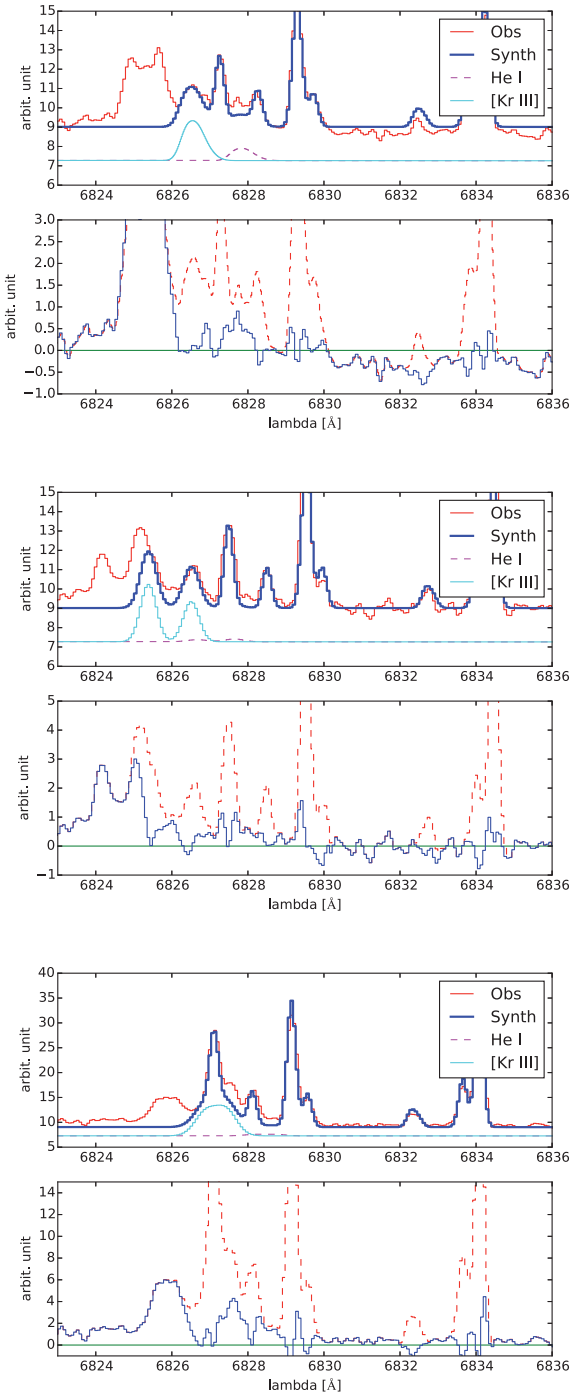

Figure 11. PYSSN fitting of the [Kr III] λ6826.70 + He I λ6827.88 lines in the spectra of He 2-86 (top panel), PC 14 (middle panel), and Pe 1-1 (lower panel). Colours and labels are the same as in Fig. 5. The feature labelled as CT is a feature produced by charge transfer coming from the emission of H α in a contiguous echelle order.

sample. Our results are very similar to those of Sterling et al. (2015) and their equation 3 gave a very high abundance compared to other equations. The exception is NGC 3918, owing to its high ionization.

In the lower panel of Fig. 10 we only include the objects with [Kr III] and [Kr IV] lines detected and compute the C/O ratios using C II and O II recombination lines and the ICFs given by Delgado-Inglada et al. (2014). We overplot our result for NGC 3918 adopting C/O = 1.00 ± 0.29 from C II and O II recombination lines and the ICFs given by Delgado-Inglada et al. (2014), which is in excellent agreement with the result obtained from the sum of ionic abundances (C/O = 1.02 ± 0.12). A least-squares linear fit taking into account uncertainties in both axis yields

$$[\mathrm{Kr/O}] = (0.480 \pm 0.027) + (0.901 \pm 0.240)\log(\mathrm{C/O}), \quad (2)$$

where the uncertainties include both the dispersion and the individual uncertainties for each object. The Spearman coefficient for the two variables is r(Spearman) = 0.94 ± 0.06 showing clearly that both quantities follow a monotonic relation. The Pearson coefficient is somewhat lower, but is also close to 1, r(Pearson) = 0.86 ± 0.07, indicating that the relation is probably linear; however, these values should be taken with caution given the low number of points in the correlation. Adding more points to the sample will strengthen even further our conclusions. It is important to remark that this fit is very similar to the ones obtained by Sterling & Dinerstein (2008) and Sterling et al. (2015) but with a much better correlation coefficient.

As can be shown, our approach of utilizing multiple Kr ions to derive Kr abundances and determining C/O ratios from ORLs gives more precise results than the combined UV and NIR data, and minimizes the uncertainties given by aperture effects in the different wavelength ranges as well as the uncertainties related to extinction. Additional very deep optical observations of a large sample of PNe could help to confirm this correlation of [Kr/O] with C/O (and also of [Br/O], [Se/O], [Rb/O], and [Xe/O]) to constrain nucleosynthesis models.

Similarly to what we have done for Kr, in Fig. 12 we show the correlation found by Sterling & Dinerstein (2008) for a sample of PNe with known abundances of C (from UV lines) and Se abundances obtained from NIR [Se III] line detections (red squares). The least-squares fit to these data is shown as a blue line. We overplot the point for NGC 3918 where the C/O ratio was computed from ORLs and using the ICF scheme by Kingsburgh & Barlow (1994). Our result is consistent with the fit found by Sterling & Dinerstein (2008).

Table 16. I([Kr III])/I(H β) λ6826.70 line ratios [I(H β) = 100] from the García-Rojas et al. (2012) PNe sample.

Object	$I(\lambda)/I(\mathrm{H}\,\beta)$
He 2-86	0.0104
NGC 6369	0.0210
PC 14	0.0229
Pe 1-1	0.0436

7 SUMMARY

In this work we develop a detailed study of the physical conditions and the chemical content of the PN NGC 3918, based on deep, high-resolution ($R \sim 40\,000$) spectrophotometric data obtained with the UVES echelle spectrograph at the VLT. We identify and measure more than 750 emission lines, making ours one of the deepest spectra ever taken for a PN.

Thanks to the high ionization of NGC 3918, we detect CELs of multiple ionization stages. In addition to the classical CELs of N, O, Ne, S, Cl, and Ar, we detect a large number of CELs of refractory element (Ca, K, Cr, Mn, Fe, Co, Ni, and Cu). We also detect very faint CELs of several n-capture elements (Se, Kr, Rb, and Xe). ORLs of multiple ionization stages of C, N, O, and Ne are also detected in our spectrum.

Table 17. Comparison of Kr abundances computed with the ICFs by Sterling et al. (2015).

PN	12+log(Kr/H)[a]					
	ICF equation 1	ICF equation 2	ICF equation 3	ICF equation 4	ICF equation 5	ICF equation 6
NGC 3918	$3.80^{+0.07}_{-0.11}$	3.86 ± 0.06	3.83 ± 0.05	$3.92^{+0.07}_{-0.04}$	3.85 ± 0.04	3.92 ± 0.05
He 2-86	3.64 ± 0.15	3.67 ± 0.17	4.08 ± 0.07	3.62 ± 0.07	–	–
M 1-61	–	–	3.78 ± 0.10	–	–	–
NGC 2867	–	–	4.35 ± 0.04	–	–	–
NGC 6369	3.92 ± 0.11	3.48 ± 0.14	4.52 ± 0.06	3.83 ± 0.07	–	–
PC 14	3.93 ± 0.15	3.71 ± 0.16	4.37 ± 0.09	3.81 ± 0.08	–	–
Pe 1-1	3.95 ± 0.15	3.97 ± 0.16	4.64 ± 0.05	3.96 ± 0.09	–	–

Note. [a]ICFs equations 1 and 2 based on Kr^{2+} abundances; ICF equation 3 based on Kr^{3+} abundances; ICF equation 4 based on Kr^{2+} and Kr^{3+} abundances; ICF equation 5 based on Kr^{3+} and Kr^{4+} abundances; ICF equation 6 based on Kr^{2+}, Kr^{3+}, and Kr^{4+} abundances.

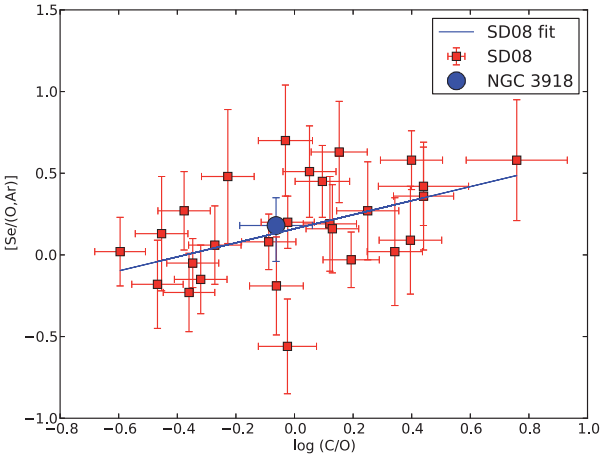

Figure 12. [Se/(O,Ar)] versus log(C/O). Red squares represent the data presented by Sterling & Dinerstein (2008) where C/O ratios were computed from UV forbidden lines. The blue dot represent the result obtained for NGC 3918. For NGC 3918 the C/O ratio was computed from optical recombination lines and using the ICF scheme by Kingsburgh & Barlow (1994). The least-squares fit to the Sterling & Dinerstein (2008) data is shown as a blue line.

We compute physical conditions from a large number of diagnostics, which are highly consistent among themselves assuming a three-zone ionization scheme.

We compute elemental abundances by using a state-of-the-art ICF scheme or simply adding ionic abundances. When multiple ionization stages are detected, both abundance determinations are in very good agreement, demonstrating the quality of the recent ICF scheme for high-ionization PNe. We also determine C/O ratios from pure recombination lines. These ratios derived from C II and O II ORLs and ICFs are consistent with those derived from the direct sum of all the ionic species detected, showing that C/O ratios from ORLs have a clear advantage over UV determinations.

Several refractory elements lines (Ca, K, Cr, Mn, Co, Ni, and Cu) were detected in the spectrum of NGC 3918. We estimate the abundance of Ca and K making use of ICFs derived from simple photoinization models. For several Fe-peak species we could not compute abundances owing to the lack of atomic data. New atomic data (specifically, transition probabilities and effective collision strengths for transitions between the lowest 50 energy levels) for these species are urgently needed to compute gas-phase abundances of these species and provide valuable information about the dust grain chemistry in PNe and AGB winds.

Chemical abundances of Se, Kr, Rb, and Xe are computed, in the case of Kr with unprecedented accuracy, thus constraining the efficiency of the s-process and convective dredge-up in NGC 3918's progenitor star. We find that Kr is strongly enriched in NGC 3918 and that Se is less enriched than Kr, in agreement with the results of previous papers and with predicted s-process nucleosynthesis. As we compute only lower limits to Rb and Xe enrichments we cannot draw definitive conclusions, but the results suggest that Xe is not as enriched by the s-process in NGC 3918 as is Kr and, therefore, that neutron exposure is typical of modestly subsolar metallicity AGB stars. The modest Rb enrichment relative to Kr and Xe seem to indicate that the progenitor mass of NGC 3918 is between 1.5 and 5–6 $M_{\odot}$.

A clear correlation is found when representing [Kr/O] versus log(C/O) for NGC 3918 and other objects with detection of multiple ions of Kr in optical data confirming that carbon is brought to the surface of AGB stars along with s-processed material during third dredge-up episodes, as predicted by nucleosynthesis models. Additional deep high-resolution spectrophotometric data are needed for [Br/O], [Se/O], [Rb/O], and [Xe/O] versus C/O to put narrow constraints to nucleosynthesis models.

ACKNOWLEDGEMENTS

This work is based on observations collected at the European Southern Observatory, Chile, proposal number ESO 090.D-0265(A). This work has been funded by the Spanish Ministry of Economy and Competitiveness (MINECO) under the grant AYA2011-22614, CONACyT, Mexico under grant CB-2010/153985 and by the DGAPA-UNAM, Mexico under grant PAPIIT-107215. We want to thank the anonymous referee for his/her valuable comments. JG-R acknowledges support from Severo Ochoa excellence program (SEV-2011-0187) postdoctoral fellowship. VL acknowledges support of the Spanish Ministry of Science and Innovation through grant AYA 2011-22614. NCS gratefully acknowledges support of this work from an NSF Astronomy and Astrophysics Postdoctoral Fellowship under award AST-0901432 and from NASA grant 06-APRA206-0049. GD-I gratefully acknowledges support from a DGAPA postdoctoral grant from the Universidad Nacional Autónoma de México (UNAM) and the GSI Foundation. JG-R acknowledges all staff, employees, and guests of the Instituto de Astronomía at UNAM, where part of this work was done. We also

thank C. Esteban, D. A. García-Hernández, D. Péquignot, and M. Rodríguez for fruitful discussions.

REFERENCES

Aller L. H., 1978, in Terzian Y., ed., Proc. IAU Symp. 76, Planetary Nebulae. Reidel, Dordrecht, p. 225
Aller L. H., Czyzak S. J., 1983, ApJS, 51, 211
Aller L. H., Keyes C. D., Ross J. E., Omara B. J., 1981, MNRAS, 197, 647
Asplund M., Grevesse N., Sauval A. J., 2005, in Barnes T. G., III Bash F. N., eds, ASP Conf. Ser. Vol. 336, Cosmic Abundances as Records of Stellar Evolution and Nucleosynthesis. Astron. Soc. Pac., San Francisco, p. 25
Asplund M., Grevesse N., Sauval A. J., Scott P., 2009, ARA&A, 47, 481
Baldwin J. A., Verner E. M., Verner D. A., Ferland G. J., Martin P. G., Korista K. T., Rubin R. H., 2000, ApJS, 129, 229
Ballance C. P., Griffin D. C., McLaughlin B. M., 2007, J. Phys. B: At. Mol. Phys., 40, 327
Ballester P., Modigliani A., Boitquin O., Cristiani S., Hanuschik R., Kaufer A., Wolf S., 2000, The Messenger, 101, 31
Baluteau J. -P., Zavagno A., Morisset C., Péquignot D., 1995, A&A, 303, 175
Becker S. R., Butler K., Zeippen C. J., 1989, A&A, 221, 375
Bhatia A. K., Doschek G. A., 1993, At. Data Nucl. Data Tables, 55, 315
Bhatia A. K., Kastner S. O., 1988, ApJ, 332, 1063
Biémont E., Hansen J. E., 1986a, Phys. Scr., 33, 117
Biémont E., Hansen J. E., 1986b, Phys. Scr., 34, 116
Biémont E., Hansen J. E., Quinet P., Zeippen C. J., 1995, A&AS, 111, 333
Blum R. D., McGregor P. J., 2008, AJ, 135, 1708
Bohigas J., Rodríguez M., Dufour R. J., 2013, Rev. Mex. Astron. Astrofis, 49, 227
Burris D. L., Pilachowski C. A., Armandroff T. E., Sneden C., Cowan J. J., Roe H., 2000, ApJ, 544, 302
Busso M., Gallino R., Wasserburg G. J., 1999, ARA&A, 37, 239
Busso M., Gallino R., Lambert D. L., Travaglio C., Smith V. V., 2001, ApJ, 557, 802
Butler K., Zeippen C. J., 1989, A&A, 208, 337
Butler K., Zeippen C. J., Le Bourlot J., 1988, A&A, 203, 189
Chen G. X., Pradhan A. K., 1999, A&AS, 136, 395
Chen G. X., Pradhan A. K., 2000, A&AS, 147, 111
Clegg R. E. S., Walsh J. R., 1985, MNRAS, 215, 323
Clegg R. E. S., Harrington J. P., Barlow M. J., Walsh J. R., 1987, ApJ, 314, 551
Corradi R., García-Rojas J., Jones D., Rodríguez-Gil P., 2015, ApJ, 803, 99
D'Odorico S., Cristiani S., Dekker H., Hill V., Kaufer A., Kim T., Primas F., 2000, in Bergeron J., ed., Proc. SPIE Conf. Ser. Vol. 4005, Discoveries and Research Prospects from 8- to 10-Meter-Class Telescopes. SPIE, Bellingham, p. 121
Dance M., Palay E., Nahar S. N., Pradhan A. K., 2013, MNRAS, 435, 1576
Davey A. R., Storey P. J., Kisielius R., 2000, A&AS, 142, 85
Delgado-Inglada G., Rodríguez M., 2014, ApJ, 784, 173
Delgado-Inglada G., Morisset C., Stasińska G., 2014, MNRAS, 440, 536
Delgado-Inglada G., Rodríguez M., Peimbert M., Stasińska G., Morisset C., 2015, MNRAS, 449, 1797
Dinerstein H. L., 2001, ApJ, 550, L223
Ellis D. G., Martinson I., 1984, Phys. Scr., 30, 255
Ercolano B., Morisset C., Barlow M. J., Storey P. J., Liu X.-W., 2003, MNRAS, 340, 1153
Escalante V., Victor G. A., 1992, Planet. Space Sci., 40, 1705
Esteban C., Peimbert M., Torres-Peimbert S., Escalante V., 1998, MNRAS, 295, 401
Esteban C., Peimbert M., García-Rojas J., Ruiz M. T., Peimbert A., Rodríguez M., 2004, MNRAS, 355, 229
Fang X., Liu X.-W., 2011, MNRAS, 415, 181
Fang X., Storey P. J., Liu X.-W., 2011, A&A, 530, A18
Fang X., Storey P. J., Liu X.-W., 2013, A&A, 550, C2
Ferland G. J. et al., 2013, Rev. Mex. Astron. Astrofis., 49, 137
Froese Fischer C., Tachiev G., 2004, At. Data Nucl. Data Tables, 87, 1
Froese Fischer C., Rubin R. H., Rodríguez M., 2008, MNRAS, 391, 1828
Galavís M. E., Mendoza C., Zeippen C. J., 1995, A&AS, 111, 347
Galavís M. E., Mendoza C., Zeippen C. J., 1997, A&AS, 123, 159
Gallino R., Arlandini C., Busso M., Lugaro M., Travaglio C., Straniero O., Chieffi A., Limongi M., 1998, ApJ, 497, 388
García-Hernández D. A., García-Lario P., Plez B., D'Antona F., Manchado A., Trigo-Rodríguez J. M., 2006, Science, 314, 1751
García-Rojas J., Esteban C., 2007, ApJ, 670, 457
García-Rojas J., Peña M., Peimbert A., 2009, A&A, 496, 139
García-Rojas J., Peña M., Morisset C., Mesa-Delgado A., Ruiz M. T., 2012, A&A, 538, A54
García-Rojas J., Peña M., Morisset C., Delgado-Inglada G., Mesa-Delgado A., Ruiz M. T., 2013, A&A, 558, A122
Giles K., 1981, MNRAS, 195, 63
Goriely S., Mowlavi N., 2000, A&AS, 362, 599
Grandi S. A., 1976, ApJ, 206, 658
Hamuy M., Walker A. R., Suntzeff N. B., Gigoux P., Heathcote S. R., Phillips M. M., 1992, PASP, 104, 533
Hamuy M., Suntzeff N. B., Heathcote S. R., Walker A. R., Gigoux P., Phillips M. M., 1994, PASP, 106, 566
Herwig F., 2005, ARA&A, 43, 435
Herwig F., Langer N, Lugaro M, 2003, ApJ, 593, 1056
Johansson S., Zethson T., Hartman H., Ekberg J. O., Ishibashi K., Davidson K., Gull T., 2000, A&A, 361, 977
Käppeler F., Gallino R., Bisterzo S. Aoki W., 2011, Rev. Mod. Phys., 83, 157
Karakas A. I., Lattanzio J. C., 2014, PASA, 31, 62
Karakas A. I., van Raai M. A., Lugaro M., Sterling N. C., Dinerstein H. L., 2009, ApJ, 690, 1130
Karakas A. I., García-Hernández D. A., Lugaro M., 2012, ApJ, 751, 8
Kaufman V., Sugar J., 1986, J. Phys. Chem. Ref. Data, 15, 321
Kerlin A. B., Macaluso D. A., Bautista M. A., Bilodeau R. C., Aguilar A., Kilcoyne A. L. D., Dumitriu I., Sterling N. C., 2015, in Laboratory Astrophysics for Beyond Hubble: Fundamental Processes from the NIR to the FUV, in press
Keyes C. D., Aller L. H., Feibelman W. A., 1990, PASP, 102, 59
Kingsburgh R. L., Barlow M. J., 1994, MNRAS, 271, 257
Kisielius R., Storey P. J., 2002, A&A, 387, 1135
Kisielius R., Storey P. J., Davey A. R., Neale L. T., 1998, A&AS, 133, 257
Kisielius R., Storey P. J., Ferland G. J., Keenan F. P., 2009, MNRAS, 397, 903
LaJohn L., Luke T. M., 1993, Phys. Scr., 47, 542
Liu X.-W., Danziger J., 1993, MNRAS, 261, 465
Liu X.-W., Storey P. J., Barlow M. J., Clegg R. E. S., 1995, MNRAS, 272, 369
Liu X.-W., Storey P. J., Barlow M. J., Danziger I. J., Cohen M., Bryce M., 2000, MNRAS, 312, 585
Liu X.-W., Luo S.-G., Barlow M. J., Danziger I. J., Storey P. J., 2001, MNRAS, 327, 141
Liu Y., Liu X.-W., Luo S.-G., Barlow M. J., 2004a, MNRAS, 353, 1231
Liu Y., Liu X.-W., Barlow M. J., Luo S.-G., 2004b, MNRAS, 353, 1251
Luck R. E., Bond H. E., 1991, ApJS, 77, 515
Luridiana V., Morisset C., Shaw R. A., 2015, A&A, 573, A42
McLaughlin B. M., Bell K. L., 2000, J. Phys. B: At. Mol. Phys., 33, 597
McNabb I. A., Fang X., Liu X.-W., Bastin R. J., Storey P. J., 2013, MNRAS, 428, 3443
Mendoza C., 1983, in Flower D. R., ed., Proc. IAU Symp. 103, Planetary Nebulae. Reidel, Dordrecht, p. 143
Mendoza C., Zeippen C. J., 1982a, MNRAS, 198, 127
Mendoza C., Zeippen C. J., 1982b, MNRAS, 199, 1025
Mendoza C., Zeippen C. J., 1983, MNRAS, 202, 981
Morisset C., 2013, Astrophysics Source Code Library, record ascl:1304.020
Morisset C., Delgado-Inglada G., Flores-Fajardo N., 2015, Rev. Mex. Astron. Astrofis, 51, 103
Morton D. C., 1974, ApJ, 193, L35
Nahar S. N., Delahaye F., Pradhan A. K., Zeippen C. J., 2000, A&AS, 144, 141
Nussbaumer H., Storey P. J., 1984, A&AS, 56, 293

Otsuka M., Tajitsu A., 2013, ApJ, 778, 146
Otsuka M., Tajitsu A., Hyung S., Izumiura H., 2010, ApJ, 723, 658
Otsuka M., Meixner M., Riebel D., Hyung S., Tajitsu A., Izumiura H., 2011, ApJ, 729, 39
Peimbert M., 1978, in Terzian Y., ed., Proc. IAU Symp. 76, Planetary Nebulae. Reidel, Dordrecht, p. 215
Peimbert M., Peimbert A., Ruiz M. T., Esteban C., 2004, ApJS, 150, 431
Peimbert A., Peimbert M., Ruiz M. T., 2005, ApJ, 634, 1056
Peña M., Torres-Peimbert S., 1985, Rev. Mex. Astron. Astrofis., 11, 35
Péquignot D., Baluteau J.-P., 1994, A&A, 283, 593
Péquignot D., Petitjean P., Boisson C., 1991, A&A, 251, 680
Péquignot D., Morisset C., Casassus S., 2012, in Manchado A., Stanghellini L., Schönberner D., eds, Proc. IAU Symp. 283, Planetary Nebulae: An Eye to the Future. Cambridge Univ. Press, Cambridge, p. 470
Podobedova L. I., Kelleher D. E., Wiese W. L., 2009, J. Phys. Chem. Ref. Data, 38, 171
Porter R. L., Ferland G. J., Storey P. J., Detisch M. J., 2012, MNRAS, 425, L28
Porter R. L., Ferland G. J., Storey P. J., Detisch M. J., 2013, MNRAS, 433, L89
Quinet P., 1996, A&AS, 116, 573
Ramsbottom C. A., Bell K. L., 1997, At. Data. Nucl. Data Tables, 66, 65
Rodríguez M., Rubin R. H., 2005, ApJ, 626, 900
Ruiz M. T., Peimbert A., Peimbert M., Esteban C., 2003, ApJ, 595, 247
Schoening T., Butler K., 1998, A&AS, 128, 581
Schoning T., 1997, A&AS, 122, 277
Seaton M. J., 1979, MNRAS, 187, 73P
Sharpee B., Williams R., Baldwin J. A., van Hoof P. A. M., 2003, ApJS, 149, 157
Sharpee B., Zhang Y., Williams R., Pellegrini E., Cavagnolo K., Baldwin J. A., Phillips M., Liu X.-W., 2007, ApJ, 659, 1265
Shields G. A., Aller L. H., Keyes C. D., Czyzak S. J., 1981, ApJ, 248, 569
Sterling N. C., 2011, A&A, 533, A62
Sterling N. C., Dinerstein H. L., 2008, ApJS, 174, 158
Sterling N. C., Stancil P. C., 2011, A&A, 535, A117
Sterling N. C., Witthoeft M. C., 2011, A&A, 529, A147
Sterling N. C., Dinerstein H. L., Kallman T. R., 2007, ApJS, 169, 37
Sterling N. C. et al., 2009, PASA, 26, 339
Sterling N. C., Porter R. L., Dinerstein H. L., 2015, ApJS, 218, 25
Storey P. J., 1994, A&A, 282, 999
Storey P. J., Hummer D. G., 1995, MNRAS, 272, 41
Storey P. J., Zeippen C. J., 2000, MNRAS, 312, 813
Storey P. J., Sochi T., Badnell N. R., 2014, MNRAS, 441, 3028
Straniero O., Gallino R., Cristallo S., 2006, Nucl. Phys. A, 777, 311
Tayal S. S., 2004, A&A, 426, 717
Tayal S. S., 2011, ApJS, 195, 12
Tayal S. S., Gupta G. P., 1999, ApJ, 526, 544
Tayal S. S., Zatsarinny O., 2010, ApJS, 188, 32
Tody D., 1993, in Hanisch R. J., Brissenden R. J. V., Barnes J., eds, ASP Conf. Ser. Vol. 52, Astronomical Data Analysis Software and Systems II. Astron. Soc. Pac., San Francisco, p. 173
Torres-Peimbert S., Peimbert M., 1977, Rev. Mex. Astron. Astrofis., 2, 181
Torres-Peimbert S., Pena M., Daltabuit E., 1981, in Chapman R. D., ed., NASA Conf. Publ. Vol. 2171, The Universe at Ultraviolet Wavelengths: The First Two Yrs. of Intern. Ultraviolet Explorer. NASA, Washington, DC p 641
Travaglio C., Gallino R., Arnone E., Cowan J., Jordan F., Sneden C., 2004, ApJ, 601, 864
Tsamis Y. G., Barlow M. J., Liu X.-W., Danziger I. J., Storey P. J., 2003a, MNRAS, 338, 687
Tsamis Y. G., Barlow M. J., Liu X.-W., Danziger I. J., Storey P. J., 2003b, MNRAS, 345, 186
Tsamis Y. G., Barlow M. J., Liu X.-W., Storey P. J., Danziger I. J., 2004, MNRAS, 353, 953
van Raai M. A., Lugaro M., Karakas A. I., García-Hernández D. A., Yong D., 2012, A&A, 540, A44
Vanzi L., Cresci G., Telles E., Melnick J., 2008, A&A, 486, 393
Wiese W. L., Fuhr J. R., Deters T. M., 1996, Atomic Transition Probabilities of Carbon, Nitrogen, and Oxygen: a Critical Data Compilation. American Chemical Society, Washington, DC
Witthoeft M. C., Badnell N. R., 2008, A&A, 481, 543
Zhang H., 1996, A&AS, 119, 523
Zhang H. L., Pradhan A. K., 1997, A&AS, 126, 373
Zhang Y., Liu X.-W., Liu Y., Rubin R. H., 2005, MNRAS, 358, 457

This paper has been typeset from a TEX/LATEX file prepared by the author.